A Study of the Fragmentation of Quarks in e^-p Collisions at HERA using the H1 Detector

David Kant

Department of Physics,
Queen Mary and Westfield College,
University of London

A thesis submitted in accordance with the regulations
for the Degree of Doctor of Philosophy
in the University of London

November 1995

Abstract

Deep inelastic scattering (DIS) events, selected from 1993 data taken by the H1 experiment at HERA, are studied in the Breit frame of reference. A review of the current theory relevant to this thesis is presented along with a description of the H1 detector.

The fragmentation function of the struck quark is compared with those of e^+e^- data. It is shown that certain aspects of the quarks emerging from within the proton in ep interactions are essentially the same as those of quarks pair-created from the vacuum in e^+e^- annihilation. The measured area (average charged multiplicity), peak position and width of the fragmentation function show that the kinematic evolution variable equivalent to the e^+e^- squared centre of mass energy is, in the Breit frame, the invariant square of the four-momentum transfer. Comment is made on the extent to which there is evidence for coherence effects in parton showers.

Contents

List of Figures

List of Tables

Acknowledgements

It would be a monumental task to recount all of the people without whom this work might not have been possible. Therefore, I apologize in advance to those who are not mentioned but hope to thank them in the near future.

I would like to extend my thanks to my supervisor, Graham Thompson, for providing guidance and advice as well as taking the time to answer all my questions - including the silly ones - over the past three years. I also thank him for prof leading dis theseis. I would also like to thank the staff at QMW particularly; Murrough Landon and Paul Kyberd for sorting out all of my computing problems, Derek Newman-Coburn for his King Georges', Wladimir Von Schlippe for invaluable discussions concerning the Breit frame, and Paul Harrison and the other *deadly lampshade* crew for bringing a new meaning to the word noise!

For teaching me everything about nothing and, nothing about everything else I thank the following people, past and present, from room 401. Andy for playing techno music really loud and not crashing his bike - with me on the back - on the M40, en route to yet another deadly lampshade gig; Thanos ('... does the battered cod have any cheese with it?' and 'Can I have six chicken burgers please?') for his *unusual* behaviour; Spon for making me throw up in Billard Hause near the North hall (I had to cycle home as well!); James for his unusual 'hands on' approach to laboratory demonstrating; Mohsin for his inability to think rationally after half a bottle of whisky (I had the other half) leading to an 'incident' involving a shopping trolley in an empty car park at 6.00 am New year's morning; Asif for his inability to think rationally while ordering food at a restaurant; Simon for spilling coffee on me (twice in one day!); Adil for knowing loads of gorgeous chicks and Asif again for his inability to consume the collosal volume of food ordered in the restaurant. I would also like to thank Eram, Rob, Martin, Keith and Daniel. Good luck guys....you're gonna need it!

Life in Hamburg was really good fun partly because my supervisor was 500 miles away but mostly because of the hours of entertainment shared with the following people. I thank the Birmingham boys Paul Newman, Paul Sutton, Lee West and Stuart Robertson; Gerry Lopez, Alan Wilson, Phil Kaziewicz, Valerie Jamieson, Gareth Noyes, Phil Biddulph and Andy Mehta.

I would also like to thank David Cussans, Steven Burke, Dave Sankey and John Morris for their invaluable help with the fragmentation analysis. John Dainton and Michael Kuhlen for their advice and encouragement.

I acknowledge the Particle Physics and Astronomy Research Council (PPARC), formerly known as the Science and Engineering Research Council (SERC), for their financial support.

For my Father

Preface

A proper quantum mechanical treatment of multi-parton emission in perturbative QCD involves the notion of colour coherence. The inability of long wavelength gluons to resolve individual colour charges of partons within the parton cascade reduces the available phase space for soft gluon emission to an angular ordered region due to interference effects. This prescription is modelled in the modified leading logarithm approximation (MLLA) and gives rise to a characteristic 'hump-backed' plateau in the parton momentum spectra. With the hypothesis of local parton-hadron duality (LPHD) this also applies for observable hadrons and has been observed in e^+e^- interactions.

In ep deep inelastic scattering (DIS) the parton shower resulting from the fragmentation of the struck parton is time-like as in e^+e^- interactions. However, in ep interactions the proton fragmentation region is more complicated, since it contains the space-like evolution parton cascade as well as time-like radiation showers *and* the remnant from the initial beam proton. In order to compare to the MLLA predictions and to the e^+e^- data, the ep events at HERA are studied in the Breit frame. This frame is defined by two requirements. The exchanged virtual photon and the incoming proton momenta are antiparallel to one another and, the virtual photon is *purely* space-like i.e, no energy component in its four-vector. In this frame, by definition particles with a negative longitudinal component of momentum constitute the "current hemisphere" and the rest is denoted as the proton fragmentation region.

The purpose of this thesis is to compare the properties of the fragmentation process initiated by the struck quark in DIS in the current hemisphere of the Breit frame to those of quarks that are pair created in e^+e^- interactions, and to the predictions of the MLLA. This thesis will not concern itself with any investigation of the proton fragmentation region. The work presented in this thesis has been published and may be found in reference [74] and tables of data relevant to this analysis can be found on World Wide Web at the following site; *http://durpdg.dur.ac.uk/HEPDATA*.

Chapter one gives a brief overview of the HERA collider and the H1 experiment concentrating on the principle detector components used in this analysis. Chapter two is designed to give the reader a feeling for the various type of physics processes that occur at HERA. Particular attention is given to processes that are a background to DIS and to Monte Carlo models that are able to describe the data. These models are discussed further in chapter three which also discusses some of the theoretical background relevant to this thesis.

The selection of DIS candidates that comprise the data used in this thesis is discussed in chapter four. To calculate the boost to the Breit frame of reference, the kinematic variables x and Q^2 must be determined as accurately as possible. Thus a comparison of the different methods of kinematic reconstruction are reviewed and the resolution of the variables from each of the methods is compared in different regions of the (x, Q^2) plane. Due to the $1/Q^4$ dependence of the neutral current DIS cross section, the data are subdivided into ten analysis bins in order to study the energy evolution of the fragmentation function.

The analysis presented in chapter four shows that the variables x and Q^2 are best determined from the electron only method. The boost to the Breit frame is thus calculated from the kinematics determined solely from this method and is done via the hadronic centre-of-mass system (CMS) as described in chapter five. In order to avoid large acceptance corrections to the data a selection based on the calorimetric energy flow observed in one hemisphere of the Breit frame is discussed. A description of the method used to make acceptance corrections to the data is given in chapter six.

The properties of the fragmentation function for charged particles in the current hemisphere of the Breit frame with increasing energy are presented in chapter seven. These results are compared to those of similar analyses in e^+e^- interactions. The data are also compared to a number of different QCD models which utilise different ansätze for the description of coherence effects and hadronisation. A full account of all possible sources of systematic error is also given.

Chapter 1

HERA and the H1 Detector

1.1 The HERA Collider

HERA [1] consists of two independent accelerators designed to accelerate and then store bunches of protons and electrons (or positrons) of energy 820 GeV and 30 GeV respectively. The two beams, housed inside a tunnel of circumference 6.3 km situated about 20 meters below ground, counter rotate in their respective rings and intersect at four interaction points at zero crossing angle. The overall layout of the HERA machine including pre-accelerators to inject the electron and proton beams into HERA is shown in Figure 1.1.

Figure 1.1: *Schematic view of the HERA accelerator and pre-accelerators. Shown also are the intersection regions housing the H1, ZEUS and HERMES experiments.*

Electrons (positrons) are injected into a small storage ring from a 500 MeV linear accelerator. They are accumulated into a 60 mA single bunch and injected into DESY II where they are accelerated to 7 GeV and transferred to the modified PETRA II ring. This stage is repeated at a rate of 12.5 Hz until PETRA II has been filled with 70 bunches each approximately 28.8 meters apart. The bunches are then injected into the HERA main ring. According to design, the procedure is repeated two more times until there are 210 bunches in the main ring.

A new chain of pre-accelerators was built in order to inject protons into HERA. A 50 MeV linear accelerator is used to strip negatively charged hydrogen ions of their electrons and inject them into DESY III. Here the protons are accelerated to 7.5 GeV and then transferred to PETRA II, where they are accelerated to 40 GeV before the final injection into the HERA ring.

During 1993 HERA operated with bunches of electrons of energy 26.7 GeV colliding with bunches of protons of energy 820 GeV, with a time between bunch crossings of 96 ns. For 1993 data-taking, 84 paired bunches were filled for each beam and in addition 10 electron and 6 proton satellite bunches were left unpaired for calibration and background monitoring purposes.

To detect collisions between electron and proton bunches, two detectors, H1 [2] and ZEUS [3] have been built. As can be seen from Figure 1.1, the H1 and ZEUS detectors are located at the North and South halls respectively. A third experiment, HERMES [4], is situated at the East hall and is presently under construction. HERMES will study collisions between polarized electron and atomic beams thus enabling measurements to be made of the polarized nucleon structure functions [5].

1.2 General Description of the H1 Detector

The H1 detector [2] is a general purpose 4π detector built to study the various physics processes outlined in chapter 2. A longitudinal view along the beam line of H1 is shown in figure 1.2.

Due to the imbalance in the energy of the colliding beams the centre of mass for HERA collisions is boosted along the proton direction[1]. As a consequence of this,

---

[1] The incoming proton by definition moves in the positive z direction with $\theta = 0°$ polar angle, also called the forward direction. At H1 this is an East to West direction.

Figure 1.2: *Longitudinal cut through the H1-detector along the beam line.*

the detector is more densely instrumented in the proton direction to measure the large particle multiplicities and large energy flow emerging from this direction.

H1 coordinates are based on the right-handed cartesian system. The z-axis increases in the direction of the proton beam with origin - the nominal vertex point - at the centre of H1. The positive x-axis is directed towards the centre of HERA and the positive y-axis is vertically upwards.

Charged particles are tracked in a uniform magnetic field of 1.15 T which is produced by a superconducting solenoid that surrounds the calorimeter. The tracking system consists of two cylindrical jet - and z - drift chambers in the central region, and of three radial and three planar drift chamber modules in the forward direction. Energy measurements are made by an electromagnetic and hadronic liquid argon calorimeter, the (hadronic) plug calorimeter and the backward electromagnetic calorimeter. Muons are identified using a forward muon detector either side of a magnetised toroid together with the instrumented iron which also acts as a secondary 'tail catcher' calorimeter, to measure hadronic showers leaking from the principal calorimeters.

The time of flight (TOF) system and scintillator walls, located behind the backward calorimeter, are used to veto background events originating from beam-gas and beam-wall interactions. The luminosity is determined from the rate of the Bethe-Heitler [6] process $ep \rightarrow ep\gamma$ measured in the electron tagger and photon tagger located 33 m and 103 m respectively from the interaction region in the backward direction.

Since this data was taken the H1 apparatus has been supplemented by the addition of a silicon vertex detector and forward Roman pots. The backward electromagnetic calorimeter has been replaced with the SPACAL (SPAgetti-CALorimeter) device. This calorimeter has an electromagnetic and a hadronic section both of which are sandwiched with layers of scintillating fibre.

1.3 Tracking: Introduction

The tracking system of H1 provides simultaneous track triggering, reconstruction and particle identification for events emerging from ep collisions. It has been designed to reconstruct jets with high particle densities and to measure the momen-

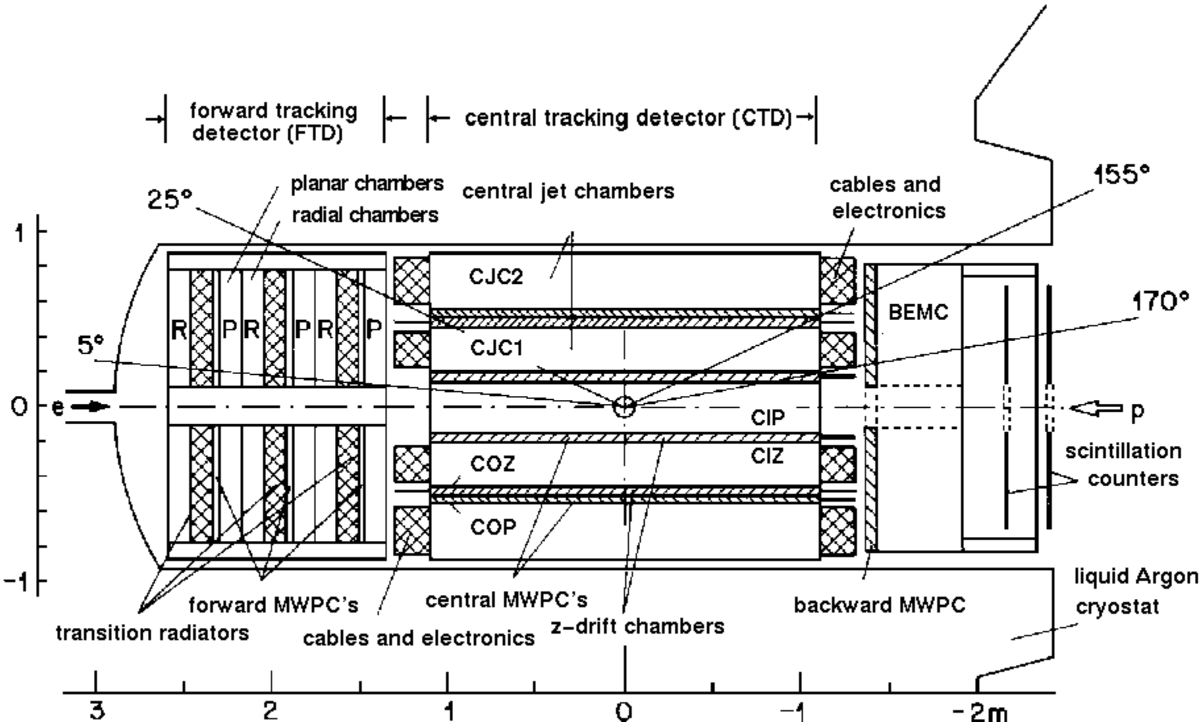

Figure 1.3: *The H1 tracking system (r - z view)*

tum and angles of scattered isolated charged particles to a precision of $\sigma_p/p^2 \approx$ $3\text{x}10^{-3}$ GeV^{-1} and $\sigma_\theta \approx 1$ mr.

Due to the asymmetry between the electron and proton beam energies many charged particles are produced at small angles in the forward direction. To maintain good efficiency for triggering and reconstruction over the whole solid angle, the tracking system is divided into the central and forward regions. The central tracking detector (CTD) and forward tracking detector (FTD) are shown in Figure 1.3.

1.3.1 The Central Tracking Detector

Track reconstruction in the central region is based on two large concentric drift chambers, CJC1 and CJC2, covering the angular region $15^\circ < \theta < 165^\circ$ as shown in Figure 1.3. The chambers have wires strung parallel to the beam axis with the drift cells inclined with respect to the radial direction in the $r - \phi$ (drift coordinate) plane. The space point resolution in the drift plane is 170 μm.

Two thin drift chambers, the central inner (CIZ) and central outer (COZ) z-

chambers complement the measurement of charged track momenta in the central chambers. The CIZ and COZ chambers are situated inside CJC1 and between CJC1 and CJC2 respectively. The polar angles covered by the CIZ and COZ are $16° < \theta < 169°$ and $25° < \theta < 156°$, respectively. These two chambers deliver track elements with typically 300 μm resolution in z and 1-2% of 2π in ϕ. This requires a drift direction parallel to, and hence wires perpendicular to the beam axis.

During the 1993 data runs, the efficiency (and acceptance) of the CJC1 chamber was degraded by the presence of dead wires due to mechanical failure. As a result of dead wire regions up to 15% of the CJC1 was unable to output any signals.

1.3.2 The Forward Tracking Detector

Tracking in the forward region, $5° < \theta < 30°$, is provided by the forward tracking detector. It is comprised of three 'supermodules', each of which is made up of a planar drift chamber, a multiwire proportional chamber (FWPC), a transition radiator (TR) and a radial drift chamber. The layout of these chambers is shown in Figure 1.4. The planar modules provide homogeneous spatial resolution (angular resolution $\sigma_{\theta,\phi} < 1$ mr) in the plane perpendicular to the beam axis, while the radials serve for precise momentum measurement (resolution $\sigma_p/p < 0.003p$).

The planar chambers are separately made up of three drift chamber layers whose wires in any given layer are strung parallel to one another, perpendicular to the beam axis. The angular displacement of the drift chambers (each layer is rotated by 60° in azimuth from the previous layer) allows accurate determination of the $x - y$ coordinates of the forward tracks, enabling central and forward tracks to be linked together. The spatial resolution of the planar chambers has been measured as 150 μm.

Each of the three modules in the FTD contains a radial wire drift chamber as its most forward component. The chambers are azimuthally segmented into 48 drift cells and have wires strung radially outwards.

The FWPC's consist of two planes of wires interleaved with three cathode planes. The cathode pads are radially segmented into 20 rings and azimuthally segmented into sections covering 25° except for the four outer rings where the pads cover 45°. The FWPC's provide fast track information for triggering purposes. A track crossing

Figure 1.4: *Forward tracker overview. Top: cross section in the r, z-plane showing the three supermodules. Bottom: cross section in r, ϕ-plane showing the basic cell structure of each supermodule component in one quadrant (A: planar chamber, B: FWPC, C:TR, D:radial chamber).*

all three or at least two modules of the FWPC has to fall into the polar angle range $6.6° \leq \theta \leq 18.0°$ or $5.1° \leq \theta \leq 21.6°$, respectively. For such tracks an effective timing resolution of 20 ns (FWHM) was measured, well below the required separation of two successive bunches.

The transition radiators are passive units producing X-rays when a charged particle of sufficient momentum passes through them. The TR together with the radial drift chamber which detects the X-rays, is used to discriminate between electrons and pions as these signals are greater for electrons. Using beams of pions and electrons a 90% electron acceptance can be achieved with less than 10% pion contamination for tracks passing through all three modules of the FTD with momenta not greater than 80 GeV.

1.3.3 The Backward Proportional Chamber

The backward multiwire proportional chamber (BPC) has an angular acceptance of $155.5° < \theta < 174.5°$ and serves to identify electrons and to measure precisely their direction. The BPC is equipped with five cathode planes and four anode wire planes, where wire planes are orientated at 45° relative to one another. The wires in each plane are parallel to each other. The space points given by the BPC contribute 0.5 mr to the angular resolution, of the same order as the multiple scattering in the material in front of it. For high energy electrons an efficiency of 87% per plane was measured from extrapolated jet chamber tracks.

1.4 Calorimetry: Introduction

The design of the H1 calorimeter is such that it complements the tracking detectors in measuring jets with high particle densities and discriminating between leptons and hadrons. Furthermore, the calorimeters are needed where measurements from tracking detectors are unavailable, such as the detection of neutral particles. The momentum resolution provided by tracking detectors is degraded for high momentum particles which are deflected less by the magnetic field. Conversely, the resolution of calorimetry improves at higher energies. It is therefore advantageous to combine calorimetry and tracking in order to cover the large momentum range of particles to be measured.

The liquid Argon calorimeter covers the polar angle $4^\circ < \theta < 153^\circ$. Additional coverage is provided by the PLUG calorimeter situated between the beam pipe and the LAr cryostat ($\theta \leq 4^\circ$), a lead scintillator backward electromagnetic calorimeter (BEMC) located in the electron direction after the tracker and covering $151^\circ \leq \theta \leq 177^\circ$ and by the tail catcher system (TC).

The H1 LAr calorimeter has a much finer segmentation than that of the ZEUS calorimeter, but does not have e/π compensation.

1.4.1 The Liquid Argon Calorimeter

The calorimeter is longitudinally subdivided into an electromagnetic section with lead plates and a hadronic section with stainless steel plates as absorbers. The total depth of the calorimeter varies between 4.5 and 8 absorption lengths (λ_I). The calorimeter was optimised for a precise measurement and identification of electrons and for stable energy calibration for electrons and hadrons. The energy resolution σ_E/E for electrons is $12\%/\sqrt{E} \oplus 1\%$ and $45\%/\sqrt{E} \oplus 1\%$ for charged pions as measured with test beams. Throughout this thesis, all energies expressed in resolution formulae are in GeV. The hadronic energy measurement is performed by applying a weighting technique in order to account for the non-compensating behaviour of the calorimeter. The electromagnetic energy scale is known to a precision of 3%, a result obtained by comparing the measured track momentum of electrons and positrons with their corresponding energy deposition in the LAr calorimeter. The overall calibration of the hadronic energy is presently known to 6%, as determined from studies of transverse momentum balance in deep inelastic scattering (DIS) events.

1.4.2 The Backward Electromagnetic Calorimeter

The primary task of BEMC is to trigger and measure scattered electrons in DIS events having a Q^2 value ranging from 5 to 100 GeV^2. In addition the BEMC has to contribute to the measurement of hadronic material emerging from photoproduction and medium to low-x, high-y hadronic final states. A description of the variables Q^2, x and y relevant for DIS kinematics is discussed in chapter 2.

The backward electromagnetic calorimeter (BEMC) consists of 88 multilayer lead-scintillator sandwich stacks, each with a depth of 22.5 electromagnetic radiation lengths (Xo) corresponding to about 0.97 interaction lengths.

The energy resolution of BEMC due to sampling fluctuations is $10\%/\sqrt{E}$. The average noise per stack was measured to be 150 MeV which implies that the noise contribution to the measurement of a typical scattered electron shower is about 450 MeV [2, 7]. The resolution is further affected by stack to stack intercalibration estimated to be around 4%. Thus, for an electron the BEMC resolution can be expressed as:

$$\frac{\sigma_E}{E} = \frac{\sigma_{noise}}{E} \oplus \frac{\sigma_{sampling}}{\sqrt{E}} \oplus \sigma_{constant}$$

where $\sigma_{noise} = 0.45$, $\sigma_{sampling} = 0.1$ and $\sigma_{constant} = 0.04$.

The BEMC resolution is further subjected to a calibration uncertainty of 2%. The energy calibration can be checked by comparing the measured scattered electron energy with the derived energy using the angle of the electron and the angle of the momentum vector of the hadronic final state [8].

About 30% of all hadronic flow into the BEMC will not produce signals above threshold due to the low interaction length of the device. The hadrons which do interact typically deposit about 30% of their energy in the BEMC. By combining energy measurements in the BEMC and the instrumented iron, a hadronic energy resolution of about $80\%/\sqrt{E}$ is determined from detailed simulation studies.

1.4.3 The Plug calorimeter

The plug calorimeter (PLUG) has been designed to close the gap of acceptance for the energy flow measurements between the beam pipe ($\theta \approx 0.6^\circ$) and the forward part of the LAr calorimeter ($\theta \approx 3.0^\circ$). This is important for charged current interactions where the event kinematics can only be determined from the measured hadronic final state. The plug consists of 9 layers of copper absorber interspersed with 8 layers of silicon detectors. The total depth of the plug is roughly $4.3\lambda_I$.

Due to the lack of lateral and longitudinal shower containment and coarse sampling the hadronic energy resolution of the plug has been measured as $150\%/\sqrt{E}$.

However, data taken by the plug calorimeter is not used in any part of the physics analysis presented in this thesis.

1.4.4 The Instrumented Iron

One of the uses of the iron return yoke is to measure the hadronic energy flow leaking out of the LAr calorimeter, hence it is usually termed the (hadronic) tail catcher. It is also used for hadronic detection in the backward region, behind BEMC as well as muon detection

In order to meet these requirements the iron yoke is instrumented with streamer tubes and readout pads, placed in the gaps of alternating layers of iron.

The streamer tubes and the readout pads are orientated along the beam axis in the barrel region ($25^\circ < \theta < 130^\circ$) and vertically in the forward and backward regions. The tail catcher covers the angular region $5^\circ < \theta < 175^\circ$ and has a depth of about $4.5\lambda_I$. The hadronic energy resolution of the tail catcher has been measured as $150\%/\sqrt{E}$.

1.5 The Forward Muon Detector

The forward muon detector (FMD) is designed to measure energetic muons with momenta between 5 and 200 GeV/c in the angular range $3^\circ < \theta < 17^\circ$. The detector consists of three double layer drift chamber planes mounted on either side of a toroidal magnet and is not affected by the axial field of the H1 magnet. The lower limit is given by the amount of material that the muons have to penetrate and the influence on the momentum resolution while the upper limit is set by the magnetic field strength of the toroid and the spatial resolution of the drift chambers.

1.6 Luminosity System and Electron Tagger

The luminosity is determined from the rate of the Bethe-Heitler events $ep \rightarrow ep\gamma$ which have a large and precisely calculable cross section [9]. The main source of background is bremsstrahlung from the residual gas in the beam pipe, $eA \rightarrow eA\gamma$ which has a larger cross section and an almost identical signature. The background is measured experimentally using electron and proton pilot bunches. The luminosity is calculated as:

$$\mathcal{L} = \frac{R_{tot} - (I_{tot}/I_0)R_0}{\sigma_{vis}}$$

where R_{tot} is the total rate of the bremsstrahlung events, R_0 is the rate in the electron pilot bunches, I_{tot} and I_0 are the corresponding electron beam currents and σ_{vis} is the visible part of the $ep \to ep\gamma$ cross section, taking into account the acceptance and the trigger efficiency of the whole system.

The luminosity monitor detects scattered electrons and outgoing photons in coincidence. Therefore it contains two arms, the electron tagger (ET) and the photon detector (PD). The detectors are situated close to the beam pipe and very far away from the interaction region because the angular distribution for both the electrons and the photons are strongly peaked in the direction of the primary e-beam. At 30 GeV the polar angles are of the order of $\theta \simeq \mathcal{O}(m/E) \simeq 17\mu$ radians. The general view of the luminosity system is shown in Figure 1.5. The ET and PD are situated at $z = -33$m and $z = -103$m, respectively.

The scattered electrons are deflected into the ET by a set of warm quadrupoles and a bending magnet located in the region -5.8 m $< z < -23.8$ m. The photons leave the beam pipe via the photon exit window at $z = -92.3$ m where they enter the photon tagger.

1.7 Time-of-Flight Counters and The Veto Wall

The scintillator arrays discussed in this section are located in the backward region of the detector and designed to reject background, associated with proton beam interactions, at the first level trigger.

The time of flight device (ToF) is located upstream of the interaction region at $z \approx -2$ m. This position represents a compromise between good coverage of the detector and time resolution. The mean separation of particles from proton background and those from ep collisions at this point is $\sim$ 13 ns. ToF is a hodoscope consisting of two planes mounted perpendicular to the beam pipe. Each wall consists

Figure 1.5: *The layout of the H1 luminosity system.*

of 3 cm plastic scintillator sandwiched between 6.5 mm ($1.1X_0$) of lead. The lead absorber both protects the scintillator from damage and limits the number of triggers from synchrotron radiation. The ToF is readout by 24 photomultiplier tubes. These signals are discriminated and strobed in three time windows: background, interaction and global. A trigger signal is sent to the central trigger logic (CTL) if a logical OR between the two walls in any of the three time windows gives a coincidence. Most important is the background trigger which is used to suppress triggers from other subdetectors, leading to an overall 99% decrease in the overall trigger rate, and subsequent reduction in deadtime. The interaction and global ToF signals are used in conjunction with other trigger elements to form physics and cosmic ray triggers [10]. The total time taken for a trigger decision to reach the CTL is 250 ns. The device as a whole has a time resolution of 4 ns, while individual counters have a resolution of the order of 2 ns.

In addition to the ToF device two double scintillator veto walls are installed at a distance of $z = -6.5$ m (large veto wall) and $z = -8.1$ m (small veto wall).

1.8 Triggering and Data Acquisition

The H1 multilevel trigger is designed to distinguish electron-proton events from the high rate of beam-induced background processes. On the basis of their different topologies, ep events such as deep inelastic scattering and photoproduction can be separated. To minimise dead-time and cope with the large bunch crossing rate, the trigger system is 'pipe-lined' i.e., the output signals from the subdetectors are fed into front-end digitising units where they are stored. The output signals from the subdetectors are also fed to the subdetector trigger where they are converted into 'trigger elements'. These trigger elements are sent to the central trigger logic where they are combined to provide the 'level 1' (L1) and 'level 2' (L2) subtriggers. The level 1 trigger consists of nine different trigger elements and the corresponding subtriggers can be used to select possible physics interactions, as well as events useful for detector studies such as cosmic ray events for tracking and calorimeter calibration. If the event is worth further examination, the central trigger logic sends out an 'L1KEEP' signal which disables all detectors, and the data in their pipelines is read out. The final L1 trigger decision is usually made 24 beam crossings (2.5 μs) after the real interaction event time. Through pipelining, the L1 decision introduces no deadtime to the experiment and therefore, no loss of possible physics events. Deadtime arises from readout after the event is accepted for further reconstruction at higher levels if required. The L2 trigger analyses the event in more detail and a decision whether to keep or reject the event is made within 20 μs after the L1KEEP signal. If the event is kept then the data from the detector output is read out from the pipelines, otherwise the detector is re-enabled. The output signals are then passed onto the 'level 3' (L3) trigger which makes a more complex study based on topologies and produces a decision after a few hundred μs. The events which survive the level 2 and 3 triggers are then taken to the central data aquisition system so that a level 4 (L4) decision can be made.

The data aquisition (DAQ) system reads out information in parallel from each subdetector system before the the 'event builder' combines the data into a full event record. These full events are then passed to the L4 trigger. Data compression is carried out online to reduce the large volume of raw data (roughly 3Mbytes) down to event sizes ranging between 50 and 100 Kbytes. The L4 trigger performs a simplified version of the full event reconstruction online to provide a powerful discrimination on the basis of event topology and class of physics event. Events accepted by L4 are then stored onto tape where they are fully reconstructed and put onto output tapes. Approximately 1 ms elapses from the L1Keep signal before all the data is available to the L4 trigger after which the detector is re-enabled.

During the 1993 data taking period, the H1 trigger system did not include the L2 and L3 triggers. Since the maximum rate for sending events to the DAQ is 50 Hz, the absence of these triggers meant that the L1 trigger could only put out events at a rate of 50 Hz.

1.9 The H1 Software Chain

Once an event has successfully passed the L4 trigger, it is fully reconstructed by the H1 reconstruction software H1REC [11] and then put onto 'production output' (POT) tapes. The POT data contain a large fraction of background events which passed the online triggers and so further event reduction is done using software algorithms which look for event characteristics associated with types of physics processes. Events which pass these offline selections are assigned a (physics) class number and are put onto data summary tapes (DST). This level of data selection is sometimes referred to as 'level 5' (L5).

The physics analysis package H1PHAN [12] uses the reconstructed data from simulated data or real data (POT's or DST's) and converts them into meaningful 'physics' objects, such as four-vectors. It provides the routines to allow determination of event kinematics, simple particle identification and jet reconstruction. The user must provide their physics analysis code which can then be used within the framework of H1PHAN.

The H1 simulation program H1SIM [13] is based on the GEANT [14] package. H1SIM provides an accurate detector simulation which can then be used to fine tune physics analysis programs, study trigger efficiencies and study energy flow properties in the different calorimeters. It simulates all the physics associated with the passage of particles through the various subdetectors. H1SIM produces response banks which have the form of those produced by the real detector, the output of which can then be reconstructed using the H1REC software chain.

During 1993 data runs the CJC1 detector contained dead wire regions. Therefore, in order to compare the real data with Monte Carlo simulations, the dead regions are accounted for during the reconstruction of the H1SIM data. The reconstruction of the simulated CJC data simply removes any hits on the observed dead wires. This allows the performance of the CJC1 detector to be better understood.

Chapter 2

Physics at HERA

2.1 Introduction

The *ep* collider HERA at DESY, in which 27.5 GeV electrons (positrons) collide with 820 GeV protons, gives access to a new kinematic region of lepton nucleon scattering with a rich physics potential. The large centre-of-mass energy associated with these collisions increases the kinematic phase space in momentum transfer Q^2 by two orders of magnitude and, at low Q^2, lowers the detectable Bjorken x by one order of magnitude compared to fixed target experiments.

This chapter will define the kinematics relevant to this thesis and give a brief description of the principle types of physics that are possible at HERA.

2.2 Kinematics

The kinematics of the inclusive deep inelastic scattering (DIS) process $ep \to e'(\nu)X$ at fixed centre-of-mass energy, $\sqrt{s}$, is determined by two independent variables, conventionally chosen from Q^2 and the scaling quantities x and y. Q^2 is the negative four-momentum transfer squared between the incoming and outgoing lepton, x in the naïve quark parton model (QPM) is the momentum fraction of the proton carried by the struck parton (Bjorken x), and y is the fraction of the energy transferred from the initial electron to the hadronic system in the the rest frame of the incoming proton. The lowest order diagram for this process is depicted in figure 2.1 and defines the four vectors involved in the kinematics. Since the H1 experiment at HERA measures both the scattered electron and the hadronic final state produced between the struck

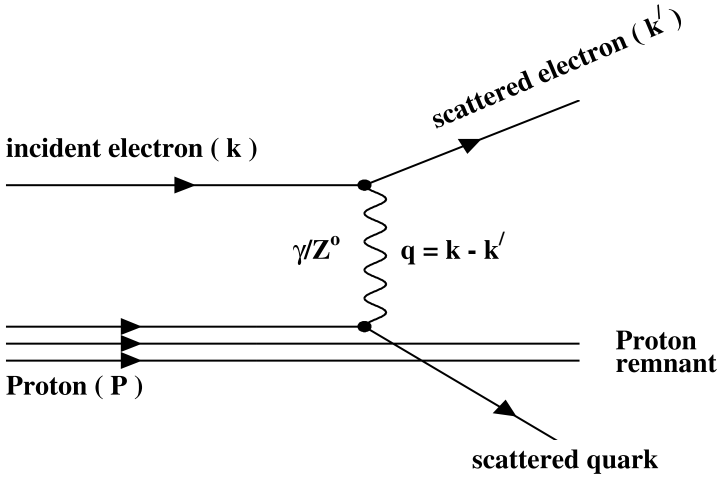

Figure 2.1: *Born term diagram for deep inelastic scattering.*

parton and the proton remnant, the collision kinematics are over-constrained and thus can be determined from electron variables, hadronic variables or a mixture of both. These methods are discussed further in chapter 4.

In Lorentz-invariant notation the kinematic variables are defined as follows:

$$Q^2 = -q^2 = -(k - k')^2 \tag{2.1}$$

$$y = \frac{P \cdot q}{P \cdot k} \tag{2.2}$$

$$x = \frac{Q^2}{2P \cdot q} \tag{2.3}$$

where

- k is the four-momentum of the incoming electron,
- k' is the four-momentum of the scattered electron,
- P is the four-momentum of the incoming proton and,
- q is the four-momentum of the exchange boson.

Neglecting the proton mass M, the invariant mass squared of the hadronic final state, W^2, in terms of the variables defined in equations 2.1, 2.2 and 2.3, is given by

$$W^2 = (P+q)^2 \approx Q^2 \left(\frac{1-x}{x}\right) \tag{2.4}$$

At HERA the centre-of-mass energy squared, neglecting the mass of the proton, is defined as

$$s = (k+P)^2 \approx 4E_e E_P \tag{2.5}$$

where E_e and E_P are the energies of the incoming electron and proton, respectively. With the present HERA beam energies s reaches 87600 GeV^2. Due to this high centre-of-mass energy using,

$$Q^2 = sxy \tag{2.6}$$

x values down to $\sim 10^{-4}$ in the deep inelastic regime ($Q^2 > 10$ GeV^2) can be accessed at HERA. For small Bjorken x values, y can be approximated to $\sim W^2/s$ using equations 2.4 and 2.6.

The kinematic variables in charged-lepton nucleon scattering are traditionally determined from the polar angle θ and the energy E_e' of the scattered lepton through the relations

$$Q^2 = 4E_e E_e' \cos^2\frac{\theta}{2}, \tag{2.7}$$

$$y = 1 - \frac{E_e'}{E_e}\sin^2\frac{\theta}{2} \tag{2.8}$$

and the Bjorken variable x is calculated using equation 2.6.

Polar angles, such as θ, are measured relative to the the proton beam direction, termed the "forward direction" (corresponding to $\theta = 0°$ throughout this thesis). The kinematics for the scattered electron in the (x, Q^2) plane is shown in figure 2.2. For a large region in the plane, corresponding roughly to $y < 0.1$, the energy of the scattered electron is close to the incident electron beam energy. This leads to a peak in the scattered electron energy spectrum, termed the "kinematic peak", which serves beneficially for calibration purposes.

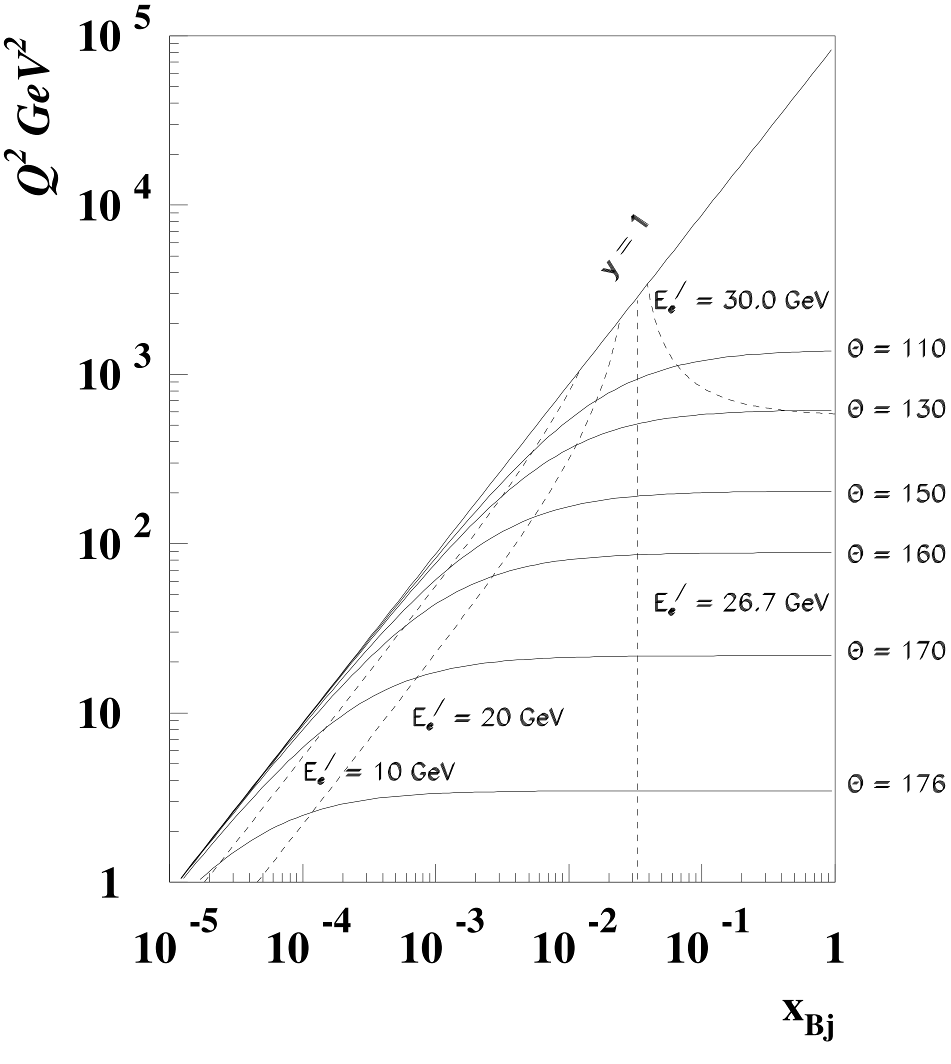

Figure 2.2: *Lines of constant energy and scattering angle for the scattered electron in the* (x, Q^2) *plane for deep inelastic scattering events.*

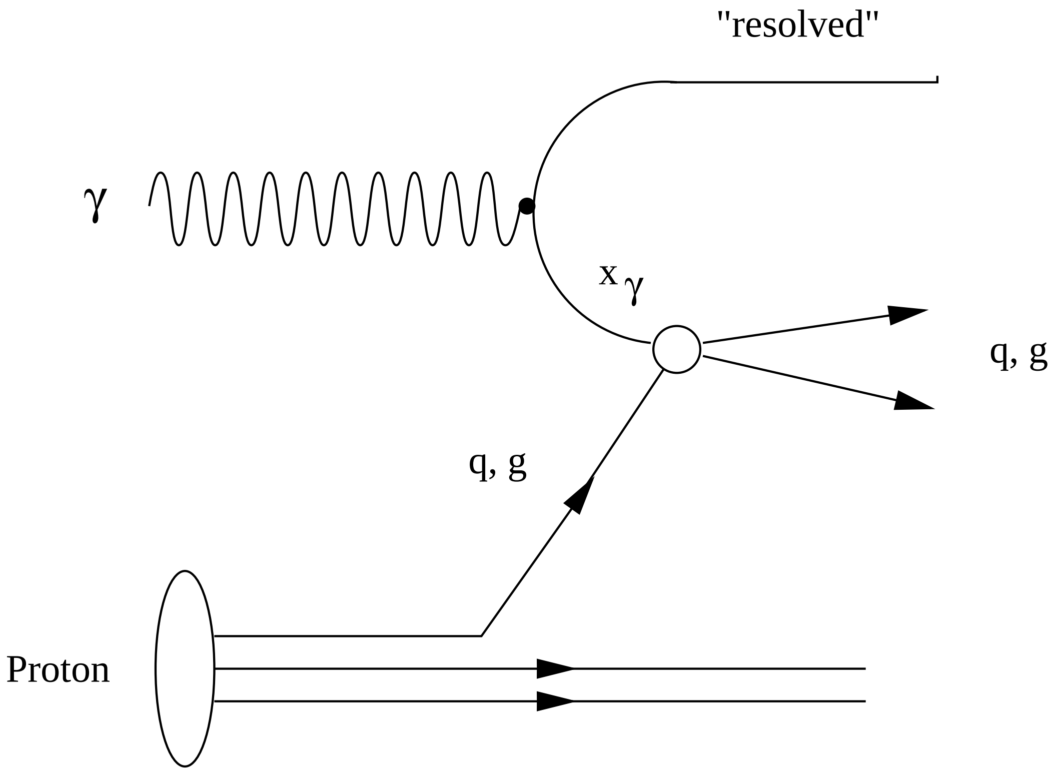

Figure 2.3: *Leading order QCD hard γp interaction of the constituents of a "resolved" photon with the partons from the proton, leading to at least two high p_T and two low p_T remnants from the photon and proton.*

2.3 Photoproduction

The interaction of electrons and protons at HERA are dominated by photoproduction processes [15]: electrons scatter through small angles and emit quasi-real photons, which then interact with the protons. Due to the large cross section, photoproduction constitutes a major background for DIS studies. Phenomenologically, γp scattering can be viewed as a superposition of several production mechanisms, related to the "structure" of the photon [16]. The bulk of the cross section is "soft", leading to low p_T particle production, described by the vector dominance model (VDM). In photoproduction, however, high p_T particles can also be produced. They are thought to result from a hard scattering process of the hadronic constituents of the photon ("resolved photon"), characterised by a photon structure function $F^{\gamma}(x_{\gamma})$. The corresponding lowest order diagram is shown in figure 2.3.

2.4 Deep Inelastic Scattering

Precise measurements in DIS of charged [17, 18] and neutral [19] leptons on nuclear matter have been essential for our understanding of the partonic substructure on the nucleon. While QCD in its present form cannot supply information on the parton distribution functions inside the nucleons, it does predict their evolution in Q^2.

Parton densities are conventionally evolved in Q^2 according to the linear DGLAP equation [20, 21], starting from known input distributions in x at fixed Q^2. DIS data for $x > 10^{-2}$ are successfully described by the DGLAP equation. However, in the small x ($\sim 10^{-4}$) regime at HERA the DGLAP evolution may not be applicable due to a sizeable contribution from $\ln(1/x)$ terms that are discarded in the summation.

Alternatively, the BFKL equations [22] employ an evolution in x. Measurements of the structure function F_2 impose constraints on the parton distributions, and at HERA, F_2 is seen to rise with decreasing x [23] in accord with expectations from the BFKL equations. However, such a behaviour could also be mimicked by the conventional DGLAP dynamics [24].

For momentum transfers small compared to the mass of the Z^0 the cross section for deep inelastic electron-proton scattering in lowest order (Born cross section) can be expressed in terms of a single structure function F_2 and the ratio of the cross sections for longitudinally and transversely polarized photons on protons, $R = \sigma_L/\sigma_T$:

$$\frac{d^2\sigma}{dx \cdot dQ^2} = \frac{2\pi\alpha^2}{Q^4 x}\left(2(1-y) + \frac{y^2}{1+R}\right) F_2^P(x, Q^2) \tag{2.9}$$

The ratio R [5] which in principle also depends on x and Q^2, has not yet been measured at HERA and is expected to be sizable at large y.

2.5 Transverse Energy Flow - E_T

More direct searches for BFKL dynamics look into the hadronic final state. In the low x domain, the region away from the expected current jet towards the proton remnant, as shown in figure 2.4, is of particular interest in the analysis of the energy

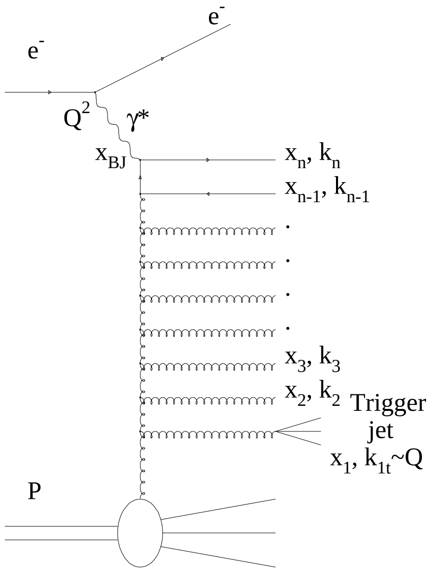

Figure 2.4: *Parton evolution in the ladder approximation.*

flow [25], as it may be the region most sensitive to new effects based on BFKL dynamics.

In the DGLAP picture, the parton cascade is evolved in Q^2 leading to a strong ordering in transverse momenta $k_{Tn}^2 >> k_{Tn-1}^2 >> ... >> k_{T1}^2$, while there is only a soft ordering for the longitudinal parton momentum scaled by the proton momentum, $x_n < x_{n-1} < ... < x_1$. In the BFKL scheme the cascade follows a strong ordering in fractional momentum $x_n << x_{n-1} << ... << x_1$, while there is no ordering in transverse momentum [26], i.e, the transverse momentum follows a kind of random walk in k_T space. As a consequence, BFKL evolution is expected to produce more transverse energy E_T than DGLAP evolution [27, 28] in the region between the struck quark and the remnant.

Figure 2.5 shows the mean transverse energy flow E_T as a function of the pseudorapidity $\eta = -\ln\tan(\theta/2)$ in the laboratory system for low x and moderate $< Q^2 >\approx 15$ GeV^2. The energy flow exhibits an enhancement around the current direction in the central region and levels off at about 2 GeV per unit of rapidity

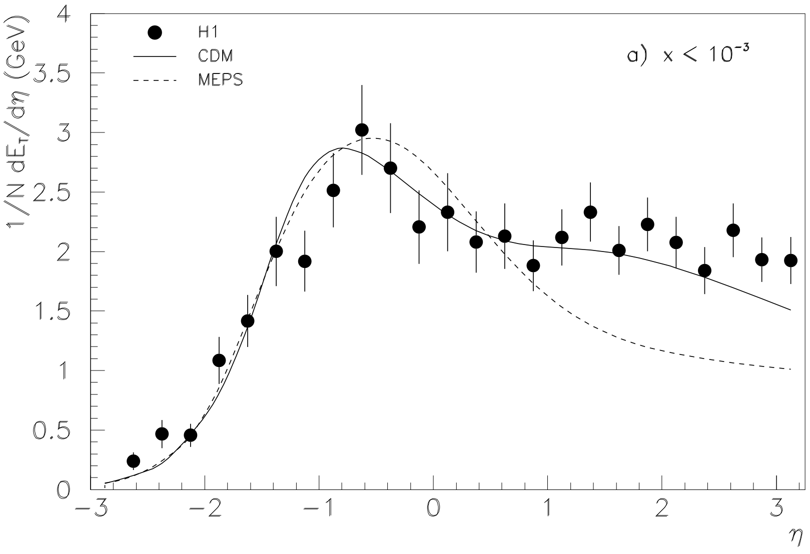

Figure 2.5: *Transverse energy flow E_T in the laboratory system as a function of pseudorapidity η, measured in the calorimeter, for events with $x < 10^{-3}$ The proton direction is to the right (positive values of η).*

towards the proton remnant at large positive η values. The MEPS model (matrix elements matched to parton showers) produces considerable less energy in the forward region than observed. The colour dipole model (CDM) is closer to the data on account of its description [29, 30] of gluon emission which is believed to be similar to that of BFKL evolution.

2.6 Large Rapidity Gap Events

A typical DIS event exhibits energy flow associated with the direction of the proton remnant i.e, large values of η as was shown in figure 2.5. This flow presumably results from the fragmentation of the proton remnant, or in terms of the colour string picture, from the fragmentation of the colour string between the struck quark and the proton remnant. However, both H1 [31] and ZEUS [32] have reported a class of DIS events in which there is no particle flow in a large interval of rapidity around

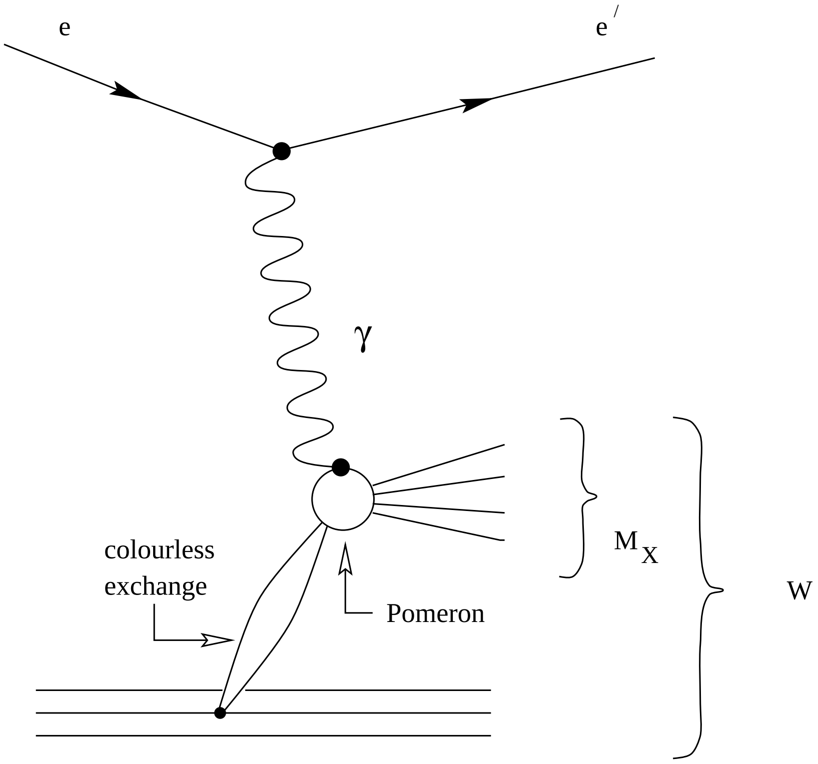

Figure 2.6: *Diagram for a deep inelastic event where the virtual photon scatters off a colourless object (Pomeron) inside the proton. The Pomeron has a mass M_X less than the total hadronic mass W.*

the proton direction. The observation of these rapidity gap events, unexpected in the context of the colour string picture between the quark and the proton remnant, points towards a mechanism in which the virtual photon interacts with a *colourless* object, sometimes called the Pomeron, emitted from the proton as shown in figure 2.6.

Figure 2.7 shows the distribution of the gap in pseudorapidity, measured with respect to the forward edge of the LAr calorimeter ($\eta = 3.65$) to the first significant energy deposition, for all DIS events. Comparison with a standard DIS Monte Carlo simulation (LEPTO) reveals a clear excess of events in a plateau beyond $\Delta\eta \approx 2$. Events with such a rapidity gap amount to about 6% of the deep inelastic sample.

2.7 QCD Models

In LEPTO [33], QCD processes are calculated up to $\mathcal{O}(\alpha_s)$ according to exact first order matrix elements (ME). The QPM corresponds to turning $\mathcal{O}(\alpha_s)$ matrix ele-

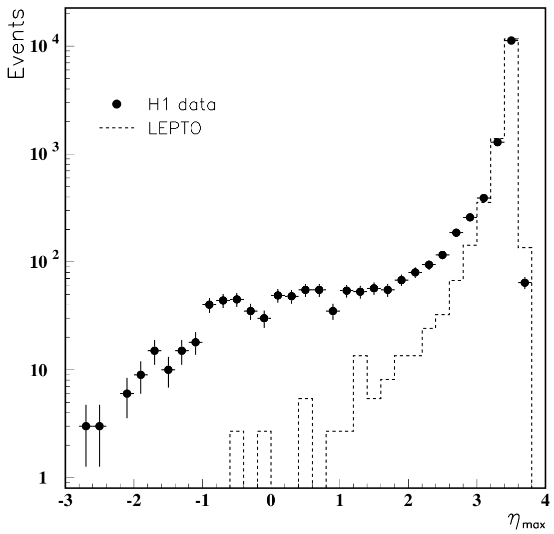

Figure 2.7: *Distribution of the measured η_{max} for all DIS events together with the expectation from the LEPTO Monte Carlo simulation normalised to the peak at high η_{max}.*

ments off. Higher order contributions are simulated in the leading logarithm approximation and known as the parton shower (PS) approach. In an incoherent approximation, the struck quark can emit partons either before or after the parton boson vertex. As the quark is radiating the initial state shower - before the boson vertex - it becomes more off shell or negatively virtual. After the interaction the quark becomes positively (time-like) off-shell and returns to the mass shell by radiating the final state shower. The amount of gluon radiation depends on the scale of virtuality which can be chosen to be either Q^2 or W^2, sometimes referred to as PS(Q^2) and PS(W^2), or a function of both, $Q{\cdot}W$. Since $< Q^2 >$ is much smaller than $< W^2 >$ in the experiment, PS(W^2) will predict much more gluon radiation than PS(Q^2). The combination of the two approaches (ME+PS) gives the first order parton emission plus the higher order emissions through parton showers. The probabilities for all partonic subprocesses are matched to avoid double counting. The hadronisation into hadrons is performed with the LUND string model [34] as implemented in JETSET [35].

Chapter 3

QCD Models of the Hadronic Final State

3.1 The Quark Parton Model

The Quark Parton Model (QPM) provides the simplest description of the partonic final state in Deep Inelastic Scattering (DIS). Neglecting Quantum Chromodynamics (QCD), DIS can be viewed as a two stage process. The first stage consists of an elastic scattering of the lepton by a single valence or sea quark which carries a fraction x of the proton four-momentum, P, by the exchange of a virtual boson.

The second stage of the DIS process is the break up and recombination of the partons to form hadrons. This is normally referred to as fragmentation of the parton and takes place such that there is a colour flow between the struck parton and proton remnant partons.

The final hadronization process is a direct consequence of the colour confinement property of QCD; the struck parton is a coloured object and thus it cannot be observed in isolation. The hadronic final state consists of the 'current jet' from fragmentation of the struck parton, and the 'target jet' formed from the spectator (proton remnant) partons.

DIS experiments at SLAC in the late 1960s provided the first evidence that nucleons are composed of pointlike constituents, known as partons. The structure of the nucleus can be probed using a virtual photon of sufficiently high Q^2, equivalent to enhancing the spatial resolution within the proton. The proton structure function, $F_2(x, Q^2)$ was observed to be roughly independent of Q^2 at a given value of x [36].

This scaling behaviour, known as *Bjorken scaling hypothesis*, was interpreted as evidence for the existence of pointlike partons.

In the absence of electro-weak interactions the differential cross-section for the DIS process can be written in terms of two dimensionless structure functions, $F_1(x,Q^2)$ and $F_2(x,Q^2)$:

$$\frac{d^2\sigma}{dQ^2dx} = \frac{4\pi\alpha^2}{xQ^4}[(1-y)F_2(x,Q^2) + xy^2F_1(x,Q^2)] \tag{3.1}$$

Callan and Gross showed that the structure functions should be related [36]:

$$2xF_1(x) = F_2(x) \tag{3.2}$$

reflecting the hypothesis that the charged constituents of the proton are spin $\frac{1}{2}$ particles. This result was confirmed experimentally at SLAC. Equation 2.9 follows from equation 3.1 by setting $R = 0$ and using the relation in 3.2.

Evidence that the partons carry fractional electric charge came from the comparison of F_2 measured in neutrino-nucleon scattering and electron-nucleon scattering which confirmed that $F_2^{\nu N} \simeq \frac{18}{5}F_2^{eN}$, a result expected for quarks with fractional charge.

The experimental verification of Bjorken scaling, the Callan-Gross relation and the fractional electric charges in DIS provided compelling evidence that the partons within the proton are quarks. In the Feynman infinite momentum frame where the momentum of the proton is much greater than its mass, relativistic time dilation slows down the rate at which the partons interact with one another within the proton. During the short time interval in which the photon interacts with the parton, $t \sim \hbar/Q$, it is essentially a free particle within the proton and deep inelastic ep scattering can be interpreted as elastic electron-parton scattering.

The Quark Parton Model was developed on the basis of these results. In this model the proton instantaneously consists of three non-interacting 'valence' quarks (uud) accompanied by many quark-antiquark pairs, mainly $u\overline{u}$, $d\overline{d}$ and $s\overline{s}$ known as sea-quarks. In the QPM each parton i carries a momentum fraction x_i of the proton's 4-momentum and is assumed to be massless. The structure function, F_2, is then interpreted as:

$$F_2(x) = \sum_i e_i^2 x f_i(x) \tag{3.3}$$

where $f_i(x)$ is the probability that parton i with electric charge e_i carries a fraction x of the proton's momentum.

3.2 Quantum Chromodynamics

The basis for the QPM was that the virtual photon scatters off a 'free' quark, i.e, there was no interaction between the quarks over the short-time scale during the scattering. QCD provides the theoretical justification for the QPM in that over the short distance-time scales involved, the strong coupling constant, α_s, becomes very small and thus the quarks are asymptotically free. However, over longer time-scales (lower Q^2), α_s becomes large enough such that quarks cannot be considered as 'free' (noninteracting) partons. The running Q^2 dependence of the coupling constant arises due to the anti-screening effects associated with gluon-gluon interactions. In the leading logarithmic approximation the running coupling constant of QCD is expressed as

$$\alpha_s(Q^2) = \frac{12\pi}{(33 - 2N_f)\ln(Q^2/\Lambda^2_{\overline{MS}})} \tag{3.4}$$

The constant $\Lambda_{\overline{MS}}$ is the one fundamental constant of QCD that must be determined from experiment. It governs the dependence of the dimensionless α_s on energy and characterises the scale at which α_s becomes sufficiently large that perturbative QCD breaks down. This constant represents the boundary between the world of quarks and gluons and the physical world of hadrons. It can be seen from equation 3.4 that asymptotic freedom can only occur if the number of active flavours, $N_f \leq 16$. Due to the break down of perturbative techniques in the limit $Q \sim \Lambda_{\overline{MS}} \sim 100 - 400$ MeV, the fragmentation of quarks and gluons occur at too low a value of Q^2 to be treated perturbatively. Consequently, phenomenological models are needed to describe these process and will be discussed in section 3.9

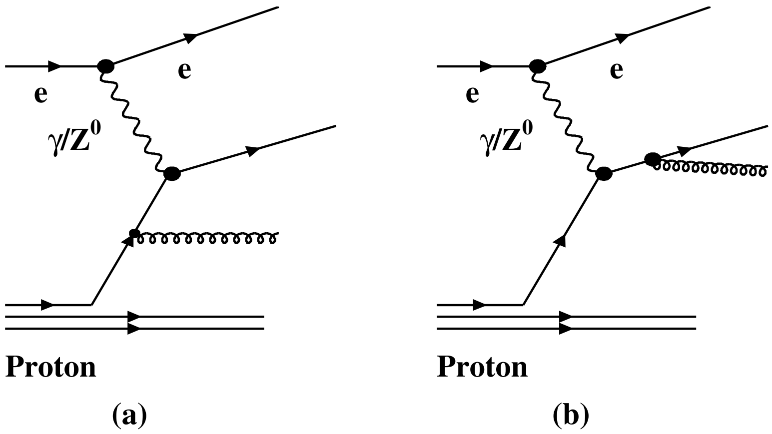

Figure 3.1: *The Feynman diagrams for $\mathcal{O}(\alpha_s)$ (a) initial state QCD Compton and (b) final state QCD Compton processes.*

3.3 Matrix Elements

Within the framework of perturbative theory, matrix elements calculated to fixed order in α_s offer an exact description of parton emissions. Although matrix elements for DIS have been recently calculated up to second order [37], only the first order calculations have been incorporated into the Monte Carlo generators. Such interactions allow for the possibility that the quark may radiate a gluon before or after being struck by the virtual photon $\gamma^* q \rightarrow qg$. Another possible interaction, neglected in the QPM, is that a gluon in the proton can contribute to DIS by producing a $q\overline{q}$ pair, one of which couples to the exchanged virtual boson $\gamma^* g \rightarrow q\overline{q}$. These leading-order processes are hereafter known as, QCD Compton (QCDC) and Boson-Gluon Fusion (BGF) respectively. These processes are shown in figure 3.1 and figure 3.2 and the matrix elements for these diagrams have been calculated exactly.

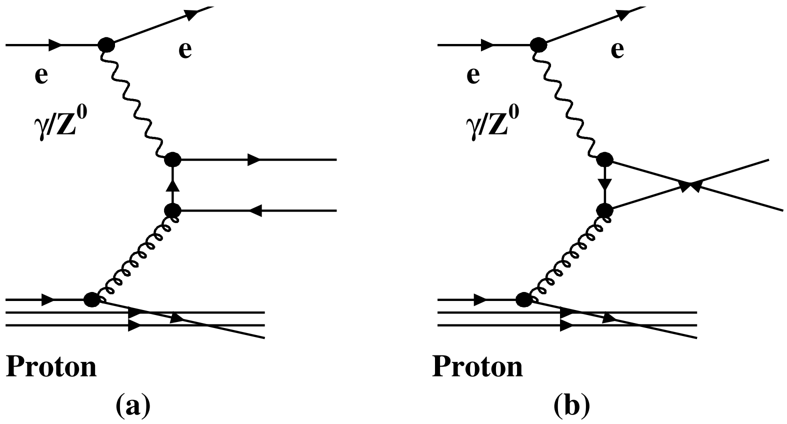

Figure 3.2: *Feynman diagram for Boson-Gluon Fusion.*

3.4 Leading Logarithmic Parton Showers

In DIS the struck quark can emit gluons before and after the boson vertex. In the parton shower approach this process gives rise to initial and final state parton showers, as illustrated in figure 3.3. In the initial cascade a parton, typically close to the mass-shell, radiates a gluon and becomes (further) off the mass-shell. After each successive branch the parton becomes increasingly off-shell with a space-like virtuality ($m^2 < 0$).

Finally the resulting spacelike quark is then struck by the boson and turned into a quark that is either on the mass-shell or has a time-like virtuality ($m^2 > 0$). This quark can further radiate gluons - depending on its virtuality - and gives rise to the final state parton shower. In contrast to the initial cascade, the virtuality of the struck quark in final state shower decreases after each branching.

In the leading logarithmic approximation, the probability for a branching $a \rightarrow bc$ to take place during a small change $dt = dQ^2_{evol}/Q^2_{evol}$ of the evolution parameter

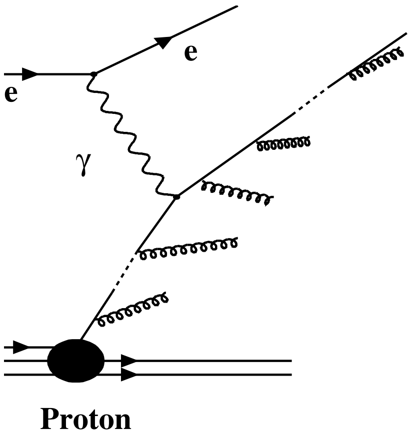

Figure 3.3: *The parton shower picture for DIS. Gluon emission before and after the boson vertex gives rise to the initial and final state parton showers respectively.*

$t = \ln(Q^2_{evol}/\Lambda^2)$ is given by the Altarelli-Parisi equations [21]

$$\frac{d\mathcal{P}_{a\to bc}}{dt} = \int dz \frac{\alpha_s(Q^2)}{2\pi} \mathcal{P}_{a\to bc}(z) \tag{3.5}$$

$\mathcal{P}_{a\to bc}(z)$ are the Altarelli-Parisi splitting kernels and describe the probability that a parton of four-momentum zp will be found in what started as a parton of initial momentum p before the branching. The splitting functions are

$$\mathcal{P}_{qq}(z) = \frac{4}{3}\left[\frac{1+z^2}{1-z}\right] \tag{3.6}$$

$$\mathcal{P}_{qg}(z) = \frac{1}{2}\left[z^2 + (1-z)^2\right] \tag{3.7}$$

$$\mathcal{P}_{gq}(z) = \frac{4}{3}\left[\frac{1+(1-z)^2}{z}\right] \tag{3.8}$$

$$\mathcal{P}_{gg}(z) = 6\left[\frac{(1-z)}{z} + z(1-z) + \frac{z}{(1-z)}\right] \tag{3.9}$$

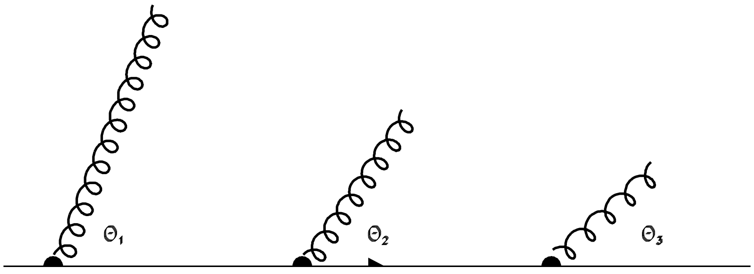

Figure 3.4: *Angular Ordering of gluon emissions in the cascade :* $\theta_1 > \theta_2 > \theta_3$

3.4.1 Angular Ordered Parton Cascades

Coherence effectively restricts successive gluon emissions to decreasingly smaller angles, known as angular-ordering, as shown in figure 3.4. In order to explain this phenomenon, an analogy is drawn with soft photon bremsstrahlung from a relativistic e^+e^- pair. Figure 3.5 shows an e^+e^- pair with an opening angle of $\theta_{e^+e^-}$ created by pair-production.

A photon with four momentum k is emitted by the electron at an angle $\theta_{\gamma e^-}$ with respect to the e^- direction. The time taken for the photon emission, hereafter referred to as the formation time, t_{form}, can be estimated as the life-time of the intermediate virtual electron (p_1) using the uncertainty relation. The virtual mass of this intermediate electron, $M = \sqrt{p_1^2} = \sqrt{(p_e + k)^2}$, provides an estimate of the time interval required for the radiated photon to be formed [38].

$$t_{form} \sim \frac{1}{M}\gamma \sim \frac{|\vec{p_e}|}{(p_e + k)^2} \sim \frac{1}{|\vec{k}|}\frac{1}{\theta_{\gamma e}^2} \sim \frac{\lambda_\perp}{\theta_{\gamma e}} \tag{3.10}$$

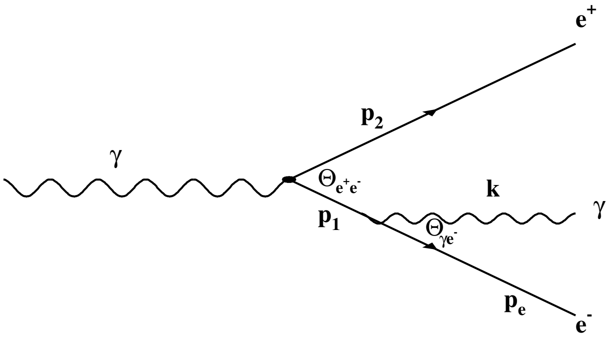

Figure 3.5: *Bremsstrahlung radiation of a photon after e^+e^- pair-production.*

where γ is the Lorentz dilation factor $\sim E/M$, $\lambda_\perp$ is the transverse wavelength of the radiated photon, and the angle $\theta_{\gamma e}$ and mass of the final-state electron are assumed to be small.

During this time the e^+e^- pair separates a transverse distance

$$\rho_\perp^{e^+e^-} \sim \theta_{e^+e^-} t_{form} \sim \theta_{e^+e^-} \frac{\lambda_\perp}{\theta_{\gamma e}} \tag{3.11}$$

If the photon were emitted at large angles such that $\theta_{\gamma e} > \theta_{e^+e^-}$, the separation of the e^+e^- pair would be smaller than the wavelength of the photon i.e, $\rho_\perp^{e^+e^-} < \lambda_\perp$. In such cases the emitted photon cannot resolve the internal structure of the e^+e^- pair and probes only its total electric charge which is zero. The emission of photons at large angles is therefore strongly suppressed. This phenomenon was first observed in cosmic ray studies [39] and is known as the 'Chudakov effect'.

A similar physical picture can be drawn for QCD cascades in which a soft gluon is radiated from a quark or anti-quark as shown in figure 3.6. The net colour charge probed by the coherent radiation of soft gluons by an unresolved pair of quarks is no longer zero as in the QED case and the radiation acts as if it were emitted from the parent gluon *imagined* to be on shell.

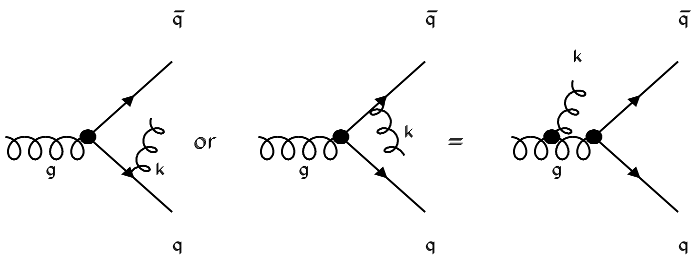

Figure 3.6: *Wide-angle emission of a soft gluon (momentum k) off a quark or anti-quark behaves as if the emission came off the parent gluon imagined to be on the mass-shell.*

The suppression of soft (low p_T) gluon emissions at wide angles leads to a modification of the inclusive momentum spectrum of partons within the cascade, the so-called "hump-backed plateau" [40]. The effect of colour coherence on the energy distribution is shown figuratively in figure 3.7 and compared to predictions obtained from an incoherent model. Colour coherence also leads to the suppression of large multiplicity events as well as a modified mode of the energy distribution.

3.5 Expectations from the Modified Leading Logarithmic Approximation

The Modified Leading Log Approximation (MLLA) of perturbative QCD has been developed to provide a quantitative description in e^+e^- interactions of the properties of soft particles with relatively small momenta which are radiated from high energy quarks and gluons [38]. An earlier attempt, the Double Logarithmic Approximation (DLA), which attempts to describe soft particle production, overestimated gluon multiplicities in the parton cascade. To control the parton production, the MLLA takes into account non-leading Single Logarithmic (SL) effects. The MLLA predicts

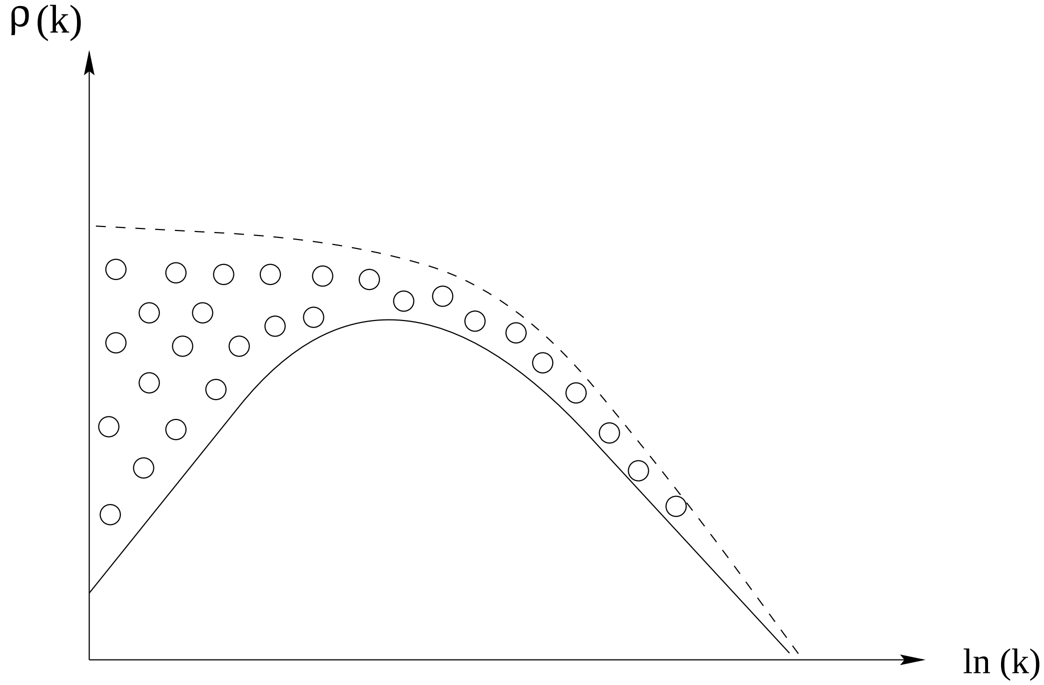

Figure 3.7: *The effect of colour coherence on the energy distribution of partons within the cascade. The dotted area corresponds to the contribution which is removed from the incoherent (dashed) case to the coherent (solid) case.*

the form of the inclusive momentum distribution for massless partons radiated from a high energy source, of energy $\sqrt{s_{ee}} \equiv E^*$. At high energies and in the relativistic limit, the analytical form is given by a limiting spectrum, $\overline{D}^{lim}(\xi, Y)$, described in reference [38]. The variables are $\xi = \ln(1/x_p)$ where the scaled momentum $x_p = 2p_{hadron}/E^*$ and the dimensionless variable $Y = \ln(E^*/\Lambda_{eff})$. The free parameter Λ_{eff} sets the scale of the mass of the final state fragmented hadrons and is not related directly to $\Lambda_{\overline{MS}}$.

The MLLA predictions are used in conjunction with the hypothesis of Local Parton-Hadron Duality (LPHD) [38, 41], in which the observed hadron distributions are related to calculated parton distributions by a constant of proportionality, which is predicted to be independent of the energy of the hard scattering process.

Thus, the hump-backed plateau is not only predicted to be experimentally observed but the MLLA results can be directly applied to the observed distributions such that

$$\frac{1}{\sigma}\frac{d\sigma}{d\xi} = \kappa^{ch}\overline{D}^{lim} \tag{3.12}$$

where the parameter κ^{ch} is the constant of proportionality used to relate the hadron spectrum to the analytical spectrum from the MLLA.

The MLLA result can be approximated by a Gaussian distribution about the peak position given by

$$\frac{1}{\sigma}\frac{d\sigma^{e^+e^-}}{d\xi} \approx N(Y)\left(\frac{c_1}{\pi Y^{3/2}}\right)^{1/2} exp\left(\frac{-c_1[\xi - \xi_{max}]^2}{Y^{3/2}}\right) \tag{3.13}$$

where $c_1 = \sqrt{36N_c/b}$ and $b = 11N_c/3 - 2N_f/3$ are constants which depend on the number of flavours, N_f and number of colours, N_c. $N(Y)$ is the average charge particle multiplicity which, within the assumption of LPHD, is proportional to the soft parton multiplicity predicted by the theory.

If Q is taken to be equivalent to $\sqrt{s_{ee}}$ and is normalised by an effective energy scale to give a variable $Y = \ln(Q/2\Lambda_{eff})$ then, assuming gluon coherence, the predicted MLLA behaviour of the peak position and width is [38]

$$\xi_{peak} = 0.5Y + c_2\sqrt{Y} + \mathcal{O}(1) \tag{3.14}$$

$$\xi_{RMS} = \sqrt{Y^{3/2}/2c_1} \tag{3.15}$$

where $c_2 = B\sqrt{b/16N_c}$, $B = (\frac{11}{3}N_c + \frac{2}{3}N_f/N_c^2)/b$ and $\mathcal{O}(1)$ contains higher order corrections.

In equation 3.14, it can be seen that apart from the higher order correction, Λ_{eff} is the only free parameter and even that is constrained to be a few hundred MeV. Once a value has been determined, the peak position and width can be predicted at any value of Q. This shall be discussed later in chapter 7.

3.6 Coherence in e^+e^- Annihilation

A number of e^+e^- experiments have studied the inclusive momentum distribution, $\ln(1/x_p)$ of charged particles in the interaction $e^+e^- \rightarrow$ hadrons and its evolution

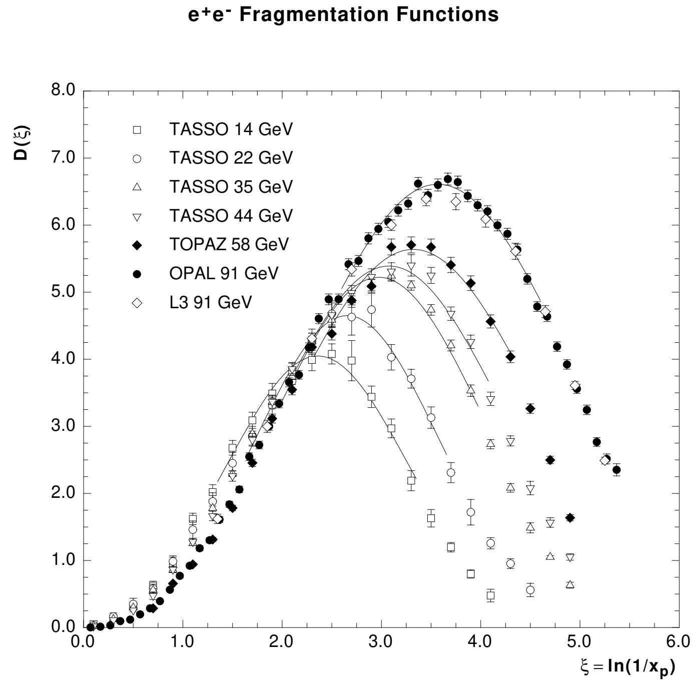

Figure 3.8: $\ln(1/x_p)$ *distributions at* $E^* = 14, 22, 35, 44$ *and 91 GeV.*

with $E^* = \sqrt{s_{ee}}$ [42, 43, 44, 45]. These results have shown that the inclusive momentum spectrum as a function of $\sqrt{s_{ee}}$ are approximately Gaussian as shown in figure 3.8. The hump-backed gaussian distribution of $\ln(1/x_p)$ does not, by itself constitute proof for gluon coherence [46].

Compared to the incoherent case, coherence effects modify the peak position and the degree of fall-off on the right hand side of the ξ distribution corresponding to the low momentum end of the spectrum. The evolution of the peak position, ξ_{max}, has been best described by combining results from e^+e^- experiments at different centre-of-mass energies e.g from TASSO (E* = 14, 22, 35 and 44 GeV) and OPAL (91 GeV). The value of Λ_{eff} and $\mathcal{O}(1)$ obtained from this are 0.21 ± 0.02 GeV and -0.32 ± 0.06 respectively [43].

These results from e^+e^- interactions are compared to the H1 measurements in chapter 7.

3.7 Coherence in Deep Inelastic Scattering

The kinematic region accessible by HERA allows tests of perturbative QCD to be made over a large kinematic range. In comparison to a given e^+e^- experiment at one fixed value of E^*, an ep experiment results in a wide range of Q thus enabling the evolution of fragmentation to be tested in a single experiment.

In DIS, to leading order QCD, the observed hadrons from the evolution of partons emanate from three possible regions. These regions are the struck quark, the proton remnant and gluon emission emanating from the colour string stretched between the quark-diquark system. The evolving partons from these regions are quite different and it is therefore advantageous to separate them for independent study. However, in ep interactions there is no exact equivalent of the e^+e^- centre of mass system. In the HERA laboratory system most of the observed transverse momentum in the hadronic final state arises from momentum conservation against the scattered lepton, thus the ep laboratory system is a poor frame to study QCD effects. The hadronic centre-of-mass (CMS) is one candidate in which the total hadronic system is at rest with energy W. In this frame the virtual photon and incident proton approach along a common z axis. If the final state is a simple two particle system (quark and proton remnant), as would be expected in the QPM, then conservation of momentum demands that there be no transverse momentum. The quark and remnant decay into opposite hemispheres with equal and opposite momenta.

The Breit frame, which can be reached from the hadronic CMS by boosting along the z axis, is another possible frame in which hadronic final states may be studied. This frame is defined such that the virtual photon, q is entirely space-like, having zero energy component and components of momentum aligned along the negative z direction such that $q = (0, 0, 0, -Q)$, maintaining the convention that the incoming proton travels in the +z direction. In the QPM the incoming quark has momentum $Q/2$, collides elastically with the virtual boson and is scattered in the opposite direction with momentum $-Q/2$. The proton remnant continues in the direction of the incident proton. Thus, in this simplistic model also, the Breit frame separates into two hemispheres into which particles are assigned according to their longitudinal momentum component in this boosted frame. Particles with $p_z < 0$

form the current region corresponding to the direction of the struck quark in the QPM, whilst particles with $p_z > 0$ form the target region however, the magnitudes of target-associated particles are much greater. The Breit frame is defined solely by the kinematics of the virtual current, it is not a zero momentum frame, and is concerned more with the quark-current rather than, as in the hadronic CMS, proton-current interactions. Thus, despite some difficulties [47], the negative z hemisphere of this frame, rather than the hadronic CMS, has been suggested [38, 41] as a better approximation to one half of the e^+e^- CMS. The Breit frame is discussed in more detail in chapter 5.

This thesis is principally concerned with a study of fragmentation arising from the evolving struck parton in the negative z hemisphere of the Breit frame as a function of the event x and Q^2.

3.8 The Colour Dipole Model

In the colour dipole model (CDM) QCD radiation of quarks and gluons is described by a chain of dipoles radiating a colour field. ARIADNE [29] provides an implementation of the colour dipole model. It is interfaced to the LEPTO Monte Carlo generator, which generates the electro-weak part of the scattering process leaving ARIADNE generate the QCD cascade process afterwards. Hadronisation is performed by JETSET which uses the LUND string model to transform coloured partons into colourless hadrons. When a gluon is emitted from a dipole [48] (e.g., from a $q\overline{q}$ pair in e^+e^- annihilation), the subsequent emission of softer gluons is given by two independent dipoles, one stretched from the quark to the gluon and the other from the gluon to the antiquark. This result is generalised in ARIADNE, so that the emission of one more gluon is given by three independent dipoles as shown in figure 3.9.

The CDM description of gluon emission is similar to that of the BFKL evolution because the gluons emitted by the dipoles do not obey strong angular ordering. Furthermore, the dipole prescription leads to a kinematical constraint for the allowed rapidity of each emitted gluon corresponding to strong angular ordering in parton showers [49].

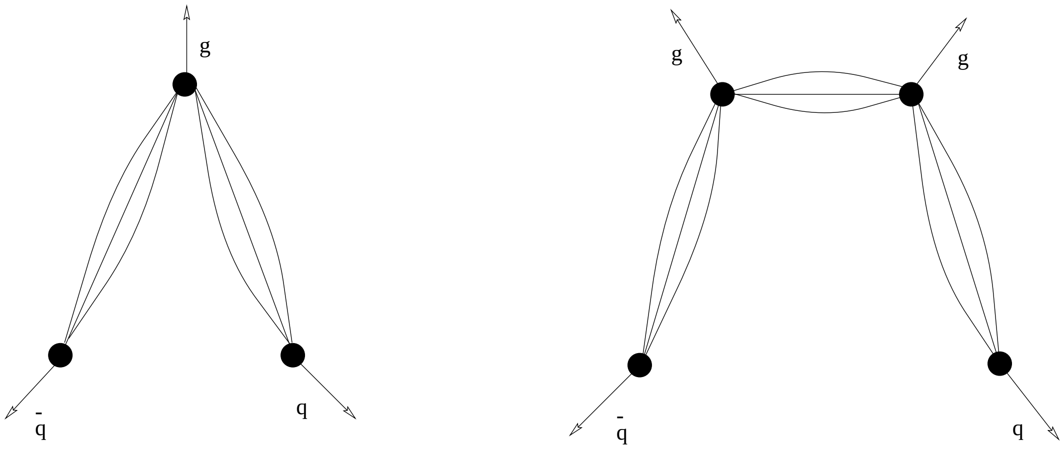

Figure 3.9: *Two stages of the dipole chain development. In the Lund model a colour field or string can be specified either in terms of gluons or in terms of the dipoles stretched between the gluons or the gluons and the quarks.*

These dipoles form links or chains, such that one gluon connects two dipoles and one dipole connects two gluons. The gluons are ordered in the dipole chain according to their colour which is in close correspondence with the Lund string model where gluons act as transverse excitations on a string like field.

3.8.1 CDM Extension to Deep Inelastic Scattering

For e^+e^-, the dipole model is essentially equivalent to the conventional parton shower scenario. The main difference lies in the ordering of the cascade i.e, the implementation of the Sudakov form factor [50]. In the dipole model the ordering is in the p_T^2 of the emissions whereas in the parton shower the ordering is in the virtuality Q^2 of the emitting parton. The implementation of the dipole model for deep inelastic scattering (DIS) is very similar to the e^+e^- case. The main difference is that the emitting quarks in the latter case can be considered basically point-like, which is not the case in DIS [51]. The quark 'kicked out' from the proton in DIS can still be treated as pointlike. However, in the colour dipole between the quark and the proton remnant the latter must be treated as an extended coloured object. One drawback of the CDM scheme is its inability to describe BGF events. As the CDM only considers the radiation from the dipole between the struck quark and the proton remnant, it will not allow for a situation in which the incoming gluon splits into a quark-antiquark pair. This problem can be overcome[1] by generating BGF processes using first order matrix elements and adding subsequent emissions using dipole radiation.

3.9 Hadronisation

Hadronisation describes the non-perturbative process of transforming final partons into a jet of hadrons. The Monte Carlo generators used in this thesis to compare with data use the Lund String hadronisation model. However, other schemes such as independent and cluster fragmentation (as implemented in HERWIG) have been used for comparison. These models are briefly described below.

3.9.1 Local Parton-Hadron Duality

The simplest assumption for hadronisation is local parton-hadron duality (LPHD) [41]. In this model it is assumed that the general features of the partonic final state, such as energy flows and multiplicities, can be related to the spectra of hadrons by introducing normalisation constants. These constants have to be determined by experiment. The existence of LPHD is not yet verified experimentally, although studies at LEP show a very good agreement with predictions based on this assumption [43, 44, 52, 53].

3.9.2 Independent Fragmentation

The original model which attempted to describe the way partons fragment into hadrons was proposed by Feynman and Field in 1978 [54]. This model is based on the scaling hypothesis and on meson production i.e., $q\overline{q}$ pairs emerge out of the vacuum till the energy of the original parton is used up. As the name implies, each primary parton is treated independently and fragmentation proceeds via a simple recursive scheme as shown in figure 3.10. An initial primary quark q_1 combines with an antiquark $\overline{q_2}$ from a pair $q_2\overline{q_2}$ to form a meson $M_1(q_1\overline{q_2}))$. The remaining quark

---

[1] The ARIADNE program is interfaced with the LEPTO [33] Monte Carlo generator, which generates the electro-weak part of the scattering leaving ARIADNE generate the QCD cascade process afterwards. Henceforth, this implementation shall be referred to as the MEAR Monte Carlo.

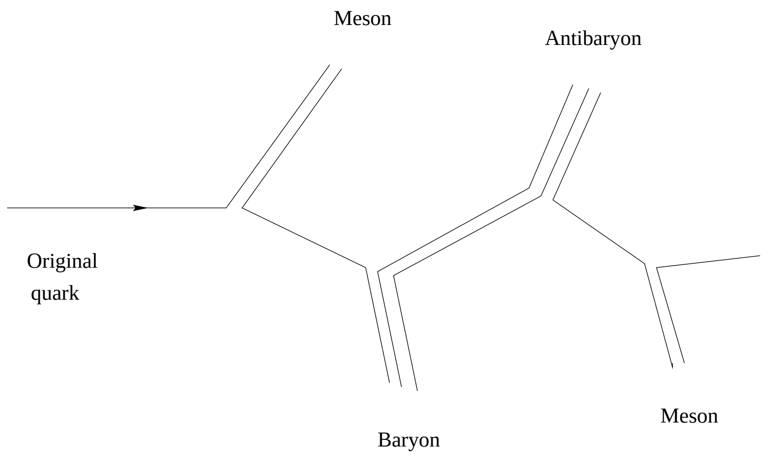

Figure 3.10: *Pictorial representation of independent fragmentation.*

q_2 combines with an antiquark $\overline{q_3}$ from a pair $q_3\overline{q_3}$ to form a meson $M_2(q_2\overline{q_3})$) and so on down the chain. The meson M_1 is sometimes called the first in 'rank', M_2 the second in 'rank' etc. This is not necessarily their ordering in momentum but would be expected to be close to it. This model has been modified to include baryon production [55], in which a quark q_i occasionally combines with two quarks q_jq_k from a 'diquark-antidiquark' pair $q_jq_k\overline{q_jq_k}$ to form a baryon $q_iq_jq_k$. The remaining 'antidiquark' $\overline{q_jq_k}$, then combines with an antiquark $\overline{q_l}$ from a pair $q_l\overline{q_l}$ to form an antibaryon $\overline{q_lq_jq_k}$.

One basic deficiency of this algorithm is that it cannot conserve both energy and longitudinal momentum simultaneously. Several different schemes for energy and momentum conservation have been devised, see for example [56, 57].

3.9.3 String Fragmentation

Another way of looking at the process of fragmentation is the Lund String Model [34] which is the *de facto* standard for Monte Carlo generators which implement JETSET [35].

String models are based on the idea that as primary partons move apart, a colour flux tube or string stretches between them. Figures 3.11 (a) and (b) contrast the electric field lines produced by the electromagnetic interaction between two electric charges with the chromodynamic field lines produced by the strong interaction

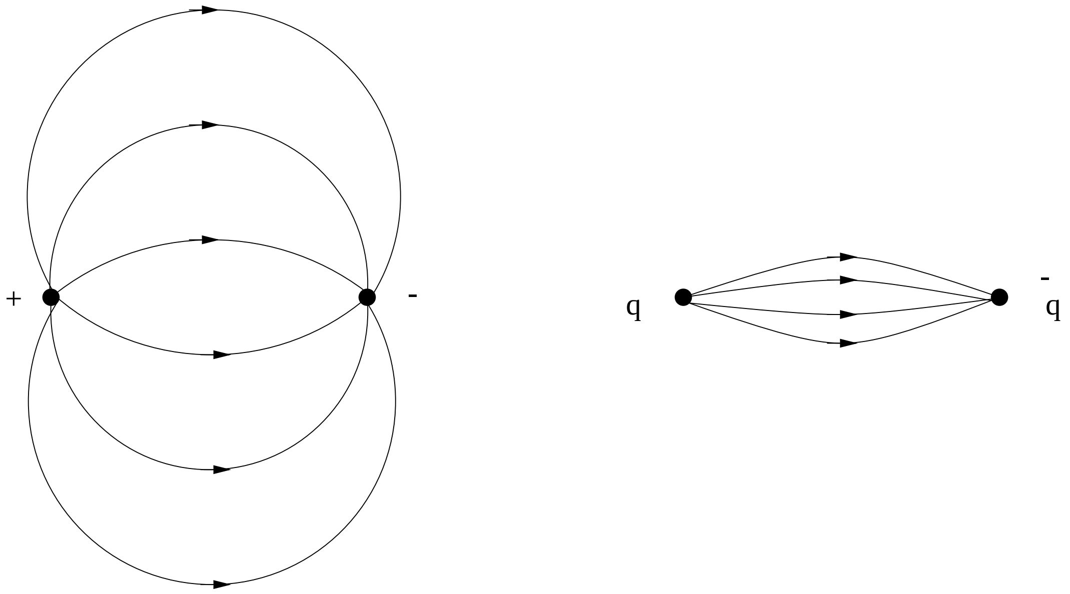

(a) (b)

Figure 3.11: *Contrast between the electric field lines produced by the electromagnetic interactions between electric charges with the strong field lines produced by the strong interaction between two colour charges.*

between two colour charges.

In the second case, because of the coupling between gluons, the flux lines are pulled together and form a colour flux tube or 'string' between the partons. If the string has a constant energy density per unit length (as is suggested by the spectra of e.g, ϕ excitations) then the potential energy in the string rises linearly as the colour charges separate, the energy being supplied from the kinetic energy of the partons. In other words, if the partons are rapidly separating from each other the string is stretched. This requires energy since the colour force rises with increasing separation (confinement). Once the potential energy in the string is sufficient to be able to create a quark-antiquark pair from the vacuum, the string will break into two separate strings as shown in figure 3.12. In this way the original string will subsequently break up into smaller string pieces, corresponding to conventional on-shell hadrons. In order to generate the quark-antiquark pairs $q_i\overline{q_i}$ which lead to string breakups, the Lund model evokes the idea of quantum tunneling.

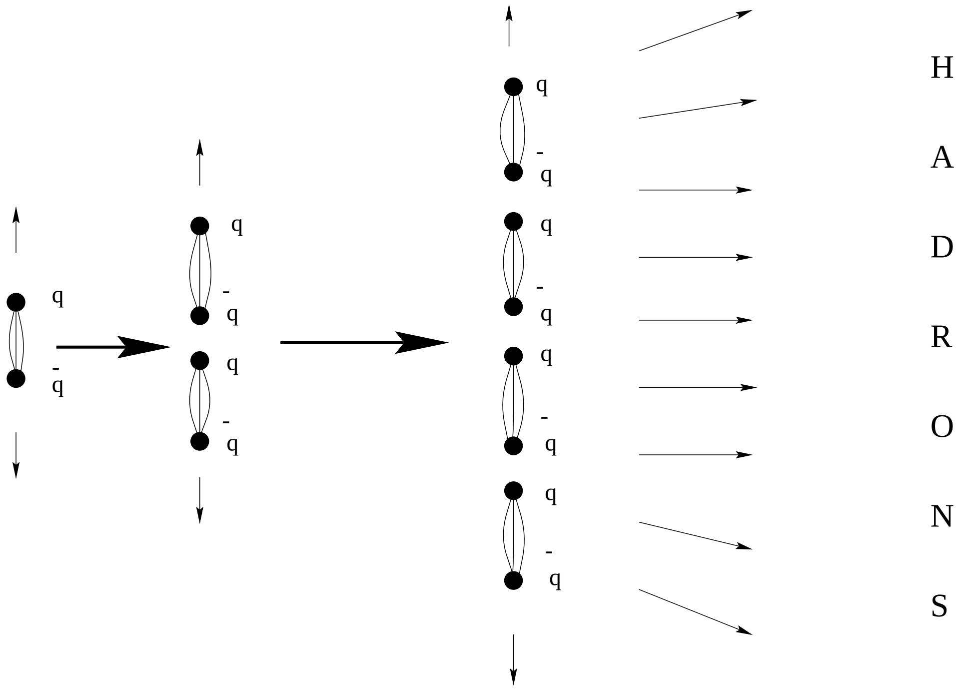

Figure 3.12: *String fragmentation model. A string between a $q\overline{q}$ pair is stretched and breaks into smaller pieces. Finally the low energy strings give rise to mesons and baryons.*

3.9.4 Cluster Fragmentation

The formation and decay of colourless clusters is implemented by HERWIG [58]. After the perturbative stage of parton generation, all final gluons are split non-perturbatively into essentially light (u or d) quark and anti-quark pairs. They are combined into colourless clusters [59] which decay into hadrons.

Chapter 4

Deep Inelastic Scattering Event Selection

4.1 Introduction

During the 1993 running period an integrated luminosity of $\sim$ 500 nb^{-1} of useful data was recorded by H1. However, only a small proportion of the events gathered consist of neutral current (NC) deep inelastic scattering (DIS) events which are of interest to this analysis. The main bulk of recorded data is still due to beam-gas, cosmic ray and photoproduction events. It is the object of the following selection cuts to reduce the level of background in order to obtain a relatively clean sample of neutral current DIS events.

4.2 L5 Event Classification at DST Level

The object of the data summary tape (DST) is to provide a sample of NC DIS event candidates, which have satisfied the L4 and L5 event classification module ECLASS [60]. The ECLASS software algorithm assigns a physics class (or more than one class) to each event which is based on reconstructed event properties. The NC DIS event candidates which have been selected for the DST data have been classified as either NC low Q^2 or NC high Q^2 events. The ECLASS definition in turn uses the following sub-classification:

- Low Q^2 events have an electron candidate cluster in the BEMC and are assigned the class NCLQSQ.

- High Q^2 events have an electron candidate cluster in the barrel or forward region of the LAr and are assigned the class NCHQSQ.

4.2.1 Class NCLQSQ

The most energetic cluster in the backward electromagnetic calorimeter (BEMC) must have an energy greater than 8 GeV and be associated with a hit in the backward proportional chamber (BPC). The cluster must be suitably well contained within the BEMC, avoiding regions of poor acceptance such as the inner most part of BEMC.

4.2.2 Class NCHQSQ

The high Q^2 classification is based on events with an electron candidate cluster in the LAr. A candidate is defined as a reconstructed cluster with an electromagnetic energy fraction (EAEM) $> 50\%$. In addition, the event is required to balance in p_t, by requiring the missing transverse momenta, p_t^{miss}, ≤ 40 GeV. An event is then classified as high Q^2 if there exists at least one good CJC or forward track and the electron candidate is found in either one of the following regions:

1. $10° \leq \theta_e \leq 45°$ and $E_t^e \geq 8$ GeV
2. $45° \leq \theta_e \leq 160°$ and $E_t^e \geq 5$ GeV

It can be seen that the events are classified according to the expected event topology. The loose electromagnetic energy fraction and p_t^{miss} cut mean that the event classification does not reject many genuine high Q^2 events due to reconstruction and detector effects.

4.3 Event Selection

The source data for this analysis come from the late period of 1993 when magnetic field in the H1 detector was reestablished. Selections to further limit the data only to periods when there were extremely stable tracking conditions and when there was no coincident problem with electronic noise in the H1 calorimetry give a total integrated luminosity[1] for this subset of $\approx$ 150 nb^{-1}.

4.3.1 Electron Selection

From the DST, a sample of neutral current DIS events are selected by demanding a well-reconstructed scattered electron of energy greater than 14 GeV, that is fully contained in either the BEMC or the LAr calorimeter. Photoproduction events in which the final state electron scatters undetected down the beam pipe may have isolated low energy deposits in the calorimeter which give rise to false electron candidates with low energies. Such events will contaminate this sample but are removed by imposing the 14 GeV cut. The selection $12 < \mathrm{Q}^2 < 80$ GeV^2 defines the BEMC (low Q^2) sample, whereas the requirement for the scattered electron to have a polar angle in the range $10° < \theta_e < 150°$ (resulting in the constraint Q^2 $>$ 100 GeV^2) and thus avoiding the intermediate region between BEMC and LAr where energy measurements are problematic, defines the LAr or high Q^2 sample.

For the low Q^2 sample, the most energetic BEMC cluster must be associated with a space point in the BPC within 5 cm of the weighted cluster centre. The BPC hit must lie less than 60 cm from the beam line, corresponding to an electron angle above 157° with respect to the nominal interaction point. In addition the electron angle θ_e has to be smaller than 172.5°, ensuring full containment of the electron shower in BEMC.

From extensive Monte Carlo studies, the efficiency of the DST criteria was estimated to be 98 ± 2% [61] for electron energies greater than 8 GeV, given that the electron scattered into either the BEMC or the LAr calorimeter.

4.3.2 Event Vertex Position

The z-position of the event vertex provided from the tracking system is used to remove events which do not originate near the nominal interaction point. This selection criteria was motivated by the observation of a large number of upstream proton background events, not vetoed by ToF, which satisfied the DST selection.

---

[1] Note that in this thesis there is no attempt to derive absolute cross-sections for any process so this number is not determined exactly.

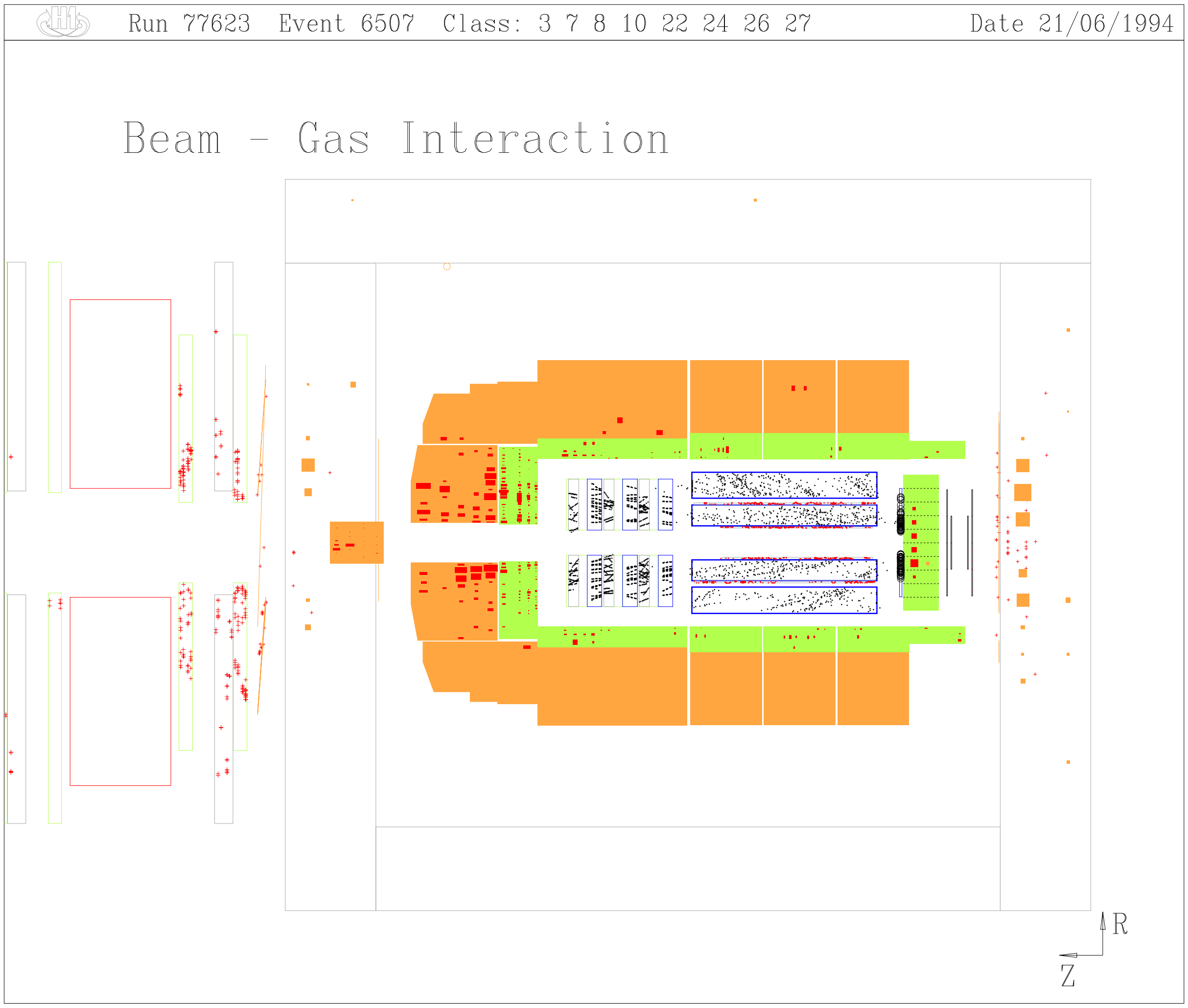

Figure 4.1: *Beam induced background event in the H1 detector.*

Such events, largely caused by interactions below or beyond ToF itself, as shown in Figure 4.1, have BEMC and LAr energy deposits but no CJC tracks, which when reconstructed, point toward the nominal interaction point.

In this analysis, the z-vertex requirement ensures that the kinematic variables are well determined from properties of the scattered electron. The data were required to have a reconstructed event vertex which satisfied $-35 < z_{vertex} < 25$ cm. The cut is asymmetric in z to account for the shift in the vertex position from the nominal interaction point and to reduce the contribution from the proton satellite peak.

Data Sample	Non diffractive events
$12 < Q^2 < 80$ GeV^2	4566
$Q^2 > 100$ GeV^2	373

Table 4.1: *Size of data samples for this analysis. See text for definition of selections.*

4.4 Forward Energy Selection

The distribution of the calorimetric energy, E_F, in the forward region of the LAr calorimeter ($4.4° < \theta_{LAr\ cluster} < 15°$) is shown in Figure 4.2. Two distinct classes of event are observed. Most events have considerable energy in the forward region while 6% of the events have only very little forward energy. The events are believed to stem from diffractive - like processes [62] which are not included in the standard QCD models used in this analysis, and so are removed from the sample. Such an event is shown in Figure 4.3. To remove these diffractive-like events we demand that for each event E_F has to be larger than 0.5 GeV. The resultant event numbers are presented in Table 4.1.

4.5 Hadronic Activity

To have sufficient hadronic activity in the central detector and to avoid the problematic low y region where QED radiative corrections are large [5], the square of the invariant mass of the hadronic system, W^2, is required to be larger than 3000 GeV^2.

4.6 Track Selection

As discussed in chapter 1, good efficiency for triggering and reconstruction over the full solid angle is accomplished by means of a central and forward tracking system. There are in principle two types of tracks. Those which are vertex constrained and hence originate from the primary vertex are referred to as primary tracks, and secondary tracks associated to secondary vertices from, for example, K_S^0 decays or from a background of secondary interactions. The track selection discussed in this

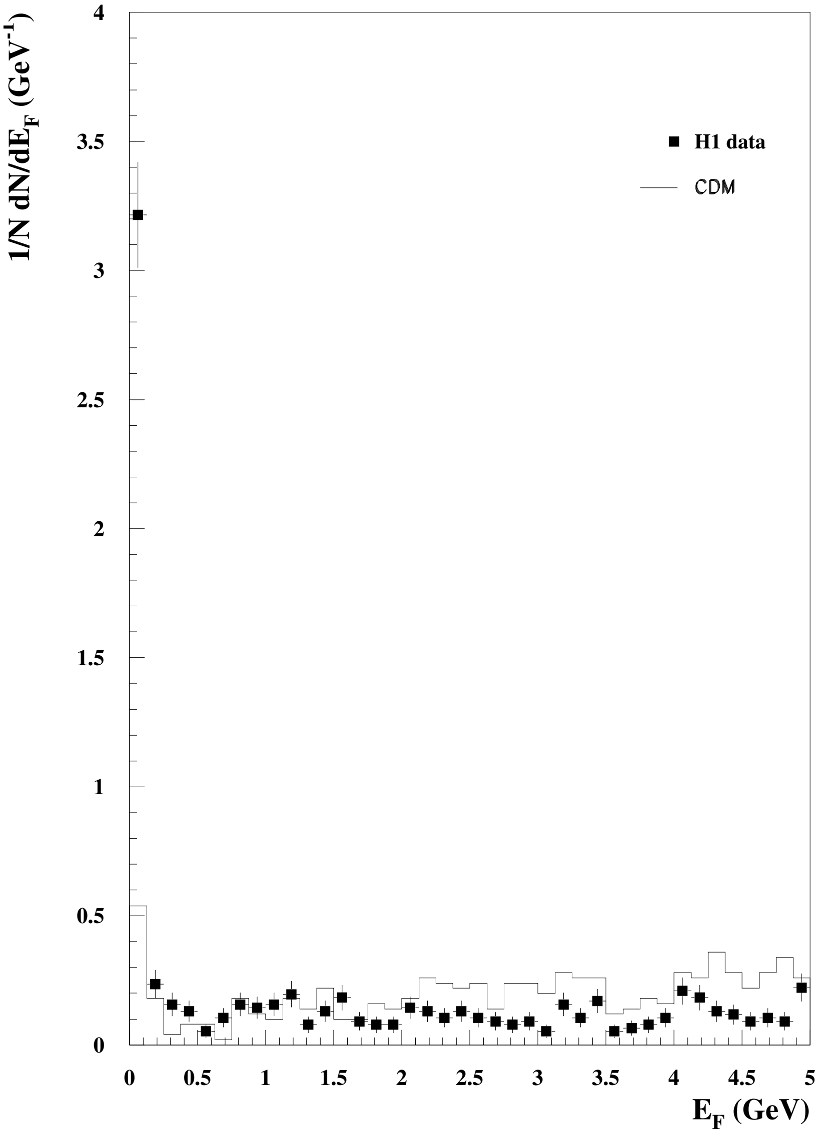

Figure 4.2: *The energy in the forward region, $4.4 < \theta < 15^\circ$. The data are compared with the CDM Monte Carlo. Both distributions are normalised to the number of events N.*

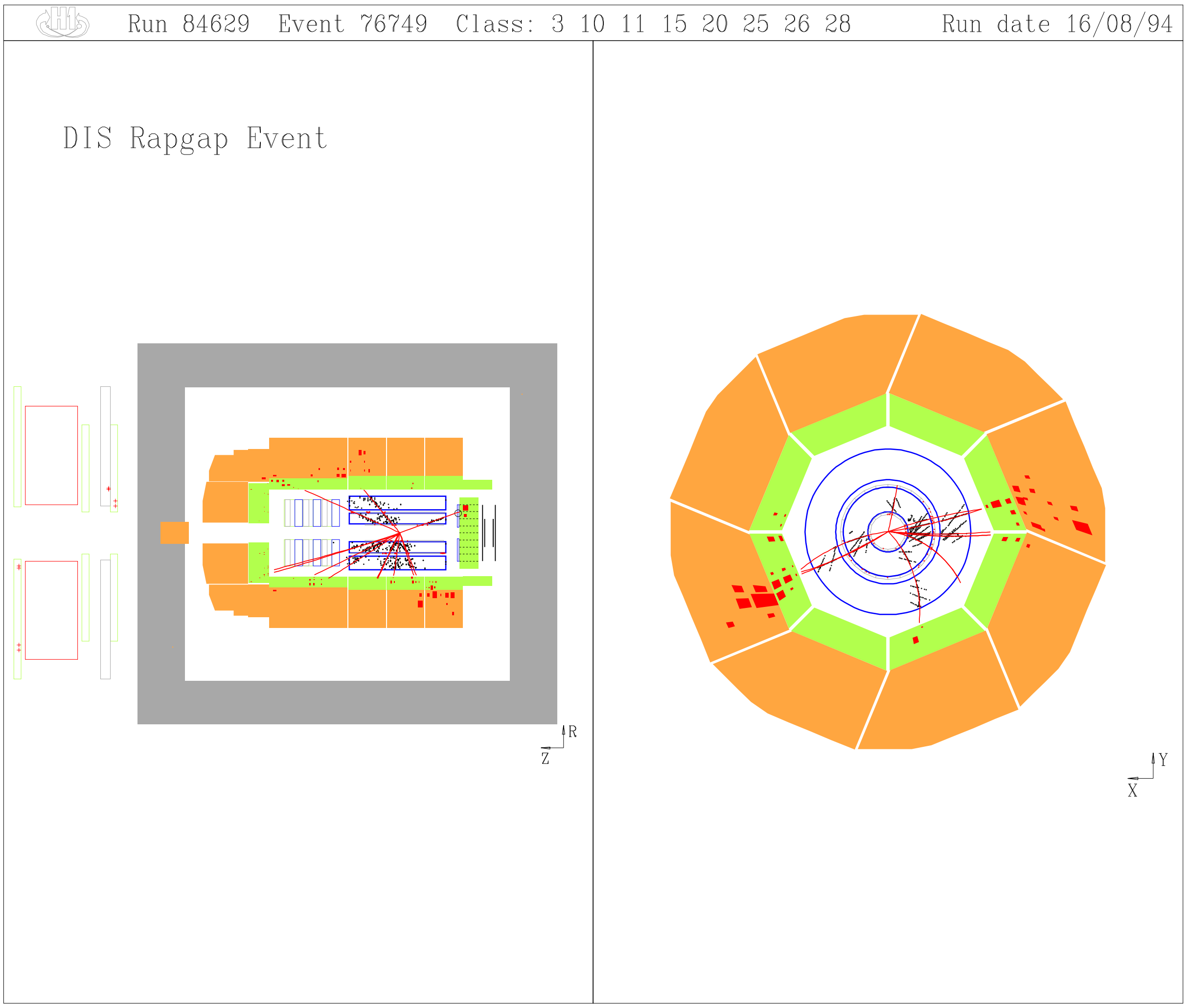

Figure 4.3: *A diffractive-like event.*

section is designed to select primary tracks representing stable charged particles originating from the interaction point which are of interest in multiplicity studies. Tracks which traverse the CJC only are subject to central track selection while those that pass through the forward tracker are subject to forward track criteria. To provide a smooth acceptance over the whole angular range, tracks which traverse both tracking systems are subject to the 'combined track' selection criteria.

The track cuts discussed below fail to exclude roughly half of the 4% of tracks arising from K_s^0 decays [63]. In order to obtain a more pure sample of charged pion candidates, the Monte Carlo corrections discussed in chapter 6 account for the remaining contribution of such decays.

4.6.1 Central Track Selection

1. The track has to have a polar angle between 10° and 150°.
2. The transverse momentum of the track has to lie in the range from 0.15 and 10.0 GeV. The lower cut in transverse momentum ensures that tracks can pass through both chambers of the CJC, and avoids reconstruction problems, where the track finding efficiency deteriorates, associated with very low momentum tracks curling back on themselves.
3. The momentum of a track is determined by the curvature of the track. If the track is very energetic it will have a small curvature associated with it and the momentum error, $\delta p/p$, will be large. Central tracks are required to have $\delta p/p \leq 1.0$.
4. The track has to be constrained to the vertex with a distance of closest approach in the $x-y$ plane to the z axis (DCA) less than 3.0 cm. The $z-$coordinate of that point is Z_0 and the track is further required to point in the local region of the vertex position, Z_{vertex}, such that $|Z_0 - Z_{vertex}| \leq$ 20.0 cm.
5. The $\chi^2_{vertexfit}$ is used to determine whether the track originates from the primary vertex. Tracks with a large χ^2 have a low probability of originating from the vertex and are therefore discarded. In this analysis, CJC tracks are required to have $\chi^2_{vertex\ fit} \leq 20.0$.

4.6.2 Forward Track Selection

1. The track must lie in the polar angle between 10° and 60°. Geometrically, the lower cut is used to avoid problems associated with edge effects of the subdetector.
2. $\chi^2_{vertex\ fit} \leq 20.0$
3. The momentum of the track, p, is required to be greater that 0.5 GeV to suppress low momentum scattering in non-sensitive materials in or between different subdetectors such as the end wall of the CJC. The momentum error of the track is required to be $\delta p/p \leq 1.0$.
4. To suppress tracks that have been associated with wrong hits in the forward tracker, the ratio of χ^2 for the track fit to the number of degrees of freedom (NDF), $\chi^2_{track\ fit}/NDF \leq 25.0$.
5. To determine if the track extrapolates reasonably close to the vertex, the distance in the $x - y$ plane between the track and vertex, R_0, must be less than 10.0 cm.

4.6.3 Combined Tracks

Combined tracks which traverse through the central and forward trackers essentially follow the forward track selection criteria.

1. $\chi^2_{vertex\ fit} \leq 20.0$
2. $\chi^2_{track\ fit}/NDF \leq 25.0$
3. $p \geq 0.5$ GeV
4. $dp/p \leq 1.0$
5. $R_0 \leq 10.0$ cm.

In 1992, using a visual scan, the ratio of track reconstruction efficiency[2] for the data, compared to the track reconstruction efficiency for Monte Carlo was found to be 92 ± 3% [25]. This discrepancy was due to readout problems which were badly

---

[2] The track reconstruction efficiency is defined as the number of reconstructed tracks over the number of tracks visually found.

modelled in the Monte Carlo. In 1993 however, the readout problems are better simulated in the standard Monte Carlo and this simulation is further improved by modelling dead regions of the central jet chamber (see section 4.6.4). The reconstruction efficiency obtained from a visual scan as described above for two prong events [64] using the standard Monte Carlo but which did not include a simulation of the dead regions in the CJC was found to be $\sim 95\%$ and therefore, there is good reason to believe that Monte Carlo and data are in good agreement.

Thus, the reader should bear in mind that there could be, although unlikely, a further systematic error of about 8% to the multiplicity measurements which are discussed in chapter 7. This error has not been included.

4.6.4 Quality Plots

In figure 4.4 some basic track distributions in the laboratory frame are shown between real tracks, and simulated tracks using the MEAR Monte Carlo after full detector simulation and reconstruction. Both samples have identical event and track selections. It is clear from the figure that the ϕ distributions have obvious holes which are caused by chamber inefficiencies affecting about 15% of the azimuthal range. This was caused by a large number of broken wires in CJC1. The question as to whether a perfect simulation of the dead regions is necessary is discussed in chapter 6.3.

4.7 Reconstruction of Event Kinematics

In order to calculate the correct Lorentz transformation necessary for the boost to the Breit frame, the kinematic variables x and Q^2 should be determined as precisely as possible. The variables are given in terms of the energies of the incoming electron E_e, the scattered electron E_e', the incoming proton E_P, the hadronic recoil jet E_h and the corresponding polar angles θ_e and θ_h, both of which are measured relative to the proton direction $\theta = 0^\circ$. Beam momenta and directions are known extremely precisely from accelerator data thus giving an over-constrained system.

Several methods have been proposed and studied [65]:

1. Electron-only method: $Q^2[E_e',\theta_e]$ and $y[E_e',\theta_e]$ are determined from the

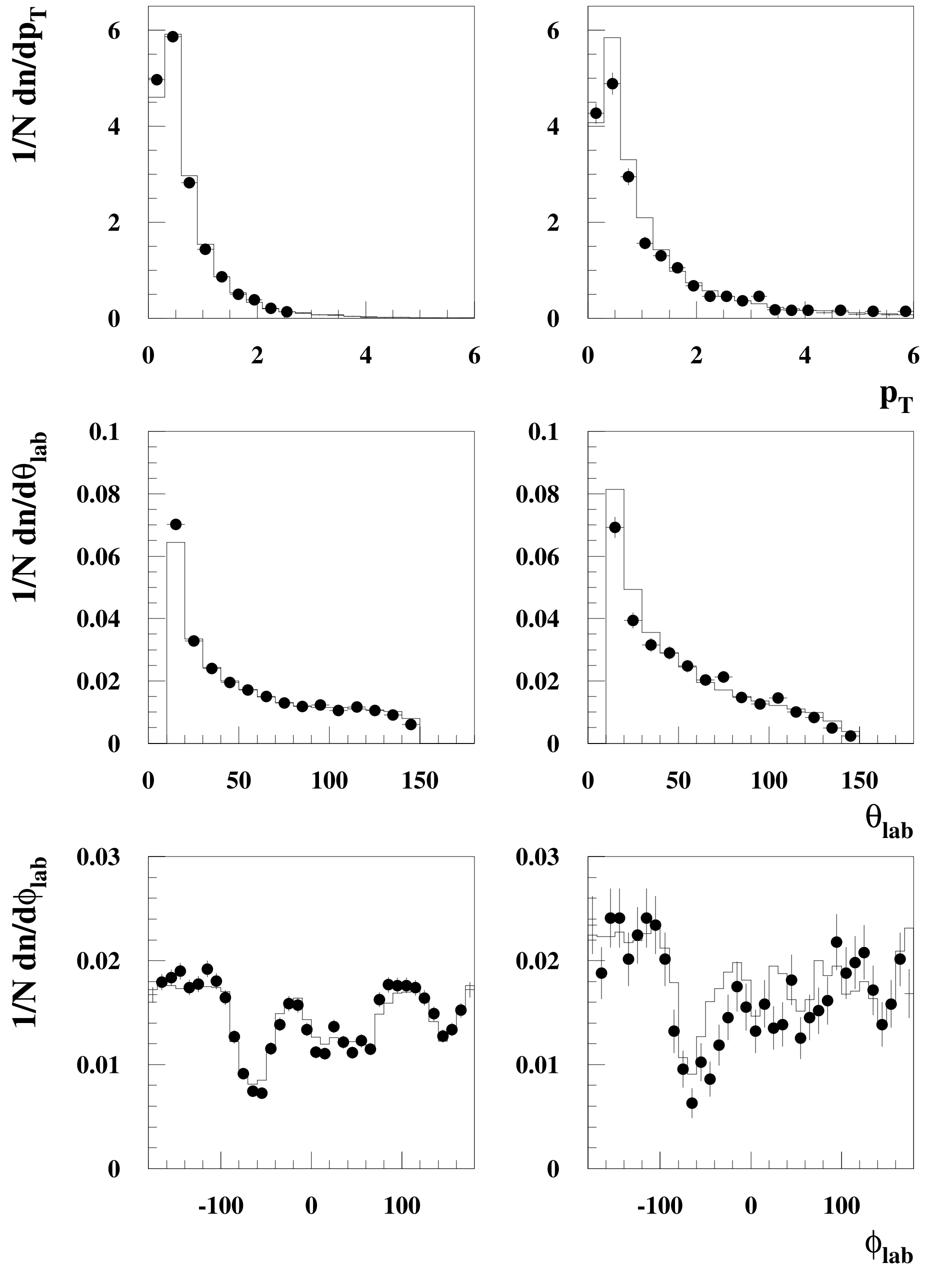

Figure 4.4: *A comparison between real and simulated tracks for transverse momentum p_T, polar angle θ, and the azimuthal angle ϕ in the laboratory frame of reference for low (left-side) and high (right-side) Q^2 data sets. The points show the real data and the histograms the reconstructed Monte Carlo samples. All distributions are normalised to the number of events N.*

scattered electron's energy and polar angle.

2. Hadron-only method (Jacquet-Blondel): $Q^2[E_h,\theta_h]$ and $y[E_h,\theta_h]$ are calculated from all the DIS final state hadrons.
3. Double-angle method: $Q^2[\theta_e,\theta_h]$ and $y[\theta_e,\theta_h]$ are determined from the polar angles of the scattered electron and the current jet (struck quark).
4. Mixed method: $Q^2[E_e',\theta_e]$ is determined from the scattered electron energy and $y[\theta_e,\theta_h]$ from the Jacquet-Blondel method.

When comparing different methods, the following points are used to judge their performance:

- good resolution over the kinematical plane,
- insensitivity to QED radiative corrections,
- insensitivity to the calorimeter calibration,
- insensitivity to the limited hadronic measurement due to the beam pipe holes.

It is beyond the scope of this thesis to present detailed studies into the advantages and disadvantages of all the proposed methods, as this would diverge from the main essence of this chapter. More details and results using these methods can be found elsewhere [66, 67].

4.7.1 Electron Only Method (EL)

Within this thesis, the kinematics for neutral current DIS events are determined using information from the scattered electron only. The advantage of this method is that 'event by event' the boost to the Breit frame can be calculated independently of the hadronic system. There is thus explicitly no possibility of bias. From the electron variables

$$Q_e^2 = 2E_eE_e'(1+\cos\theta_e) \tag{4.1}$$

$$y_e = 1-\frac{E_e'}{2E_e}(1-\cos\theta_e) \tag{4.2}$$

$$x_e = \frac{E_eE_e'(1+\cos\theta_e)}{E_P(2E_e-E_e'(1-\cos\theta_e))} \tag{4.3}$$

where x_e follows from the relation $Q_e^2 = s x_e y_e$.

The influence of finite angle and energy can be shown [68] by taking partial derivatives of the above expressions giving the uncertainties Δ for x_e and Q_e^2 to give:

$$\frac{\Delta Q_e^2}{Q_e^2} = \frac{\Delta E_e'}{E_e'} \oplus \tan(\frac{\theta_e}{2}).\Delta\theta_e \tag{4.4}$$

$$\frac{\Delta x_e}{x_e} = \frac{1}{y_e}\frac{\Delta E_e'}{E_e'} \oplus (x_e\frac{E_P}{E_e} - 1)\tan(\frac{\theta_e}{2}).\Delta\theta_e \tag{4.5}$$

It is clear from equation 4.5 that the x_e measurement cannot extend far below $y_e \sim 0.05$ because the resolutions diverge [69] as $y_e \rightarrow 0$. The resolutions are made worse by the fact that any mis-measurement of the electron energy is amplified by the y_e^{-1} factor. The Q_e^2 values are well-measured except in the kinematic region where the electron scattering angles are large, typically $\theta_e \geq 175°$. In these cases the Q_e^2 resolution is dominated by the $\tan(\theta_e/2)$ term. However, the requirement that the electron cluster candidate in the BEMC be linked to a BPC hit implies that $\theta_e \leq 172.5°$. Thus for the low Q^2 electrons in this sample, the $\tan(\theta_e/2)$ term is relatively small and the Q_e^2 resolution will be dominated by the electron energy resolution.

The kinematic variables determined from this method have a very high precision, but suffer significantly from QED radiative effects in the low and high y region. The event cuts applied to the data are designed to avoid these regions so that the effects of initial state QED radiation are expected to be small.

4.7.2 Jacqet-Blondel Method (JB)

To enable the event kinematics to be reconstructed in charged current (CC) DIS events, where the scattered neutrino goes undetected, a method was devised to determine the event kinematics from the DIS hadronic final state. The Jacquet-Blondel [70] method is based on energy-momentum conservation between the 'invisible' neutrino (or electron in NC DIS) and the hadronic system i.e, the vector sum of all outgoing hadrons. The kinematic relations are then derived from the definitions of Q^2 and y at the hadronic vertex as:

$$y_{JB} = \frac{\sum_h (E_h - p_{z,h})}{2E_e} \tag{4.6}$$

$$Q^2_{JB} = \frac{(\sum_h p_{x,h})^2 + (\sum_h p_{y,h})^2}{1 - y_{JB}} \tag{4.7}$$

$$x_{JB} = \frac{Q^2_{JB}}{s y_{JB}} \tag{4.8}$$

where, the above sum is performed over all outgoing hadrons and E_e is the incoming electron energy.

The direction of the "massless" hadronic energy flow (struck quark in the quark parton model) is given as

$$\cos\gamma_h = \frac{Q^2_{JB}(1 - y_{JB}) - 4E_e^2 y^2_{JB}}{Q^2_{JB}(1 - y_{JB}) + 4E_e^2 y^2_{JB}} \tag{4.9}$$

which is experimentally determined by summing over calorimeter energy cells, except those associated with the scattered electron, using

$$\cos\gamma_h = \frac{(\sum_h p_{x,h})^2 + (\sum_h p_{y,h})^2 - (\sum_h (E_h - p_{z,h}))^2}{(\sum_h p_{x,h})^2 + (\sum_h p_{y,h})^2 + (\sum_h (E_h - p_{z,h}))^2} \tag{4.10}$$

The cancellation of the energy terms in the above expression makes $\cos\gamma_h$ insensitive to any imperfections in the calorimeter energy scale. However, particles escaping through the backward beam hole deteriorate the y and hence the Q^2 and x measurement.

4.7.3 Double-Angle Method (DA)

The double-angle method uses the angle of the electron and the inclusive angle of the hadronic final state. Assuming an homogeneous energy measurement over the full solid angle, the DA method is independent of the absolute energy calibration.

4.7.4 Mixed Method (MI)

At HERA a fourth method has been used which combines y measured from the hadrons and Q^2 from the electron, which is the so-called mixed method [71]:

$$x_{MI} = \frac{Q_e^2}{s y_{JB}} \tag{4.11}$$

The mixed method allows to extend the F_2 measurement done with the DA method or with the electron method towards lower y.

4.8 Q^2 and x Resolution

To measure the resolution on x and Q^2 due to the different reconstruction methods, reconstructed Monte Carlo events are subject to the same series of kinematic cuts applied to the real data to obtain a corresponding sample of DIS events[3]. The resolution was measured in terms of Δx and ΔQ^2 given by

$$\frac{\Delta x}{x_T} = \frac{x_R - x_T}{x_T} \tag{4.12}$$

$$\frac{\Delta Q^2}{Q_T^2} = \frac{Q_R^2 - Q_T^2}{Q_T^2} \tag{4.13}$$

where x_T and Q_T^2 are the generated (true) values and, x_R and Q_R^2 are the reconstructed values which are determined from each of the different methods discussed in the previous section. Orthogonal bins in x and Q^2 are chosen to remove any bias which might occur due to the event selection. The bins which are chosen to examine the affect of kinematic reconstruction using different methods are defined in the first and second column of table 4.2. In general the percentage error in Q^2 can be $\leq 10\%$ whereas in x is always poorer and between $20 \rightarrow 30\%$. It is clear from table 4.2 that the electron only method provides a slightly better reconstructed x compared to that from the double angle and mixed methods in the low Q^2 (< 100 GeV^2). However, in the high x ($> 10^{-2}$) and high Q^2 (> 100 Gev^2) region, the resolution on x deteriorates for the electron only method and that of the double and mixed

---

[3] Refer to chapter 5 for additional selections applied to the data.

Q^2 Interval	x_{Bj}	$\Delta x/x_T$ %				$\Delta Q^2/Q_T^2$ %			
(GeV^2)		EL	JB	DA	MI	EL	JB	DA	MI
$12 \rightarrow 15$	$5.0\text{x}10^{-4} \rightarrow 1.0\text{x}10^{-3}$	27.2	30.1	33.7	31.0	6.6	33.0	6.3	6.4
	$1.0\text{x}10^{-3} \rightarrow 2.0\text{x}10^{-3}$	29.9	30.4	32.2	31.5	5.1	31.1	4.9	5.1
	$2.0\text{x}10^{-3} \rightarrow 4.0\text{x}10^{-3}$	30.5	35.0	28.1	27.8	3.9	28.9	4.4	4.7
$15 \rightarrow 20$	$5.0\text{x}10^{-4} \rightarrow 1.0\text{x}10^{-3}$	23.6	33.3	31.4	31.0	6.0	35.2	7.1	5.9
	$1.0\text{x}10^{-3} \rightarrow 2.0\text{x}10^{-3}$	27.2	32.6	30.3	30.9	5.4	33.4	5.3	5.3
	$2.0\text{x}10^{-3} \rightarrow 4.0\text{x}10^{-3}$	31.4	33.7	31.0	31.0	4.8	36.4	4.5	4.8
$20 \rightarrow 40$	$1.0\text{x}10^{-3} \rightarrow 2.0\text{x}10^{-3}$	19.9	36.0	31.3	31.2	5.0	40.0	6.7	4.9
	$2.0\text{x}10^{-3} \rightarrow 4.0\text{x}10^{-3}$	24.2	34.5	29.7	30.9	4.7	38.5	5.7	4.7
	$4.0\text{x}10^{-3} \rightarrow 7.0\text{x}10^{-3}$	26.2	34.6	28.9	31.0	4.7	38.2	5.4	4.7
$40 \rightarrow 60$	$2.0\text{x}10^{-3} \rightarrow 4.0\text{x}10^{-3}$	25.3	34.2	28.3	30.7	4.6	37.7	5.4	4.6
	$4.0\text{x}10^{-3} \rightarrow 7.0\text{x}10^{-3}$	25.5	33.8	27.9	30.6	4.6	37.3	5.3	4.6
	$7.0\text{x}10^{-3} \rightarrow 1.3\text{x}10^{-2}$	25.8	33.8	27.7	30.4	4.5	37.0	5.2	4.5
$60 \rightarrow 80$	$2.0\text{x}10^{-3} \rightarrow 4.0\text{x}10^{-3}$	25.4	33.7	25.8	30.2	4.5	36.9	5.3	4.5
	$4.0\text{x}10^{-3} \rightarrow 7.0\text{x}10^{-3}$	25.3	33.5	27.3	30.2	4.5	36.7	5.2	4.5
	$7.0\text{x}10^{-3} \rightarrow 1.3\text{x}10^{-2}$	25.4	33.4	27.1	30.0	4.4	36.4	5.2	4.5
$200 \rightarrow 300$	$6.0\text{x}10^{-3} \rightarrow 1.0\text{x}10^{-2}$	12.3	30.3	16.7	25.6	4.7	35.8	5.4	4.8
	$1.0\text{x}10^{-2} \rightarrow 2.0\text{x}10^{-2}$	19.9	25.4	13.5	22.8	4.8	33.7	3.1	4.9
	$2.0\text{x}10^{-2} \rightarrow 6.0\text{x}10^{-2}$	29.2	19.6	12.9	17.5	4.1	26.0	2.3	4.3
$300 \rightarrow 500$	$1.0\text{x}10^{-2} \rightarrow 2.0\text{x}10^{-2}$	11.3	28.8	11.9	23.3	3.4	37.5	3.9	3.4
	$2.0\text{x}10^{-2} \rightarrow 6.0\text{x}10^{-2}$	23.9	18.6	10.7	16.6	4.2	26.2	2.5	4.3
$500 \rightarrow 800$	$2.0\text{x}10^{-2} \rightarrow 6.0\text{x}10^{-2}$	17.2	19.4	9.0	11.7	4.2	27.5	2.9	4.2
	$6.0\text{x}10^{-2} \rightarrow 1.5\text{x}10^{-1}$	24.4	14.9	10.0	13.1	3.2	19.2	2.6	3.2
$800 \rightarrow 2000$	$6.0\text{x}10^{-2} \rightarrow 1.5\text{x}10^{-1}$	22.8	14.6	8.7	12.9	4.0	19.8	2.9	4.0

Table 4.2: Percentage error in x and Q^2, $\Delta x/x_T$ and $\Delta Q^2/Q_T^2$ respectively, for the x and Q^2 bins indicated.

Q^2 GeV^2	**Events**	$\Delta x/x_T$ %	$\Delta Q^2/Q^2_T$ %
12 → 15	248	30.7	5.5
15 → 20	394	29.8	5.6
20 → 40	788	26.2	4.7
40 → 60	337	23.3	3.9
60 → 80	178	22.7	3.7
100 → 175	21	11.1	4.1
175 → 250	64	20.4	4.1
250 → 450	76	18.8	3.7
450 → 1000	60	17.8	3.9
1000 → 8000	14	14.3	3.3

Table 4.3: (x,Q^2) bins adopted within this thesis. The choice for these bins were motivated by the small number of statistics available and the desire to examine fragmentation over a large range of Q values.

methods become superior. The Jacquet-Blondel method in this region is compatible with the electron method. With the exception of the Jacquet-Blondel method, all other methods discussed here provide very good Q^2 determination.

4.9 Analysis Bins

Due to the $1/Q^4$ dependence of the NC DIS cross-section, the bulk of the data resides at low Q^2. The choice of analysis bins for this thesis were motivated by the small statistics available and are given in table 4.3. The data have also been plotted on the (x, Q^2) plane as shown in figure 4.5.

Figure 4.6 and figure 4.7 show the $\Delta x/x_T$ and $\Delta Q^2/Q^2_T$ distributions for the low Q^2 sample. Each plot indicates the RMS of the distribution. The resolution in x is observed to improve as Q^2 increases from 31% in the lowest bin to 24% in the highest bin. The Q^2 resolution is very good and is less than 6%.

4.10 Conclusions

It can be clearly seen that all methods except the Jacquet-Blondel method provide a reasonably well reconstructed x and Q^2 measurement. The x measurement is the most sensitive of the two variables examined and its resolution deteriorates in the

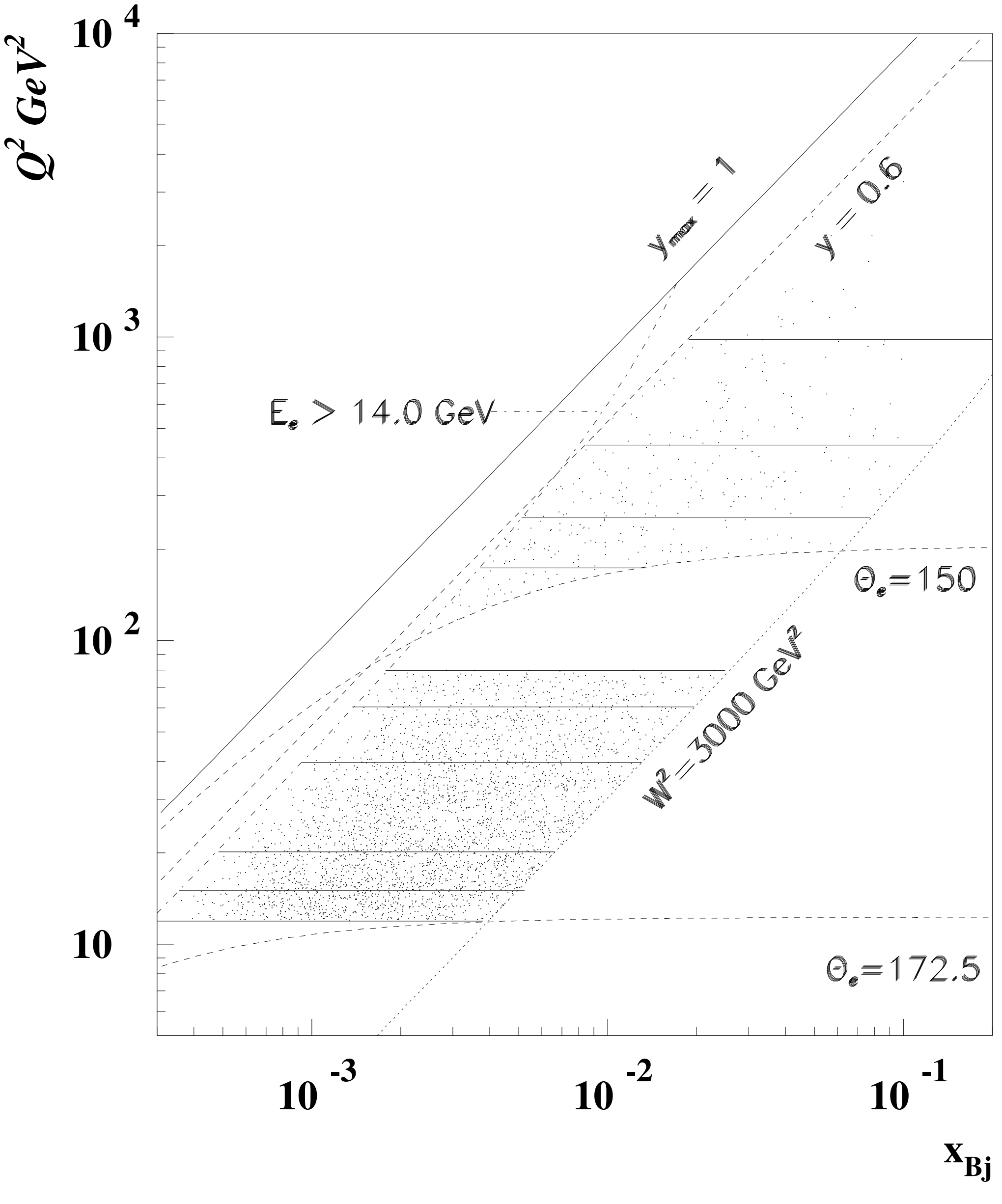

Figure 4.5: *The low and high Q^2 data sets are plotted on the (x, Q^2) plane. Shown also are some of the event cuts which are applied to the data in order to obtain a pure sample of deep inelastic events.*

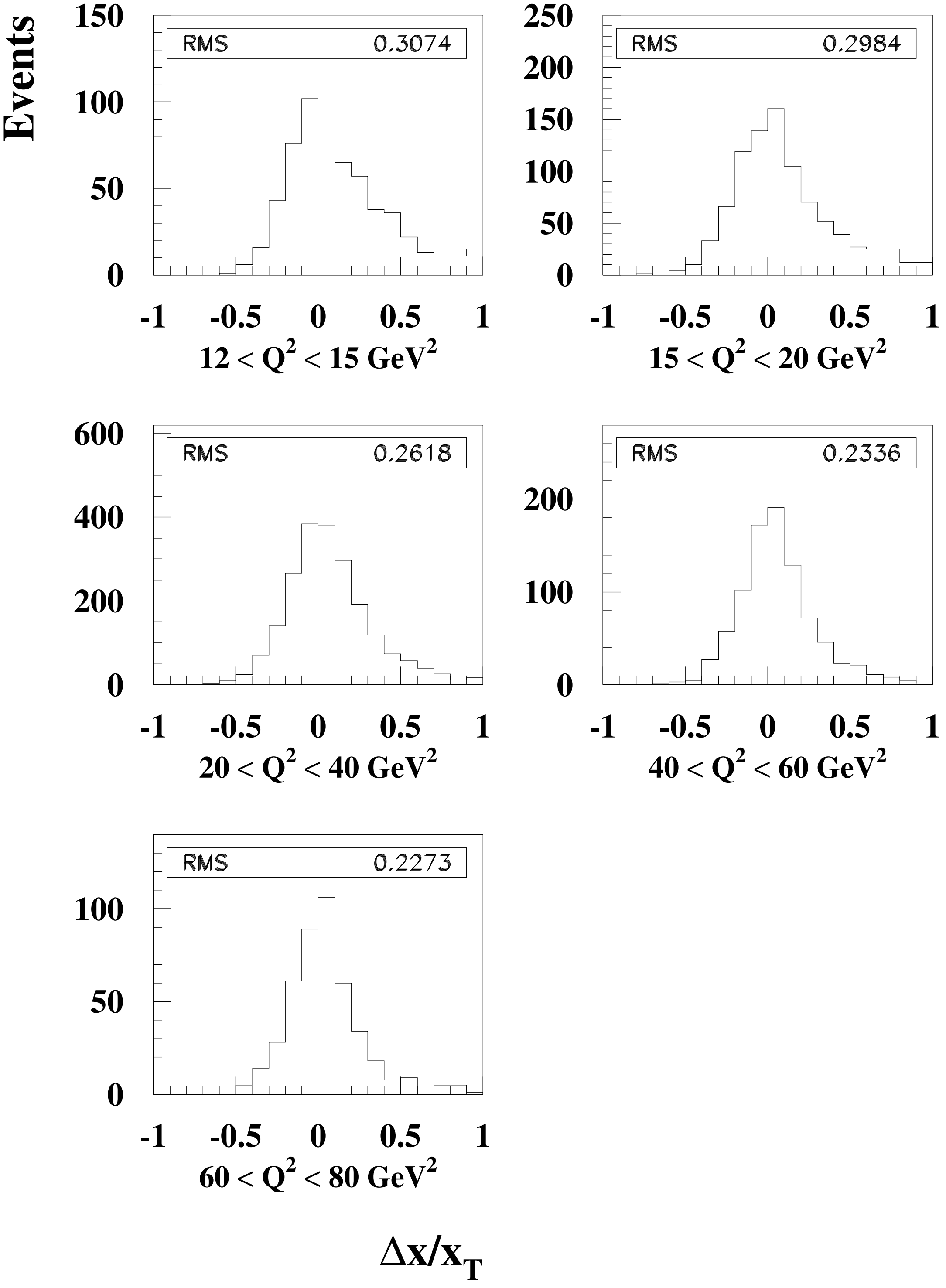

Figure 4.6: *The distributions* $\Delta x/x_T$ *for events in the low* Q^2 *Monte Carlo sample. The event kinematics have been determined using the electron only method.*

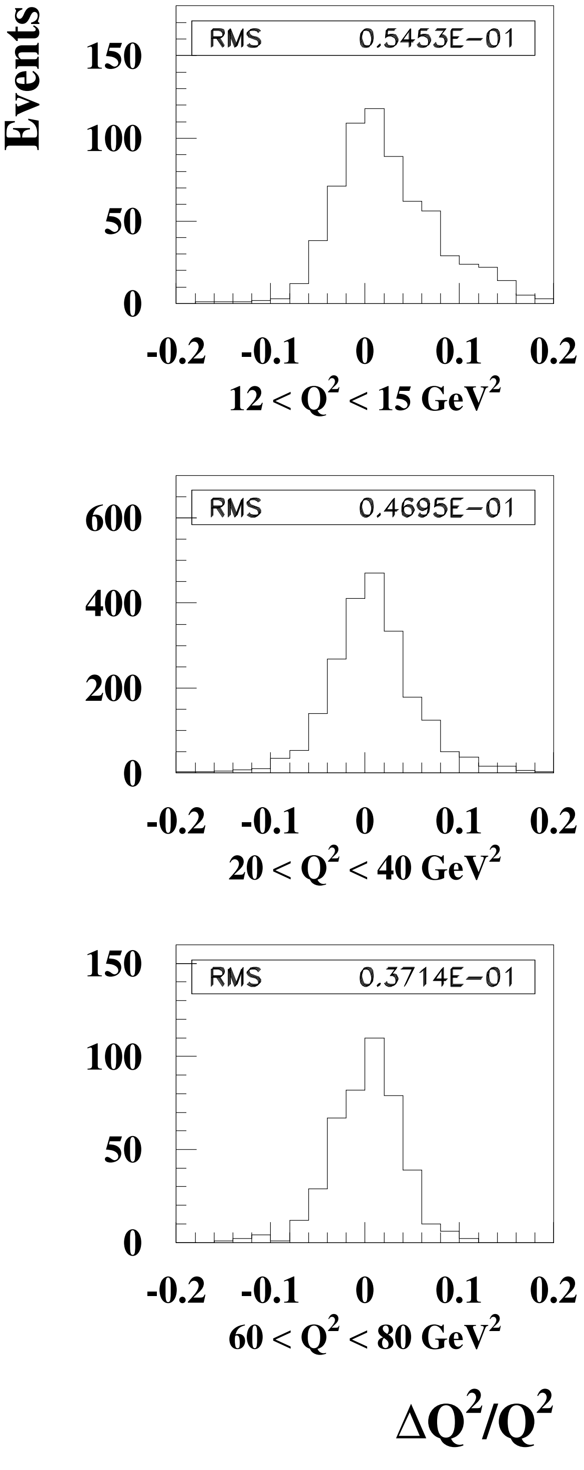

Figure 4.7: *The distributions $\Delta Q^2/Q_T^2$ for events in the low Q^2 Monte Carlo sample. The event kinematics have been determined using the electron only method.*

low Q^2 high x region. However, because the bulk of the data resides at low Q^2 due to the $1/Q^4$ dependence of the DIS cross-section, the electron method is favoured over the double angle method, say, as this provides the best measurement over the limited (x,Q^2) domain covered by events which satisfy the DIS event selection described in the earlier part of this chapter. The bins chosen for the x and Q^2 resolutions in section 4.8 are not the same as those chosen for the final analysis (section 4.9). These bins are to demonstrate the regions in the (x,Q^2) plane where migrations are expected to be large due to the poor reconstruction of the Breit frame z axis. The analysis bins that are chosen for the final analysis are motivated by the small statistics available.

Chapter 5

Inertial Frames of Reference

5.1 Introduction

The Lorentz transformation to the Breit frame via the hadronic centre-of-mass frame is discussed. It is shown that these reference frames are related by a simple longitudinal boost. Event topologies in the Breit frame are studied and compared to those predicted by the Quark Parton Model (QPM). Such a comparison allows for the removal of events that suffer significantly from QCD radiation not experienced in e^+e^- interactions as well as reconstruction effects.

5.2 The Breit Frame

It is instructive to perform the Lorentz transformation from the HERA laboratory frame to the Breit frame in two stages. In the first stage, the HERA laboratory frame is boosted to the hadronic centre-of-mass (CMS) by a boost followed by rotation [72]:

$$p \xrightarrow{\Lambda} \tilde{p} \xrightarrow{R} p^* \tag{5.1}$$

The Lorentz boost is given by the matrix[1]

$$\Lambda = \begin{pmatrix} \gamma & -\gamma\beta_x & -\gamma\beta_y & -\gamma\beta_z \\ -\gamma\beta_x & 1+(\gamma-1)\beta_x^2/\beta^2 & (\gamma-1)\beta_x\beta_y/\beta^2 & (\gamma-1)\beta_x\beta_z/\beta^2 \\ -\gamma\beta_y & (\gamma-1)\beta_x\beta_y/\beta^2 & 1+(\gamma-1)\beta_y^2/\beta^2 & (\gamma-1)\beta_y\beta_z/\beta^2 \\ -\gamma\beta_z & (\gamma-1)\beta_x\beta_z/\beta^2 & (\gamma-1)\beta_y\beta_z/\beta^2 & 1+(\gamma-1)\beta_z^2/\beta^2 \end{pmatrix} \tag{5.3}$$

---

[1] Equivalent with Eqn. 5.3 is the following equation, giving the Lorentz boost [73] of an arbitrary four-vector $p = (E, \vec{p})$ into the primed frame with boost velocity $(\vec{\beta})$ as:

$$E' = \gamma(E - \vec{\beta}.\vec{p}), \qquad p'_{\|} = \gamma(p_{\|} - \beta E), \qquad \vec{p}_{\perp} = \vec{p}_{\perp} \tag{5.2}$$

where $p_{\|} = \vec{\beta}.\vec{p}/\beta$, and $\vec{p}'_{\perp} = \vec{p} - \vec{p}p_{\|}/\beta$

where p' is the four momentum of the hadronic system given by $p' = p + q$ in terms of the four momentum components of the proton and virtual photon as measured in the laboratory, $\vec{\beta} = \vec{p'}/E'$, and $\gamma = (1-\beta^2)^{-1/2} = E'/\sqrt{p'^2}$ is the usual Lorentz dilation factor.

The rotation, which by convention aligns the negative-z axis along the direction of the virtual photon is given by

$$R = \begin{pmatrix} 1 & O \\ O^T & \tilde{R} \end{pmatrix} \tag{5.4}$$

where O is the row matrix $(0,0,0)$, O^T is its transpose and $\tilde{R} = R_y(\theta)R_z(\phi)$ with

$$R_y(\theta) = \begin{pmatrix} \cos\theta & 0 & -\sin\theta \\ 0 & 1 & 0 \\ \sin\theta & 0 & \cos\theta \end{pmatrix} \qquad R_z(\phi) = \begin{pmatrix} \cos\phi & \sin\phi & 0 \\ -\sin\phi & \cos\phi & 0 \\ 0 & 0 & 1 \end{pmatrix} \tag{5.5}$$

where θ and ϕ are the polar and azimuthal angles of the photon after the boost (i.e. in the tilde frame).

Within this thesis the Breit frame, as with the hadronic CMS, has a z axis which is aligned along the direction of the incoming proton. Spectator remnants which suffer no interaction continue in this direction in either of these frames. Likewise, in both frames the current is directed in the negative-z direction. Clearly, therefore, the transformation from one of these frames to the other is just a longitudinal boost[2].

The Breit frame is defined as the frame in which the energy and the transverse momentum of the virtual photon are zero. Thus, taking account of Lorentz invariance, we have in the Breit frame the 4-momentum of the virtual photon in the form

$$q_B = (0, 0, 0, -\sqrt{-q^2}) \tag{5.6}$$

For an arbitrary 4-momentum $p^* = (E^*, p_x^*, p_y^*, p_z^*)$ in the hadronic rest frame

$$E_B = \gamma_B(E^* - \beta_B p_z^*)$$

$$p_{Bx} = p_x^*$$

---

[2] In principle there should be another azimuthal rotation which, by convention, constrains the electron scattering plane to lie in the $x - z$ plane.

$$p_{By} = p_y^*$$

$$p_{Bz} = \gamma_B(\beta_B E^* - p_z^*) \tag{5.7}$$

where all quantities in the Breit frame are denoted by a subscript B, $\gamma_B = (1 - \beta_B^2)^{-1/2}$ and β_B is the velocity of the Breit frame with respect to the hadronic CMS and is given as

$$\beta_B = q^{0*}/q_z^* \tag{5.8}$$

by demanding that the energy of the virtual photon be zero.

The Breit frame is defined in this analysis such that the positive-z direction is that of the incoming parton and the negative direction that of the incoming photon. In this frame the virtual photon is entirely space-like, having a momentum $p_z = -Q$. Within the Quark Parton Model (QPM), the incident quark has momentum $p_z = +Q/2$ before, and $p_z = -Q/2$ after absorbing the photon. A diagramatic representation of such an event in the Breit frame is shown in figure 5.1.

The velocity of the Breit frame as viewed in the hadronic CMS can be easily derived. Firstly, the four momentum components of the virtual photon in the hadronic CMS (q^*) and Breit frame (q_B) are given as

$$q^* = \left[\left(\frac{W}{2}\left(\frac{1-2x}{1-x}\right)\right), 0, 0, \left(-\frac{W}{2}\left(\frac{1}{1-x}\right)\right)\right] \tag{5.9}$$

$$q_B = [0, 0, 0, -Q] \tag{5.10}$$

using the conservation of energy and momentum and given that the total hadronic energy is W.

Note that the invariance of the photon is preserved in all inertial reference frames i.e $q^2 = q^{*2} = q_B^2 = -Q^2$. Applying equation 5.2 to derive the energy of the photon in the Breit frame, the velocity of the Breit frame with respect to the hadronic CMS is found to be $\beta_B = -(1 - 2x)$ i.e. as viewed in the hadronic CMS, the Breit frame travels with a velocity of $1 - 2x$ along the negative z axis. Another way to derive this relation is to use the definition of β_B given in equation 5.8 and substitute the components of the photon given in equation 5.9. Thus for $x = 0.5$ the two systems coincide.

5.3 Rapidity Shift to the Breit Frame

To first order only, it has been shown experimentally that e^+e^- average charged multiplicities rise approximately as $\ln(E^*)$ [42, 43, 44, 45] where E^* is the centre-of-mass energy. Furthermore, it will be shown in this thesis (chapter 7) that the average charged multiplicity in the current region of the Breit frame is approximately half the average charged hadronic multiplicity of an e^+e^- interaction at an energy $E^* = Q$ [74]. Additionally, recent work at H1 [75] has shown that the average charged multiplicity in the current region of the hadronic centre-of-mass system is approximately half the charged multiplicity of an e^+e^- interaction at an energy $E^* = W$.

The rapidity distribution for particles of mass m at a centre of mass energy W expected as a result of limited p_t interactions has a total width of $\Delta Y = 2\ln(W/m)$ [73]. According to Feynman [54], this distribution is expected to have a flat plateau [36] as a natural result of the relativistic contraction of the target in the beam direction, leading to a flat distribution in the equivalent momentum variables. Neglecting the mass of the proton, the width can be re-expressed by substitution of the expression $W^2 = Q^2(1/x - 1)$ as:

$$2\ln(W/m) = 2\ln(Q/m) + \ln\left((1-x)/x\right) \tag{5.11}$$

A somewhat simplified rapidity distribution made up of these partitions is shown in figure 5.2. In this picture, the area to the left of the $Y = 0$ gives the average charged multiplicity in one hemisphere of the hadronic CMS. The simplified version depicted here indicates the same multiplicity[3] in both hemispheres.

Given such a flat plateau, the ratio of the multiplicity in the rapidity interval $\ln(W/m)$ to that in a rapidity interval $\ln(Q/m)$ is simply $\ln(W/m)/\ln(Q/m)$, which is what would be expected as a ratio of the multiplicities of e^+e^- events at two different energies, at least given a simple logarithmic dependence [76]. It follows in this approximation that if the rapidity shift, δY from $Y = 0$ in the hadronic CMS to the Breit frame is of the form

$$(\ln(W/m) - \ln(Q/m)) = (\ln W - \ln Q) \tag{5.12}$$

---

[3] In a more realistic picture, the height of the plateau in the target hemisphere is expected to be greater.

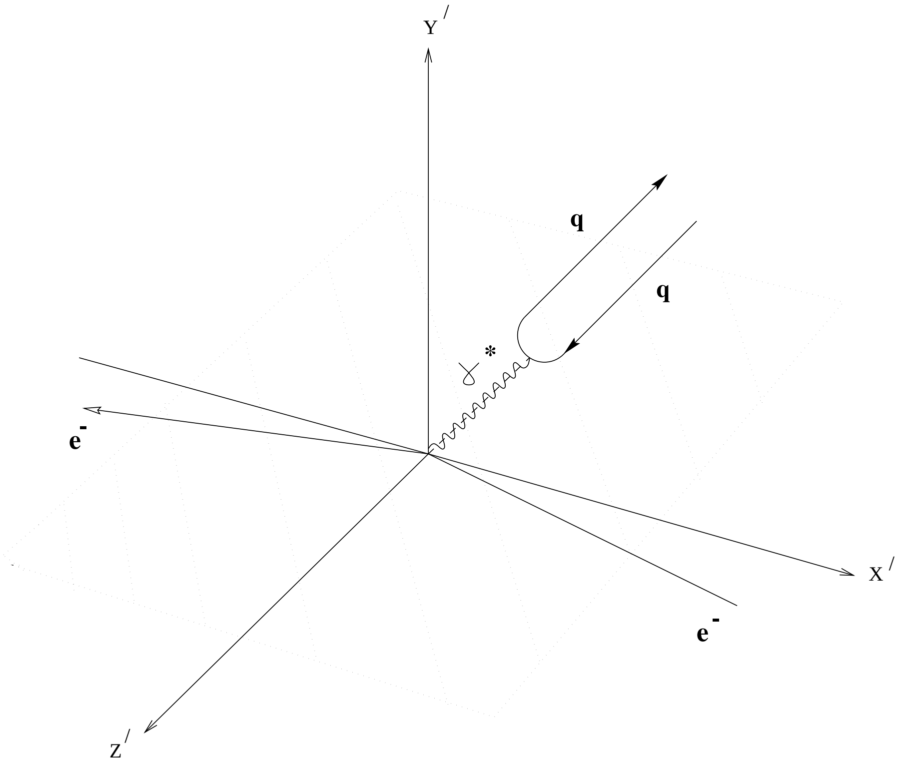

Figure 5.1: *A diagramatic representation of an event in the Breit frame.*

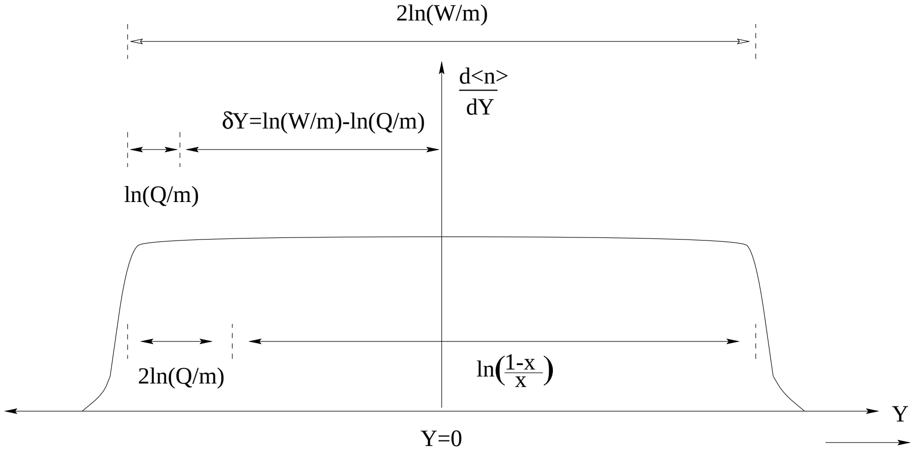

Figure 5.2: *A simplified version of the rapidity distribution (plateau) as seen in the hadronic CMS system.*

then we have proved simultaneous first order agreement of Breit frame current hemisphere multiplicities with e^+e^- data at $E^* = Q$ and hadronic CMS current hemisphere multiplicities with e^+e^- data at $E^* = W$. As stated earlier, the hadronic CMS and the Breit frame are collinear inertial reference frames linked by a simple Lorentz boost in the z-direction. Thus, the frames are expected to have the same multiplicity distribution shifted by a constant quantity in rapidity space given by [36];

$$\delta Y = \frac{1}{2}\ln\left(\frac{E^* + p_z^*}{E^* - p_z^*}\right) - \frac{1}{2}\ln\left(\frac{E_B + p_{Bz}}{E_B - p_{Bz}}\right) \tag{5.13}$$

where E_B and p_{Bz} are the Breit frame transformed energy and momenta from the hadronic CMS variables E^* and p_z^*. Choosing $p_z^* = 0$ and substituting $p_{Bz} = \gamma(0 + \beta_B E^*)$ and $E_B = \gamma(E^* + \beta_B 0)$, δY may be written as [36]:

$$\delta Y = -\frac{1}{2}\ln\frac{(1+\beta_B)}{(1-\beta_B)} \tag{5.14}$$

The expression for δY above may be further simplified using $\beta_B = 1 - 2x$ and $W^2 = Q^2(1/x - 1)$ to give,

$$\delta Y = -\frac{1}{2}\ln\frac{W^2}{Q^2} \tag{5.15}$$

and may be interpreted as a shift in the negative direction of $(\ln W - \ln Q)$ as expected in equation 5.12 assuming a flat rapidity plateau and a simple logarithmic energy dependence of multiplicities.

Since the H1 data has a natural, wide, spread of Q and W, it is difficult to show a true rapidity plateau representative of a fixed energy. Nevertheless this is done for the separately summed low (high) Q^2 data sets in figure 5.3 as an average charged particle multiplicity as a function of *pseudo*-rapidity in the Breit frame. Absolute, generated, values from the MEAR Monte Carlo are also shown.

The data are acceptance corrected[4] but the correction function is smooth and small for all values of $\eta \leq 2$. Thereafter, it increases significantly and the correction

---

[4] Acceptance corrections to the data are discussed in chapter 6.

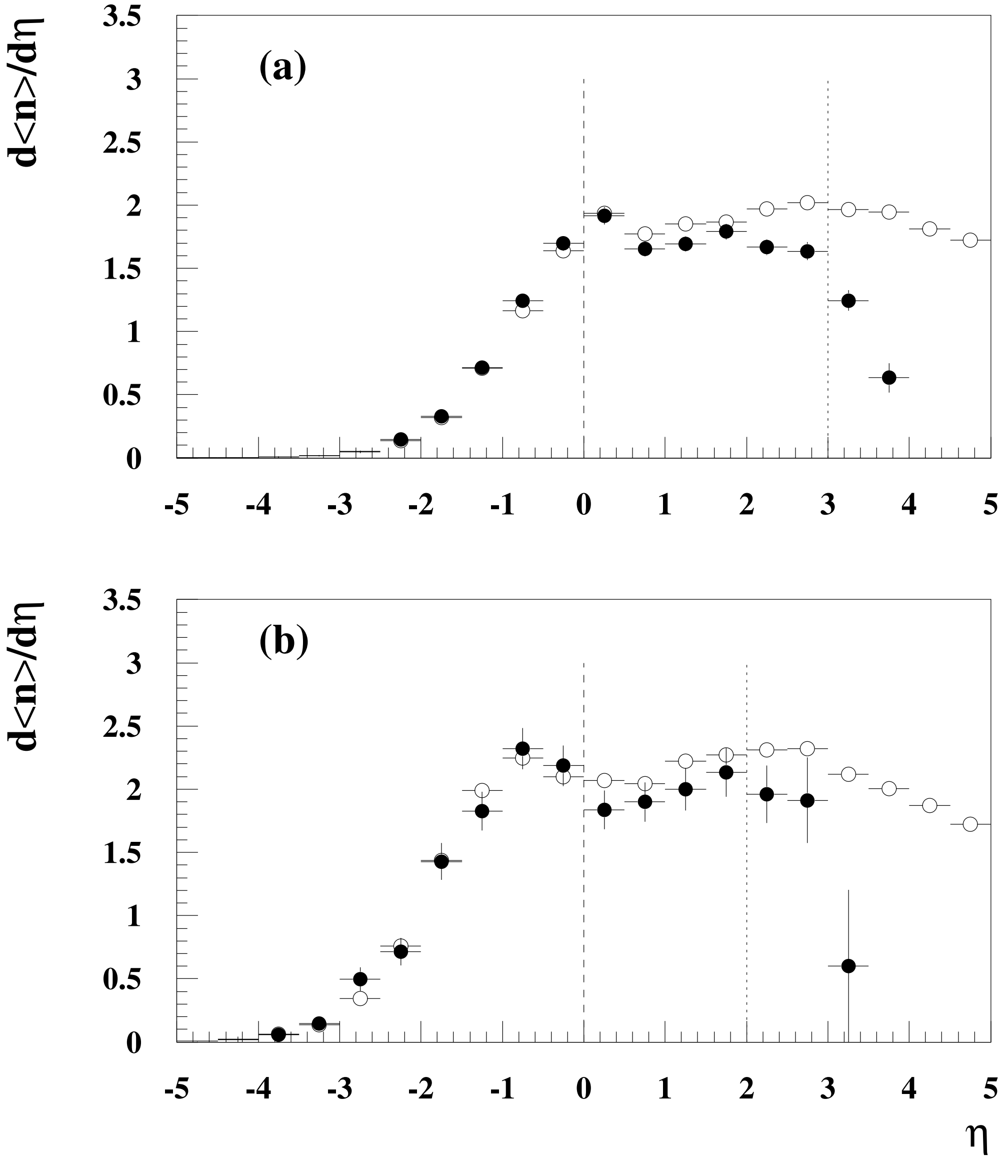

Figure 5.3: *Pseudo-rapidity distribution as seen in the Breit frame at (a) low and (b) high* Q^2*. Efficiency-corrected data is shown as closed circles and the predictions of the MEAR Monte Carlo as open circles. The Breit frame origin is at the position of the dashed line and the approximate (event averaged) position of the hadronic CMS origin is shown as a dotted line.*

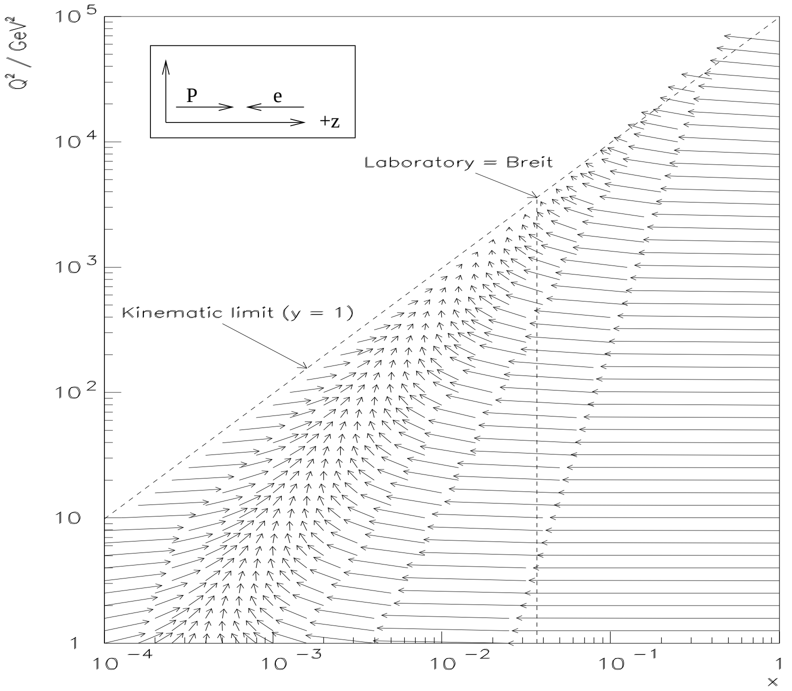

Figure 5.4: *A vector of magnitude* $\log\gamma$ *and in the direction of the active boost from the HERA laboratory frame to the Breit frame is shown at regular* (x,Q^2) *intervals. The kinematic point where the laboratory frame and Breit frames coincide is indicated.*

eventually becomes meaningless because of the lack of acceptance to correct. The exaggerated slow rise is a consequence of the mixed data but a plateau region can be readily identified at a height of roughly $d<n>/d\eta = 1.7(2.0)$ at low (high) Q^2. The average value of $(\ln W - \ln Q)$ for this data is 3.0 (2.0) at low (high) Q^2 and it can be clearly seen that the hadronic CMS origin occurs at the point where acceptance corrections are becoming difficult.

5.4 Properties of the Breit Frame

The magnitude and direction of the boost to be applied to each particle in order to reach the Breit frame is shown in figure 5.4 as a function of x and Q^2 [47]. The magnitude of the vectors is proportional to $\log(\gamma)$ purely for presentation reasons.

The figure shows that in general, a large negative longitudinal z boost is required at large x to overcome the momentum imbalance between the incident parton and the lower electron momentum. This is required to make the incident and scattered partons collinear but reversed and the energy of the incident and scattered electron equal, thus giving a current whose four-vector has no time-like component. Conversely at low x, the parton's momentum is small compared to that of the incident electron and large positive longitudinal boosts are required.

In the QPM when $x = E_e/E_P$, the scattered electron has energy equal to the incident electron beam and the current therefore has zero energy component. Interestingly there is, at $y = 1$ (the maximum Q^2 for any x) a unique point in phase space where the electron and parton backscatter and thus the HERA and the Breit system coincide. However, events at this point cannot be experimentally detected since the scattered electron and parton are backscattered from each other through the beam pipe. Figure 5.5 shows an isotropic emission of massless 10 GeV pions with an angular separation of 30° in the HERA system (solid lines). The effect of boosting the particles into the Breit frame (dashed lines) for two different (x,Q^2) points is shown in plots (a) and (b). It can be seen that the topology of the boosted vectors varies for different x and Q^2 values from which the boost vector is calculated. However, particles emitted along the positive z axis in the laboratory remain in this direction in the Breit frame regardless of the magnitude of the vector. The general relationship between the angle in the Breit frame and that in the HERA frame is shown in figure 5.6 for several different (x,Q^2). Again these results are presented for a 10 GeV pion. For the data used in this thesis it can be seen that the backward direction of the Breit frame transforms (solid black line) to the good acceptance area of the laboratory frame.

5.5 Breit Frame Event Selection

It is the aim of this analysis to select well-measured events requiring small acceptance corrections in order to measure track spectra in the Breit frame of reference. This selection should preferably be done using calorimetry information alone in order to avoid bias in charge track properties. The method adopted is as follows: First the four-momentum vectors which correspond to the direction and energy of calorimeter energy clusters (assuming pion masses) are boosted to the Breit frame using the

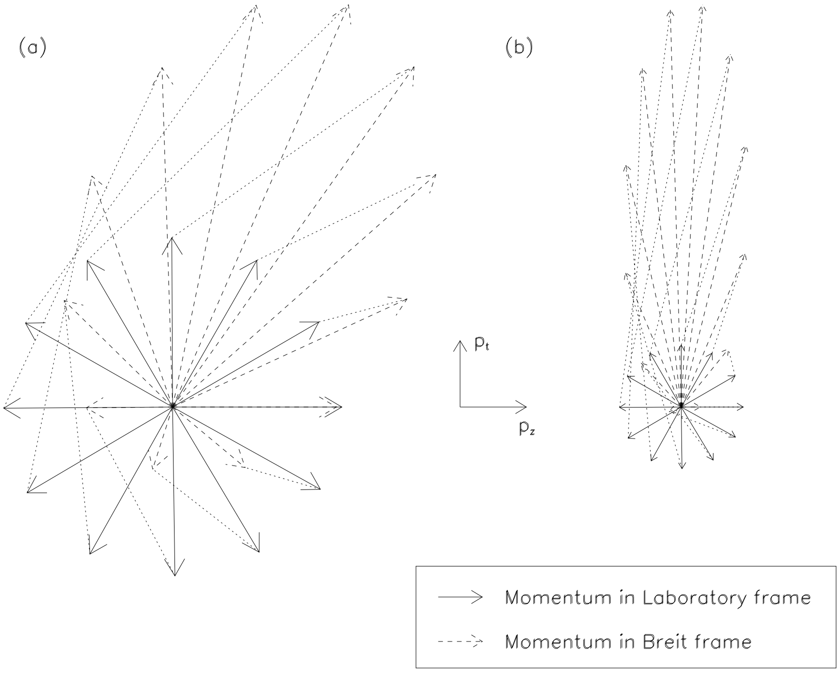

Figure 5.5: *Vectors in the HERA laboratory frame (full lines) are compared with their transformed values in the Breit frame (broken lines) for two different (x,Q^2) points of (a) (0.002,10) and (b) (0.02,100).*

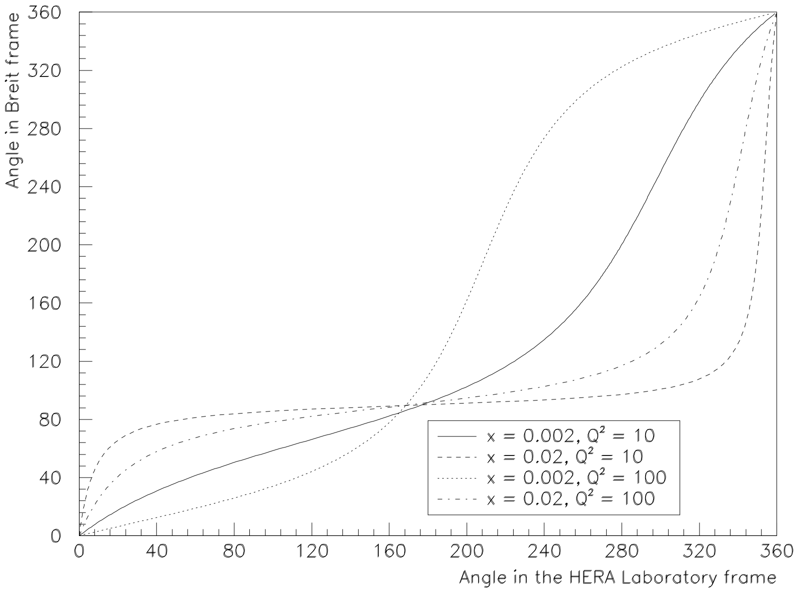

Figure 5.6: *The Breit-frame polar angle of a transformed 10 GeV pion vector, plotted against the original polar angle in the HERA laboratory frame.*

Data Sample	Good central calorimetry	Breit frame energy flow
$12 < Q^2 < 80$ GeV^2	3117	1945
$Q^2 > 100$ GeV^2	313	235

Table 5.1: *Size of data samples for this analysis. See text for definition of selections.*

(x, Q^2) values calculated solely from the electron kinematics. The $z < 0$ hemisphere, commonly referred to as the current hemisphere, is then examined in more detail.

To ensure that events have good and uniform track acceptance a selection is made such that events are taken for further analysis if 95% or more of the *total* observed energy in this hemisphere, $E^{total}_{BF(z<0)}$, originates from the laboratory polar region $10° < \theta < 150°$. This region is completely covered by the (LAr) calorimeter and thus has consistent calibration. More importantly, it also corresponds to the region of good acceptance for the trackers. Events which have no energy observed by calorimeters in the current fragmentation hemisphere are rejected from this analysis and are discussed separately in the next section.

Figure 5.7 shows event by event the fraction of energy in the current region of the Breit frame originating from three polar regions in the laboratory frame, (a) $\theta < 10°$, (b) $10° < \theta < 150°$ and (c) $\theta > 150°$, $E^{\theta_{lab}}_{BF(z<0)}$, to the total observed energy in the current hemisphere.

The number of events surviving this cut are also given in the first column of Table 5.1. Although 95% seems harsh, it can be clearly seen that most events, in general, have the majority of current related fragments contained within the central region of the detector as shown in figure 5.7(b). In (c) there are a small number of events that have energy fraction close to 1. These are events in which the struck quark is scattered backwards into the backward calorimeter and thus are at very low x_{Bj}. A similar trend is observed for the high Q^2 data however, the proportion of events in which the current is scattered backwards in the laboratory frame is smaller as high Q^2 events are generally at higher x_{Bj}.

For each event, the four-momenta of all energy clusters in the $z < 0$ hemisphere are added vectorially and the total energy, $E^{total}_{BF(z<0)}$, and angle, $\cos\Theta_{BF}$, of the

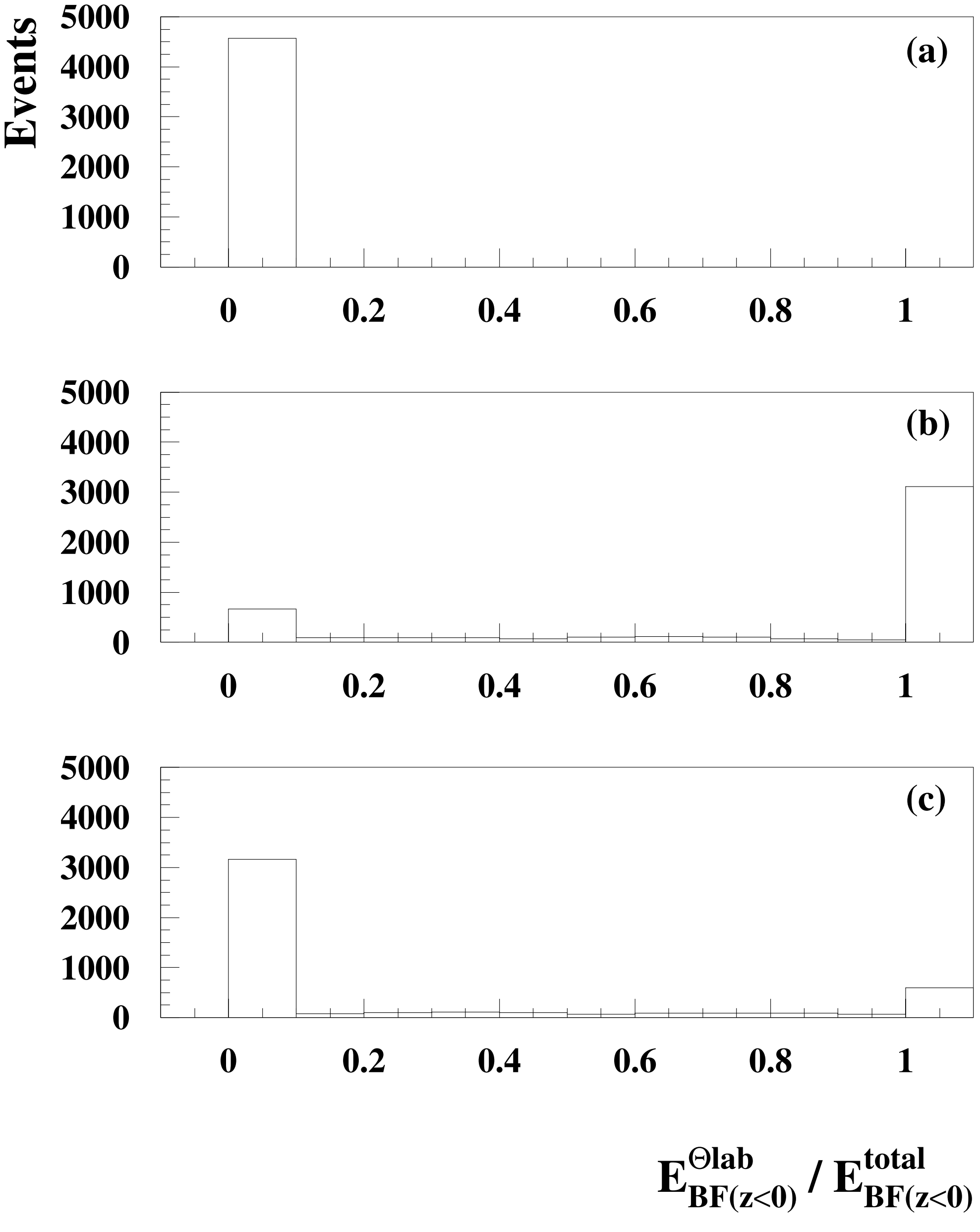

Figure 5.7: *The energy in the Breit frame current hemisphere that originates from three polar regions indicated in the figure,* $E^{\theta_{lab}}_{BF(z<0)}$*, as a fraction of the total energy in the current hemisphere of the Breit frame,* $E^{total}_{BF(z<0)}$*, for the low* Q^2 *data sample.*

resultant vector is found. Then, the total energy is plotted as a fraction of the event Q against the resultant cosine of the Breit frame polar angle, as shown in figure 5.8 for (a) low Q^2 and (b) high Q^2 data sets.

According to the QPM, a quark would be expected to have net summed energy vector of magnitude $Q/2$, pointing along the negative z axis i.e, $\cos\Theta_{BF} = -1$. At high Q^2 there is a tendency for the events to cluster in the area of this point. However, the spread of events is much greater at low Q^2 and there are a large number of events with little energy in the current hemisphere and/or with a net cluster emerging at large angles with respect to the beam axis. Figure 5.9 show these distributions for Monte Carlo events. It can be seen that apparatus - simulated event samples behave in exactly the same way as the data and, by comparing with the equivalent generated sample, that this spread is mainly caused by, but not totally the result of inexact reconstruction. In principle it ought to be possible to remove such events with no bias to track spectra by a simple cut on this event calorimeter plot.

Simple rejection of such events is a little problematic however as, at the generated level, some of these events show slightly different properties because of the loss of tracks to the target hemisphere through significant QCD radiation some of which would and some which would not (e.g, initial state radiation) have its equivalent in e^+e^- interactions. These higher order processes are discussed in section 5.6.

The possibilities of bias are tested by performing the analysis both on all events and also by rejecting events below the line joining $E^{total}_{BF(z<0)} = 0$, $\cos\Theta_{BF} = -1$ to $E^{total}_{BF(z<0)} = Q/2$, $\cos\Theta_{BF} = 0$ indicated in figure 5.8 and referred to as the 'Breit frame energy flow selection'. The event numbers surviving this topological selection are given as the final column in table 5.1.

5.6 Higher Order Processes in the Breit Frame

The Quark Parton Model of the Breit frame discussed so far is modified when $\mathcal{O}(\alpha_s)$ QCD corrections are applied. In these processes, the invariant mass of the $q\overline{q}$ or qg produced is no longer negligible. The difference between $\mathcal{O}(\alpha_s)$ processes in DIS and e^+e^- is the addition of boson-gluon fusion (BGF) and initial state QCDC radiation.

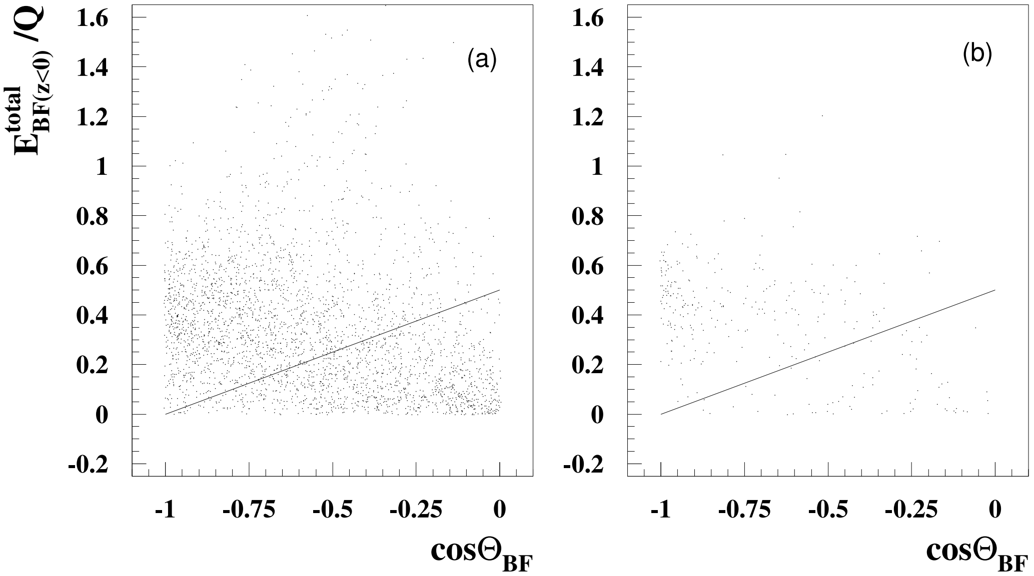

Figure 5.8: *The total energy of the summed calorimeter cluster four momentum vectors in the* $z < 0$ *hemisphere of the Breit frame is plotted as a fraction of the event* Q *against the cosine of the polar angle of the resultant vector, for (a) the low* Q^2 *and (b) the high* Q^2 *sample. The line indicates the cut for the secondary analysis described in the text.*

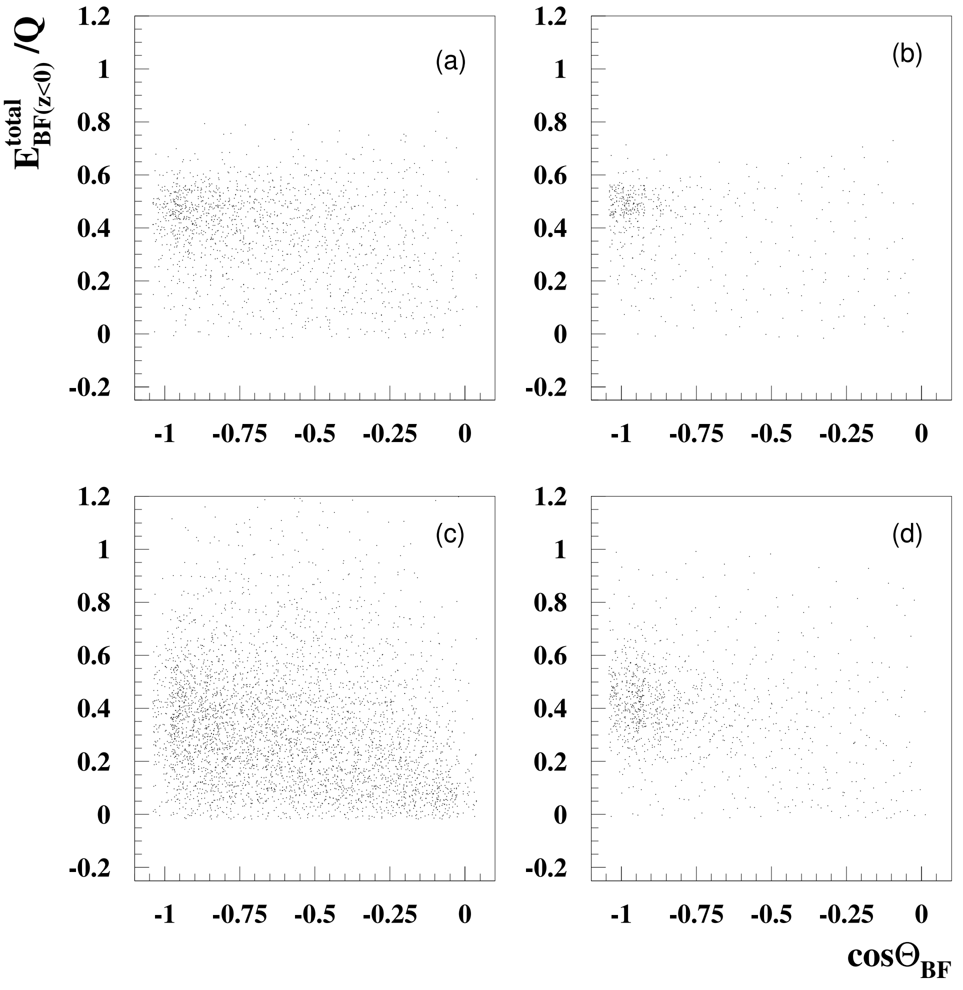

Figure 5.9: $E^{total}_{BF(z<0)}/Q$ *plotted against* $\cos\Theta_{BF}$ *for Monte Carlo events for (a) and (b) the low and high* Q^2 *generated samples respectively and, the corresponding distributions (c) and (d) after full detector simulation.*

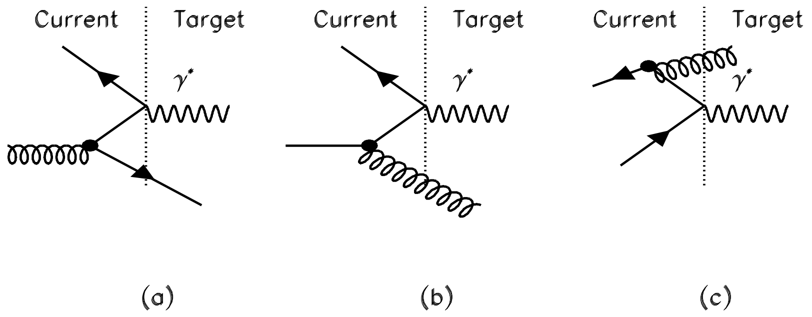

Figure 5.10: *$\mathcal{O}(\alpha_s)$ QCD processes in DIS and e^+e^-. Boson gluon fusion (a) and initial state QCDC (b) processes have no equivalent in the e^+e^- CMS. However, final state QCDC (c) radiation can occur in both systems.*

All these processes including final state QCDC can lead to the depopulation of the current region as shown figure 5.10.

In the QPM, the current hemisphere of the Breit frame when boosted back to the laboratory is a relatively narrow cone[5] containing the scattered quark. This is shown diagrammatically in figure 5.11(a). However, the higher order QCD processes discussed above modify this simplistic picture and give rise to a cone that either misses or partially contains current related fragments as shown in figure 5.11(b,c) respectively. These effects may result in a current hemisphere that has little or no energy in the Breit frame and net vector emerging at a large angle with respect to the beam axis as was shown in figure 5.9(a,b). Note that unlike the hadronic CMS the Breit frame is not a zero momentum frame and such events are perfectly compatible with kinematic constraints.

Events which have zero energy in the current hemisphere of the Breit frame are explicitly removed from the data and Monte Carlo samples. These events constitute about 20% (9%) of the events numbers listed in table 4.1 under the column 'Non diffractive events' for low (high) Q^2 sample.

---

[5] This is strictly not true. However, it is useful to think in terms of a 'cone' for the argument given in this section.

In order to check if there is any bias caused by the removal of these events, the analysis described in chapter 7 has been repeated in such a way as to include these events. It is perfectly obvious that an e^+e^- event can never be devoid of energy in any given hemisphere so such a procedure is certainly justified if the eventual aim is to compare to such interactions. If, on the other hand, the object were to be merely to investigate the properties of DIS events in the current hemisphere of the Breit frame there is a possibility of bias in such a procedure.

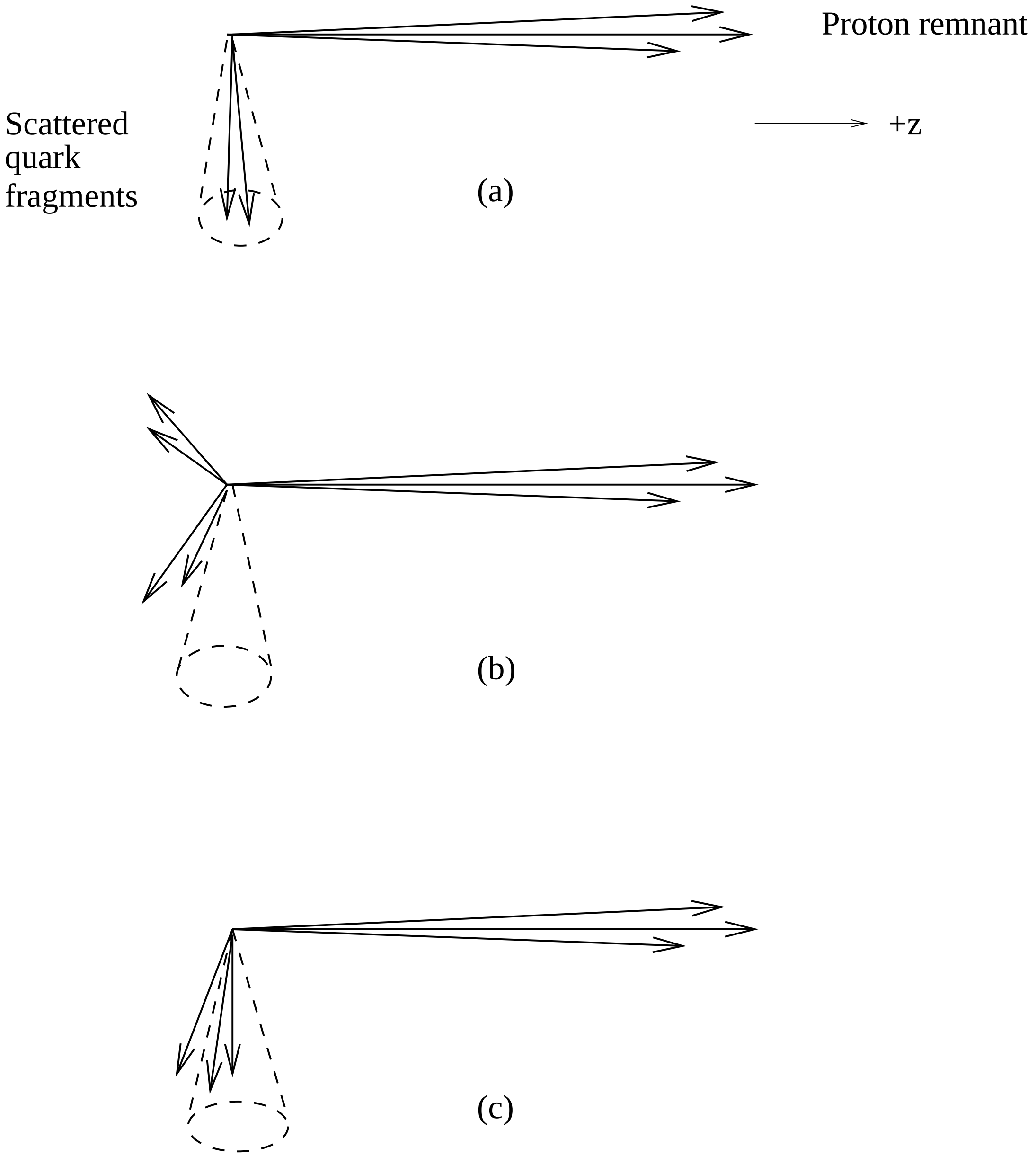

Figure 5.11: *In the QPM, the current hemisphere when boosted back to the laboratory frame is a narrow cone containing the scattered quark as shown is diagram (a). Higher order QCD process modify this picture resulting in a cone that is either empty (b), or one that contains only some of the current related fragments as shown in (c).*

Chapter 6

Data Corrections

6.1 Introduction

Throughout this thesis, no attempt is made to calculate a cross section. All distributions relating to event properties are normalised by the number of events in a given analysis bin and therefore getting the absolute number of events is not important. The shape of the distribution however is important. There are several methods available to correct experimental distributions for detector acceptance and inefficiencies. In this thesis, a vector bin-by-bin correction method is adopted. The philosophy behind this procedure is described below.

6.2 Data Correction

The MEAR Monte Carlo which provides the best description of energy flow measurements [25] within the H1 detector was used in the analysis to make acceptance corrections to the data. However, the LEPTO Monte Carlo utilising matrix elements matched to parton showers (MEPS) was used to test the sensitivity of the results to the model used. Corrections are determined from Monte Carlo simulations of the H1 detector response. The particle four vectors of the event generation are fed into H1SIM [13], the H1 detector simulation program containing a detailed description of the detector geometry, based on the GEANT [14] package.These events are then processed through the identical reconstruction and analysis chain as the data. These are henceforth known as Monte Carlo events.

The raw data are later corrected for detector effects by multiplying bin-by-bin by appropriate correction factors [77]. This vector of correction factors will be called the correction function[1]. These factors thus take into account the effects of finite detector resolution and acceptance, losses in dead material as well as the scattering of particles from secondary interactions into the fiducial volume. The correction factors are obtained by comparing two Monte Carlo distributions of a given event property, one at the generated level and the other after reconstruction. The corrected value for the i^{th} bin is then taken as $\frac{n_i^{gen}}{n_i^{rec}} \times n_i^{data}$, where n_{gen}^i is the number of generated charged hadrons (with a lifetime greater than 8 ns to ensure possible detection) and n_{rec}^i is the number of charged tracks reconstructed after simulation. The correction factor CF_i, is then equal to:

$$CF_i = n_i^{gen} / n_i^{rec} \tag{6.1}$$

Note that because of the effects of poor resolution and migration, CF_i may be less than or greater than unity, although if the analysis is conducted in a good region of acceptance, the corrections factors applied to the data should be smoothly varying and $\simeq 1$. Using this definition of CF_i above, the correction factors account for the following effects:

- acceptance effects due to geometry of the detector and its efficiency;
- track selection and reconstruction efficiency, including tracks associated to the decay products of K_s^0 and Λ which are mistakenly assigned to the primary vertex;
- if the bin width is greater than the resolution then migration between the current and target regions and migration effects between bins of the variable being considered.

The statistical error for the i^{th} bin was calculated extremely conservatively by assuming the generated and reconstructed event samples were not correlated, although in practice this is an over estimate because there will be a large degree of correlation;

$$\frac{\sigma(CF_i)}{CF_i} = \sqrt{\frac{1}{n_i^{gen}} + \frac{1}{n_i^{rec}}} \tag{6.2}$$

---

[1] The correction function is a set of separate scalar numbers and not a continuous function.

The philosophical problem in defining the correction factor in equation 6.1 is whether one should apply the Monte Carlo event selection at the generated level or whether such cuts should be applied at the reconstructed level. In this thesis only Monte Carlo events satisfying the same selections applied to the data as described in chapter 4 after full detector simulation and reconstruction are considered. This has the advantage that data and reconstructed Monte Carlo distributions can be compared fairly but has the disadvantage that, after corrections, you get back to the true physics for selections made on the *reconstructed* data.

For an infinitesimally sized bin width in some arbitrary distribution, corrections to the data are insensitive to the physics assumptions of the model. However, this hypothesis is still valid for distributions with a finite bin width, providing the resolution of the variable is smaller than the bin width of the distribution. As long as the above is true the method does not demand a perfect description of the data, since the small bin width is correspondingly a small part of phase space. However, if the Monte Carlo is, in addition, a good description of the data then even resolution effects are automatically corrected for.

6.3 Effect of Poor Simulation of Azimuth

It was shown in chapter 4.6.4 that the dead regions in ϕ are modelled reasonably well. However, it is interesting to note that the simulation of these regions does not need to be perfect. The fragmentation functions presented in chapter 7 are not correlated to ϕ and therefore the correction procedure should give only an error of normalisation but not of shape. Thus, for a poor simulation of the ϕ distribution, we would get the wrong multiplicity but the peak and width of the fragmentation function ought to be unaffected. The reader should bear in mind that in the early stage of this analysis, an adequate simulation of the ϕ distribution was not available. The reconstructed Monte Carlo predicted a flat distribution. These regions were excluded from the analysis and the results obtained were in agreement with those presented in chapter 7.

Chapter 7

Charged Particle Spectra in the Breit Frame

7.1 Introduction

The fragmentation properties of the evolved parton are studied in the current fragmentation region of the Breit frame. Throughout this thesis the Breit frame current region is defined as a hemisphere for hadrons with longitudinal momentum $p_z < 0$ in this frame. However, this is only a working definition and an attempt is made to estimate the level of current and target-associated tracks in a given hemisphere, given an incoherent additive approximation.

7.2 Current and Target Separation

Having selected events using calorimetry as described in chapter 5, track properties in the Breit frame are now investigated, beginning with the distribution $\cos\theta_B$, the cosine of the polar angle for charged particles, as shown in figure 7.1(a,b) and presented in table A.1. These distributions are corrected bin-by-bin for losses due to detector acceptance and inefficiencies using simulated and reconstructed Monte Carlo events as described in chapter 6.

The measurements are from vertex constrained tracks measured in either the central or forward tracker (or both) which satisfy the cuts described in chapter 4 in particular transverse momentum $p_t > 150$ MeV or momentum $p > 500$ MeV respectively. For each event, the boost to the Breit frame has been reconstructed using the scattered electron energy and kinematic quantities x and Q^2 obtained from

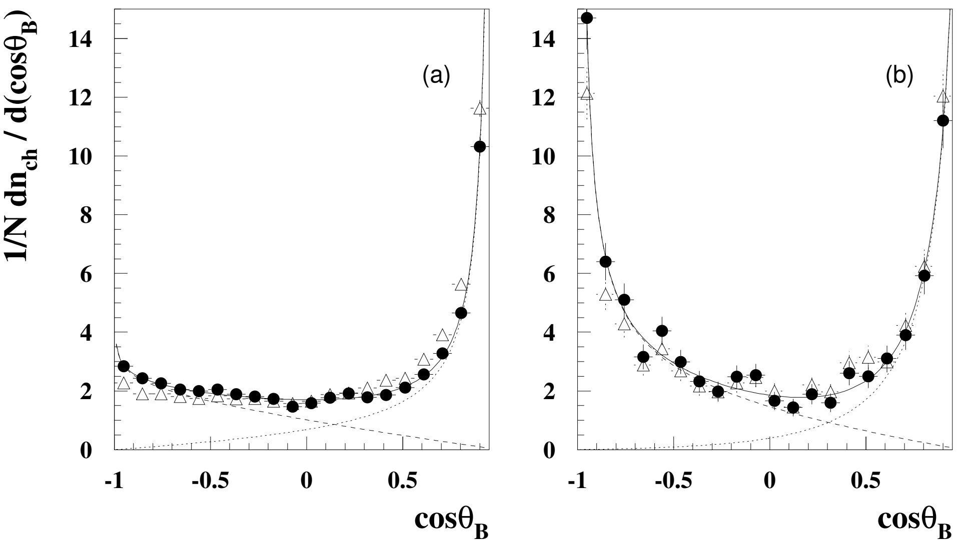

Figure 7.1: *Distribution of the cosine of the Breit frame polar angle for tracks of (a) the low Q^2 and (b) the high Q^2 sample, with statistical errors only. The open triangles show the data before the Breit frame energy flow selection. The solid line corresponds to the empirical fit described in section 7.2.1 where the dashed line is the nominal quark contribution and the dotted line that of the target.*

the electron only method. The charged tracks belonging to each event are then boosted using these quantities and assigned to the current fragmentation region by virtue of the longitudinal momentum component in the boosted frame, $p_z \leq 0$.

The corrected data in figure 7.1(a,b) display an obvious peak in the positive-z (beam) direction and also in the negative-z (quark) direction at high Q^2 but which is much less clear at low momentum transfer.

The correction factors applied to the data to obtain the corrected distributions of figure 7.1 are shown in figure 7.2(a,b) for the low and high Q^2 samples respectively. Note that both figures 7.1 and 7.2 omit the bin corresponding to the most forward direction where poorly known properties of the proton remnant and poor acceptance due to the beam pipe make correction factors extremely unreliable. For $-1.0 < \cos\theta_B < 0.95$, avoiding these effects, the average correction factor is 1.37 for low Q^2 and 1.38 for the high Q^2 sample and both vary smoothly especially for the region of principal interest for $\cos\theta_B < 0.0$.

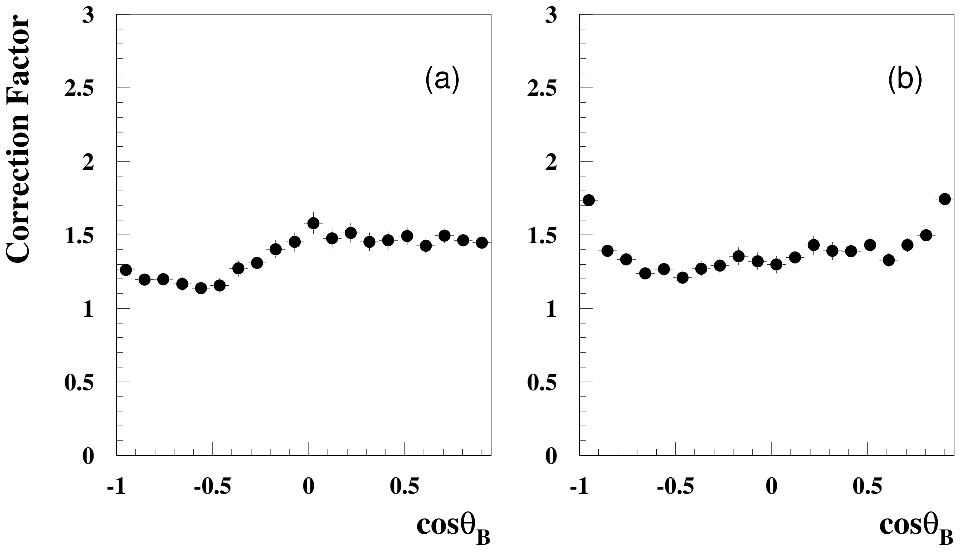

Figure 7.2: *The data presented in figure 7.1 are bin-by-bin corrected for losses due to acceptance and inefficiencies calculated using simulated and reconstructed Monte Carlo events. The corrections are small and vary smoothly for* $\cos\theta_B < 0$.

In a strict quantum-mechanical interpretation no track can be said to ‘belong’ to either the jet or target remnant, wherever it lies in the Breit frame, given a fragmenting colour string stretched between the two systems. However, it is clear from figure 7.1 that the concept of separable current and target hemispheres is a useful approximation as Q^2 increases but simply a question of definition at the lowest Q^2 values. In this thesis the properties of tracks in the current hemisphere of the Breit frame are examined and compared with those properties in e^+e^- interactions. However, to estimate the possible losses and contamination involved in using a selection of one hemisphere of the Breit frame, as a result of physics and/or poor resolution, two methods are investigated.

7.2.1 Empirical Fits

The first investigation assumes there are two incoherent sources of hadronic fragments, the current and the target. These sources then give hadrons on the opposite side of the divider line by a combination of physics and/or poor resolution. Firstly,

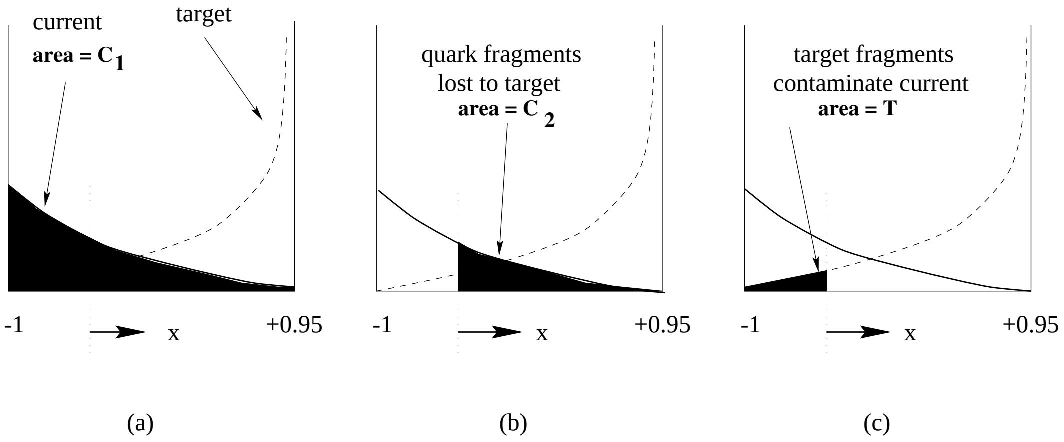

(a)

(b)

(c)

Figure 7.3: *Empirical fits are used to describe the current and target regions. In (a) the current (solid line) and target (dashed line) are shown as a function of $x = \cos\theta_B$. The area indicated in (a) is the total average charged multiplicity associated to the current quark. The area shown in (b) is its average charged multiplicity lost to the target region, which arises as a consequence of defining one section of the Breit frame to represent the quark fragmentation region. This line is indicated by the arrow shown in each of these diagrams. In (c) the shaded area shows the tail of target related fragments which contaminate the current region to the left of the divisor.*

an empirical fit is performed on the data using an arbitrary function of the form

$$f(x) = \underbrace{A(1-x)e^{a(1+x)^{\alpha}}}_{current} + \underbrace{B(1+x)e^{b(1-x)^{\beta}}}_{target} \tag{7.1}$$

where $x = \cos\theta_B$. The expressions have been chosen merely to be $x \leftrightarrow -x$ symmetric and to give a function which describes the data. Figure 7.1 shows the result of such fits superimposed on the data but for clarity this is repeated in figure 7.3(a) for the current (solid line) and target (dashed line) functions described in equation 7.1 between $-1.0 \le x \le 0.95$. The shaded area, C_1 indicates the total charged multiplicity associated to the current quark. The dotted line which is an arbitrary point in $\cos\theta_B$ space indicates current/target separation. In (b) the shaded area, C_2 corresponds to the charged multiplicity lost from the current quark to the target region as a consequence of defining a given divisor, x. The relative loss of the current (quark) fragments to the target region for a given x is then C_2/C_1. The contamination to the current region is the area T indicated in (c) divided by the contribution of the current to the left of the divisor and is $T/(C_1 - C_2)$.

This and fits to other possible functional forms which also described the data adequately suggest that, in the Breit frame, the selection $\cos\theta_B = 0.0$ roughly equalises loss and contamination between the quark and target regions and that they are $\sim 5\%$ level at high Q^2 but at the ≈ 20 - 25% level at low Q^2.

7.2.2 Resolution in $\cos\theta_B$

The second investigation assumes nothing about the origin of the particles but merely seeks to see what is the net migration/immigration into a region caused by poor resolution of both electron and hadronic kinematic variables. The accuracy of the boost to the Breit frame depends on the correct reconstruction of the kinematic quantities x and Q^2. The Breit frame z-axis origin distinguishes the current hemisphere from the target hemisphere. If the reconstructed quantities deviate significantly from the true (generated) values then the reconstructed and true axes will not coincide. In such cases, the reconstructed axes are translated and/or rotated with respect to the true axes and particles which were generated with $p_z < 0$ can have $p_z > 0$ viewed in the reconstructed frame.

The level of migration effects due to detector resolution effects was evaluated using the MEAR Monte Carlo. The generated energy and momentum components of stable charged hadrons were boosted into the Breit frame using

- the *generated* virtual photon and;
- the virtual photon *reconstructed* from the scattered electron quantities.

Particles were assigned to the current or target region depending on the sign of their generated longitudinal momentum component in the Breit frame. Table 7.1 presents the number of particles generated in the current and target regions using the generated virtual photon, and the number of particles which migrate from one region to the other due to boost reconstruction alone i.e using the reconstructed virtual photon. The values are shown for each of the ten analysis bins used in this thesis. The results presented in table 7.1 show that in the current region, $\sim 10-15\%$ of the particles generated in this hemisphere migrate to the target region. This percentage has a Q^2 dependence which generally becomes smaller as Q^2 increases. However, the percentage of generated particles in the target hemisphere which migrate to the current region is generally constant and less significant at $< 2\%$.

Q^2 Interval	**Current Hemisphere**		**Target Hemisphere**	
(GeV^2)	Generated	Migrate to Target	Generated	Migrate to Current
12 → 15	879	131	7453	127
15 → 20	1562	241	11213	170
20 → 40	3981	596	24063	309
40 → 60	1967	222	9309	116
60 → 80	1032	108	4174	65
100 → 175	1911	63	7606	30
175 → 250	6168	654	19036	149
250 → 450	9128	1510	23974	113
450 → 1000	6088	494	12746	85
1000 → 8000	3060	122	4991	33

Table 7.1: Particle migrations are studied using the MEAR Monte Carlo at the generated level.

Another contribution to migration arises from effects due to track mis-reconstruction. Such migration effects are accounted for in the Monte Carlo correction procedure and are discussed below.

The resolution in $\cos\theta_B$ as a consequence of the boost may be found from

$$\sigma_{boost}(\cos\theta_B) = \text{ rms}\,(\cos\theta_B^{rpge} - \cos\theta_B^{rpre}) \tag{7.2}$$

where $\cos\theta_B^{rpge}$ is measured using reconstructed particles boosted to the Breit frame using the four-momentum components of the generated virtual photon and $\cos\theta_B^{rpre}$ is measured using reconstructed particles boosted to the Breit frame using the four-momentum components of the reconstructed virtual photon. The resolution in this variable due to the boost *only* is shown in figure 7.4(a,b).

Migrations will also arise due to the errors associated with track reconstruction. The resolution error due to track reconstruction is calculated for the particle using

$$\sigma_{track}(\cos\theta_B) = \text{ rms}\,(\cos\theta_B^{rpge} - \cos\theta_B^{gpge}) \tag{7.3}$$

where $\cos\theta_B^{rpge}$ is measured using reconstructed particles boosted to the Breit frame with the generated virtual photon, and $\cos\theta_B^{gpge}$ is measured using generated particles which are boosted using the generated virtual photon. The resolution due to track reconstruction effects is shown in figure 7.5(a,b).

Finally, the resolution error in $\cos\theta_B$ which is a combination of the boost error due to the measurement resolution (σ_{boost}) on the kinematic quantities x and Q^2 as

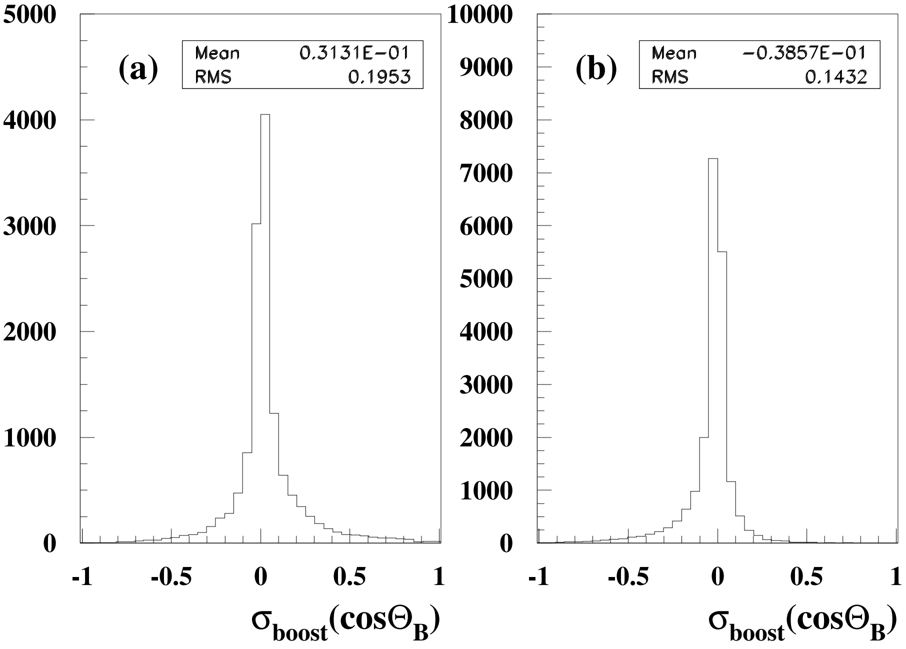

Figure 7.4: *Boost reconstruction error for (a) the low Q^2 and (b) the high Q^2 Monte Carlo events samples. The resolution error due to measurement errors on the kinematic variables is calculated for the particles using* $\sigma_{boost}(\cos\theta_B) = \text{ rms}\,(\cos\theta_B^{rpge} - \cos\theta_B^{rpre})$ *where* $\cos\theta_B^{rpge}$ *is measured using reconstructed particles boosted to the Breit frame with the generated virtual photon, and* $\cos\theta_B^{rpre}$ *is measured using reconstructed particles which are boosted using the reconstruction virtual photon.*

shown in figure 7.4 and, the error due to track reconstruction (σ_{track}) indicated in figure 7.5 is;

$$\sigma_{total}(\cos\theta_B) = \text{ rms}\,(\cos\theta_B^{rpre} - \cos\theta_B^{gpge}) \tag{7.4}$$

where $\cos\theta_B^{gpge}$ is measured using generated particles boosted using the generated virtual photon and $\cos\theta_B^{rpre}$ is measured using reconstructed particle boosted using the reconstructed virtual photon. The total resolution in the Breit frame polar angle is shown in figure 7.6.

These results indicate that the resolution of a particle's Breit frame polar angle is dominated by measurement errors of the reconstructed electron and indicate that at $\cos\theta_B \approx 0$, $\sigma_{total}(\cos\theta_B) \approx 0.21(0.15)$ at low (high) Q^2.

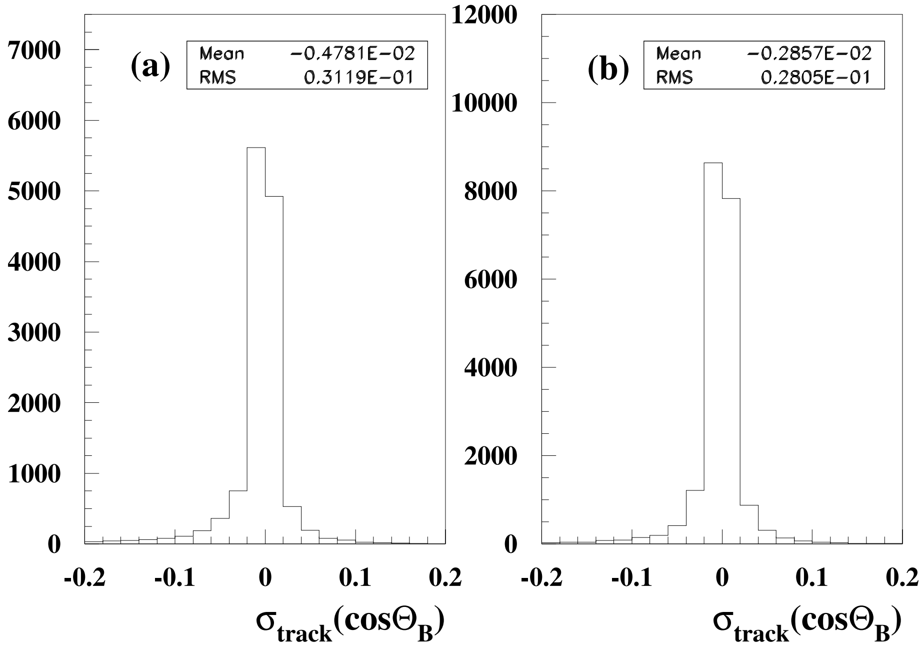

Figure 7.5: *Track reconstruction error for (a) the low* Q^2 *and (b) the high* Q^2 *Monte Carlo events samples. The resolution error due to track reconstruction is calculated for the particle momentum using* $\sigma_{track}(\cos\theta_B) = \mathrm{rms}\,(\cos\theta_B^{rpge} - \cos\theta_B^{gpge})$ *where* $\cos\theta_B^{rpge}$ *is measured using reconstructed particles boosted to the Breit frame with the generated virtual photon, and* $\cos\theta_B^{gpge}$ *is measured using generated particles which are boosted using the generated virtual photon.*

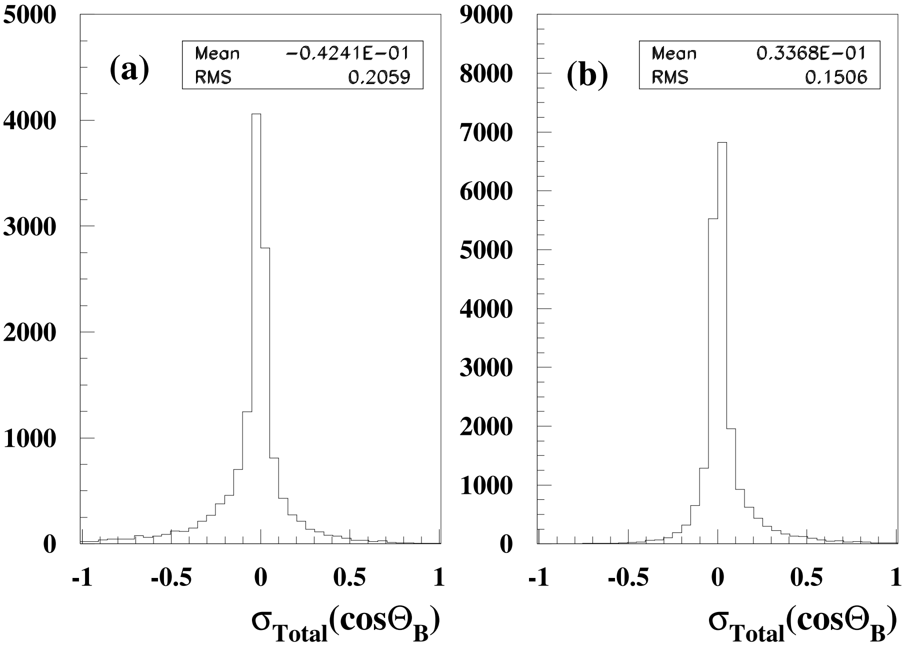

Figure 7.6: *The simulated event studies show that the resolution of a particles polar angle in the Breit frame is much poorer than its momentum and indicate that at* $\cos\theta_B \approx 0$*, the total error* $\delta\cos\theta_B \approx \pm 0.21(0.15)$ *at low (high)* Q^2*.*

7.3 Fragmentation Functions

The momentum distribution of the hadrons from quark fragmentation in e^+e^- interactions roughly scales with $\sqrt{s_{ee}} = E^*$, the overall centre of mass system (CMS) energy. The ratio of the momentum of a given charged hadron to the maximum energy that it could have, $x_p = 2p^{\pm}_{hadron}/E^*$, is thus a natural variable in terms of which e^+e^- experiments [42, 43] have described hadronic spectra. This variable also has the advantage of being independent of the difficulties involved in any jet or thrust axis determination. It is manifestly not Lorentz invariant and it will therefore become necessary to identify an equivalent frame for ep in which comparisons can be properly made. In the Breit frame, the variable $x_p = 2p^{\pm}_{hadron}/Q$ where $Q \equiv E^*$ will be tested in this thesis as equivalent to the e^+e^- definition. Reference [78] discusses other possible variables in the Breit frame incorporating, for example, $p_{||}$ which gives directional information. Since the aim of this thesis is to compare with e^+e^- experiments, we have chosen to remain with a compatible definition. The distribution defined as

$$D^{\pm}(x_p) = (1/N) \times dn^{\pm}_{tracks}/dx_p \qquad (7.5)$$

is a charged track density normalised by the number of events and is termed the fragmentation function. It characterises the complete process which includes parton shower development as well as non-perturbative hadronisation. In principle the fragmentation function is defined for a given quark to a given hadron species, but tagging techniques[1] usually dictate that the data is effectively an integrated average.

The fragmentation function is a "soft" function rising rapidly as x_p decreases but then turning over near $x_p = 0$. The charged particle fragmentation functions are displayed in figure 7.7(a,b) as a function of $x_p = 2p^{\pm}_{hadron}/E^*$ for the current hemisphere of the Breit frame and for two Q^2 intervals. These figures utilise the selections of chapter 4 including the Breit frame energy flow selection of chapter 5. The individual fragmentation functions, for positive and negative hadrons, are indistinguishable, at least with the present statistics in the current kinematic areas of

---

[1] In e^+e^-, tagging techniques such as dE/dx have allowed fragmentation comparisons between charged pions and kaons etc. However, within this thesis, dE/dx information is not used on account of it poor reliability at this stage of the H1 apparatus. We will thus assume that all charged hadrons are $\pi^{\pm}$.

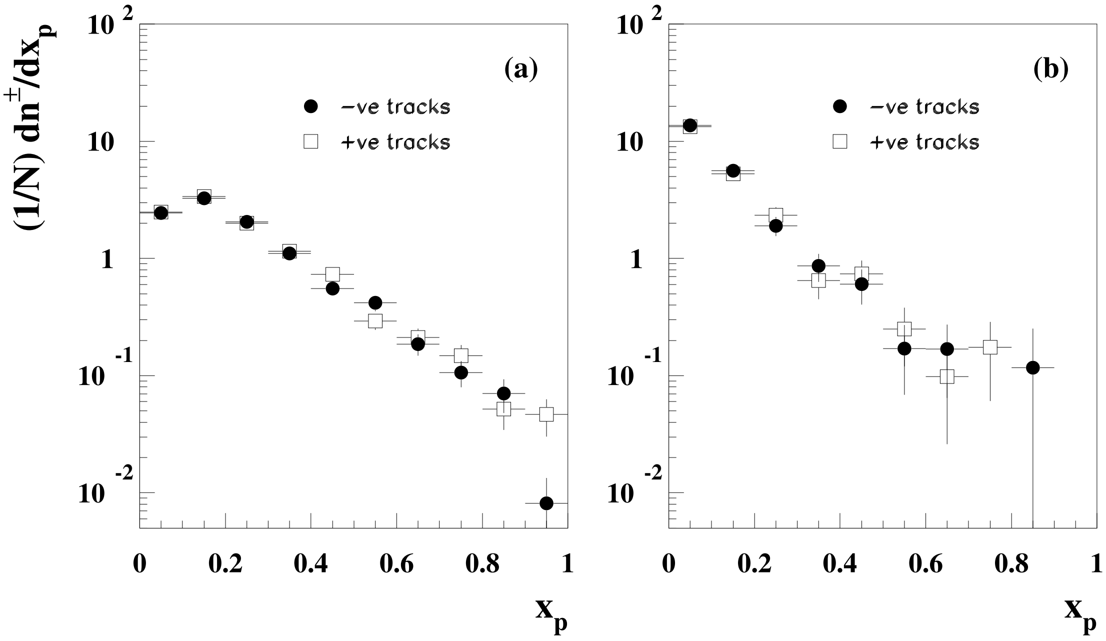

Figure 7.7: *The fragmentation functions, $D(x_p)$, for the current hemisphere of the Breit frame shown separately for positive and negative tracks, for (a) the low Q^2 and (b) the high Q^2 with statistical errors only.*

investigation, and are treated inclusively for the rest of this thesis. These results are presented in table A.2. Changing the fragmentation variable to be $\xi = \ln(1/x_p)$ expands the turn-over region, and the expectation of the Modified Leading Logarithm Approximation (MLLA) to perturbative QCD predicts that, for the partons, ξ is distributed in a roughly Gaussian manner with mean increasing as $\ln(E^*)$. Assuming Local Parton-Hadron Duality (LPHD) the same behaviour is expected for any type of hadron. Redefining the fragmentation function to be $D(\xi) = (1/N) \times dn_{tracks}/d\xi$ results in the Gaussian shape of figure 7.8(a,b). The area (average multiplicity) increases and the peak moves to higher values of ξ at higher Q^2. These distributions are also corrected bin-by-bin (see chapter 6 for discussion on correction method) for acceptance and efficiency, although again the dependence is small and smooth especially in the case of the variable ξ. These results are tabulated bin-by-bin in table A.3. Figure 7.9(a,b) show the fragmentation function for low and high Q^2 re-

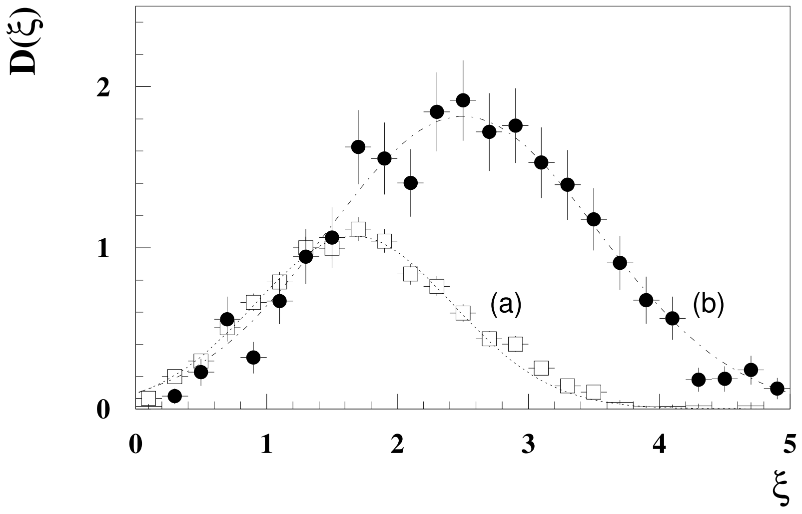

Figure 7.8: *The fragmentation functions for the current hemisphere of the Breit frame, $D(\xi)$ for (a) the low Q^2 and (b) the high Q^2 with statistical errors only, and with simple Gaussian fits superimposed. The average Q values for these samples are (a) 5.4 GeV and (b) 19.0 GeV.*

constructed MEAR events. It can be clearly seen that the shape of the distributions in figure 7.8 are well described by the Monte Carlo.

7.4 Resolution in ξ

As with $\cos\theta_B$ the resolution $\sigma_{Total}(\xi)$ due to the overall measurement of ξ, consists of a contribution from track reconstruction as well as the boost reconstruction. It has been shown that errors due to track reconstruction are small compared to uncertainties in the boost reconstruction as discussed in the previous section, but in any case, the Monte Carlo correction procedure takes account of both contributions since the shape is well described.

For physics reasons, the width of the ξ bins in this analysis are chosen to be commensurate with the resolution of ξ in the current region. The resolution of ξ is shown in figure 7.10(a,b) for the current fragmentation region of the Breit frame. A bin width of 0.2 in ξ has been used throughout this thesis.

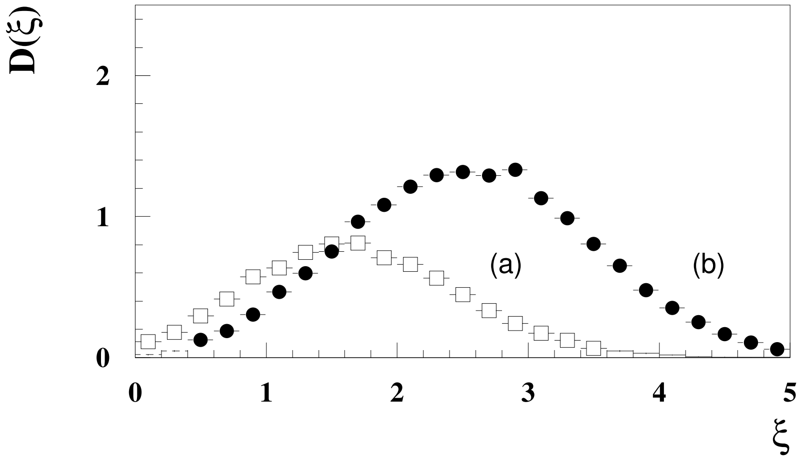

Figure 7.9: *The fragmentation functions for the current hemisphere of the Breit frame, $D(\xi)$ for (a) the low Q^2 and (b) the high Q^2 with statistical errors only, for reconstructed MEAR events.*

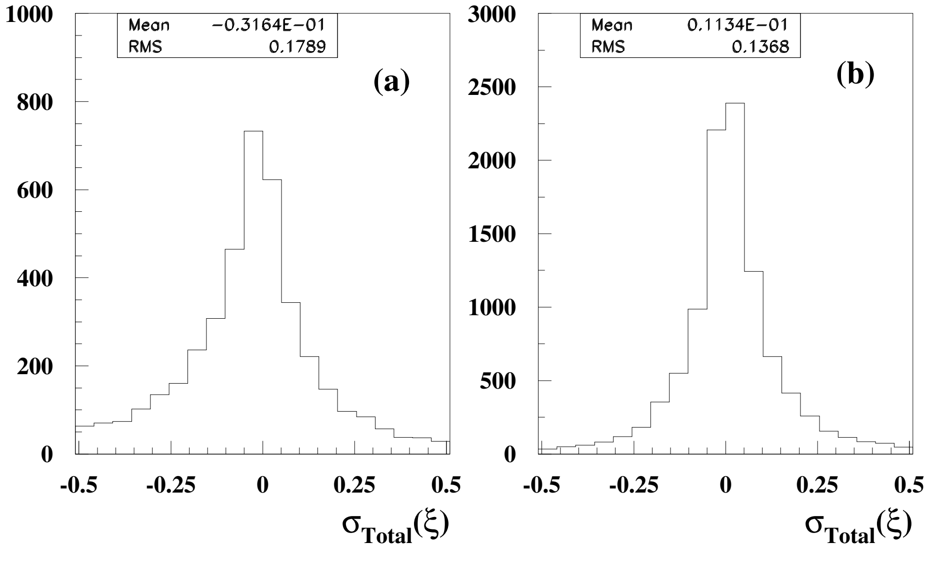

Figure 7.10: *The total resolution error $\sigma_{Total}(\xi)$ for (a) the low Q^2 and (b) the high Q^2 simulated Monte Carlo samples. For particles in the current hemisphere of the Breit frame a bin width of 0.2 in ξ is used for both data sets.*

7.5 Evolution of the Fragmentation Function

The low and high Q^2 data of figure 7.8 have each been further subdivided to give a total of ten intervals of Q as described in chapter 4.9, in order to study the evolution of the area, peak and width of the fragmentation function in more detail.

7.5.1 Corrections to Multiplicity

QED radiative corrections have an influence on the multiplicity yield and have not been corrected for in the correction procedure as they are not included in the Monte Carlo. However, the effects are expected to be small due to the restricted range in y. The effect has been investigated with the program DJANGO 2.1 which interfaces HERACLES [79] to LEPTO and thus includes radiative effects. This analysis shows no effective variation over the fragmentation peak area but indicates the need for an overall multiplicity normalisation correction of $+4.3 \pm 0.3\%$ which has been included.

Due to the limited statistics of the ten Q^2 data sub-samples, the Monte Carlo corrections discussed earlier do not correct for data bins that are empty or 'missing'. This is purely a consequence of the size of the data sample and not the results of, for example, an unforseen bias in the event selection. The missing bins occur in the tails of the ξ distributions and therefore do not affect the results described in section 7.5.4. For each analysis bin, a small upward multiplicity correction is applied which is based on the generated Monte Carlo distribution. This correction is small and generally $< +1\%$ for each sub-sample.

7.5.2 Multiplicity Evolution of the Fragmentation Function

The variation of the integrated area which is equal to the the mean charged particle multiplicity, $< n_{ch} >$ is shown in figure 7.11 for events which satisfy the Breit frame energy flow selection. The results are presented in the second column of table 7.2 with statistical and systematic errors. For comparison, the results for the total current hemisphere with statistical errors only are shown in the final column.

Figure 7.11 show the results obtained both with and without the Breit frame energy flow selection. There appears to be a significant difference, especially at low Q^2. Since these data are corrected for known acceptance effects (i.e after correction

Q^2 Interval	**Energy flow selection**	**Total current hemisphere**
(GeV^2)	$< n_{ch} > \pm$ stat $\pm$ sys	$< n_{ch} > \pm$ stat
12→15	1.54±0.11±0.07	1.35±0.08
15→20	1.77±0.10±0.08	1.63±0.08
20→40	2.18±0.08±0.10	2.02±0.06
40→60	2.60±0.13±0.12	2.39±0.11
60→80	3.20±0.19±0.14	2.84±0.16
100→175	4.05±0.58±0.12	3.71±0.50
175→250	4.73±0.35±0.14	4.05±0.29
250→450	4.75±0.32±0.14	4.00±0.25
450→1000	5.43±0.39±0.16	4.97±0.36
1000→8000	6.27±1.20±0.19	5.67±1.02

Table 7.2: *Average charged multiplicity for the Q^2 intervals given using either the energy flow selection or the total current hemisphere of the Breit frame.*

we are not concerned with reconstruction problems), the difference is ascribed to QCD radiation differentially depositing particles in the target hemisphere. Such events have lower particle multiplicities in the current hemisphere than events which do not radiate in the same interval of Q. This effect has been observed at the generated level of Monte Carlo and was discussed in chapter 5.6.

In e^+e^- experiments, a number of phenomenological models [80] have been proposed to describe the evolution with energy of the mean charged multiplicity. A fit according to the empirical relation

$$< n_{ch} >= a + b \cdot \ln(E^{*2}) + c \cdot \ln^2(E^{*2}) \tag{7.6}$$

yields $a = 3.297 \pm 0.091$, $b = -0.394 \pm 0.056$ and $c = 0.263 \pm 0.007$ with $\chi^2 = 69.1$ for 81 degrees of freedom [80].

To allow a comparison with the ep data, the mean charged multiplicities for e^+e^- events implied by this fit have been reduced by a factor two to correspond to results for a single hemisphere and a further 8.1 % (the average of available data) reduction has been made to account for K^0 and Λ decay tracks. The results of this parameterisation are shown superimposed (solid line) in figure 7.11. In general, the agreement between the H1 data and the e^+e^- fit are good but at low Q^2 the data show a lower average charged multiplicity and differences with e^+e^- data are more significant. This will be discussed in the next section but, it can be seen

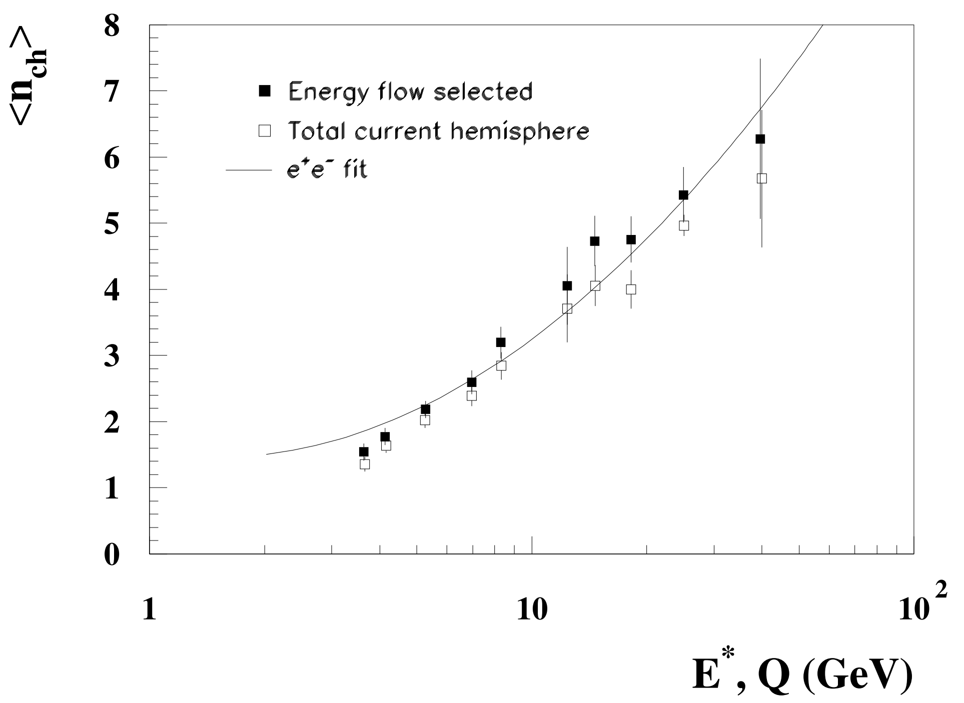

Figure 7.11: *Average charged particle multiplicity in the current region of the Breit frame for data before (open squares) and after (solid squares) the energy flow selection as a function of* Q *compared with a parameterisation (line) of one half of average corrected track multiplicities in* e^+e^- *events as a function of* E^*.

from figure 7.11 that Q is a good equivalent scaling variable to be compared with $E^* \equiv \sqrt{s_{ee}}$ in the e^+e^- system.

7.5.3 Multiplicity Comparison with e^+e^-

In comparison with e^+e^-, the data at low Q^2 show a lower average charged multiplicity. These differences becomes more significant in the lowest Q^2 bins and are as large as 2 or 3 standard deviations. The reasons for this difference is hypothesised to be attributed to $\mathcal{O}(\alpha_s)$ QCD effects which give rise to events that are not mirrored in the e^+e^- CMS. These higher order processes are those discussed in section 5.6. One would expect that the multiplicities in the current region of the Breit frame would be in better agreement with e^+e^- data if boson-gluon fusion (BGF) and initial state QCD compton events could be removed from the final sample thus giving a sample of events that more closely approximate those in the e^+e^- interactions.

To test this hypothesis, an exclusive multiplicity analysis is done for different regions in the $E^{total}_{BF(z<0)}/Q$ (vs) $\cos\Theta_{BF}$ calorimeter measurement plane. Semi-circles centred at the point (0.5,-1.0), the QPM prediction in this plane, of increasing radius are defined as shown in figure 7.12. The multiplicity in each ring is then plotted as a function of the outer ring radius, R, as shown in figure 7.13(a,b) for the low and high Q^2 corrected data samples. For comparison, multiplicities predicted by the MEAR Monte Carlo are also shown. It can be clearly seen that as the ring radius decreases, the average multiplicities move towards those of half an e^+e^- event for $E^* = Q$. At a detailed level, agreement between particle multiplicities can not be expected to be precise because of the comparative 'flavour democracy' expected in e^+e^- annihilation, although there has been no significant observed multiplicity difference other than for b-events. Jets initiated by b-quarks constitute some 22% of multihadronic events of e^+e^- events, have roughly 13% higher average charged multiplicity at LEP energies [81]. Such flavour effects are thus at the 3% level which is much less significant than the present errors and therefore, no attempt is made to correct for them.

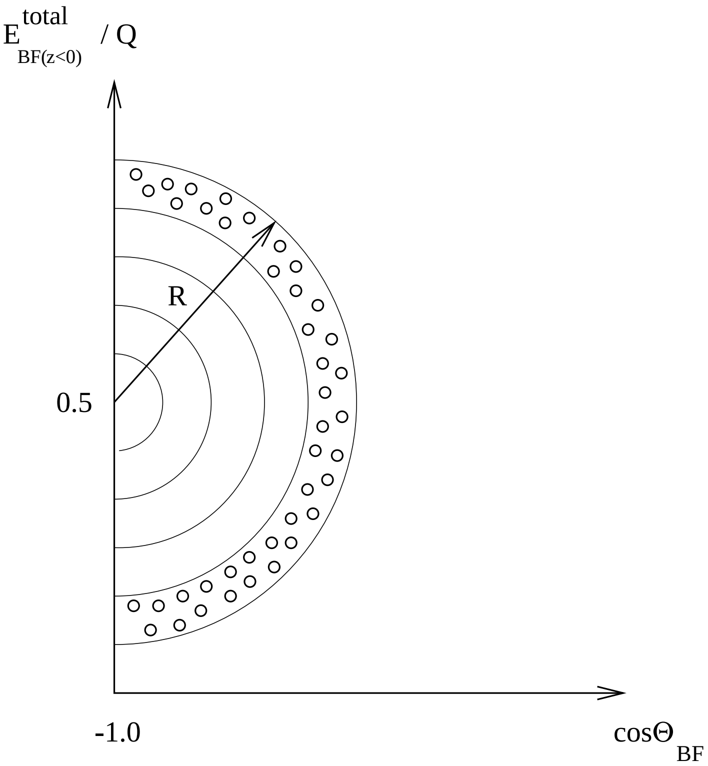

Figure 7.12: *Semi-circles centred at the point (0.5,-1.0) in the* $E^{total}_{BF(z<0)}/Q$ *(vs)* $\cos\Theta_{BF}$ *plane.*

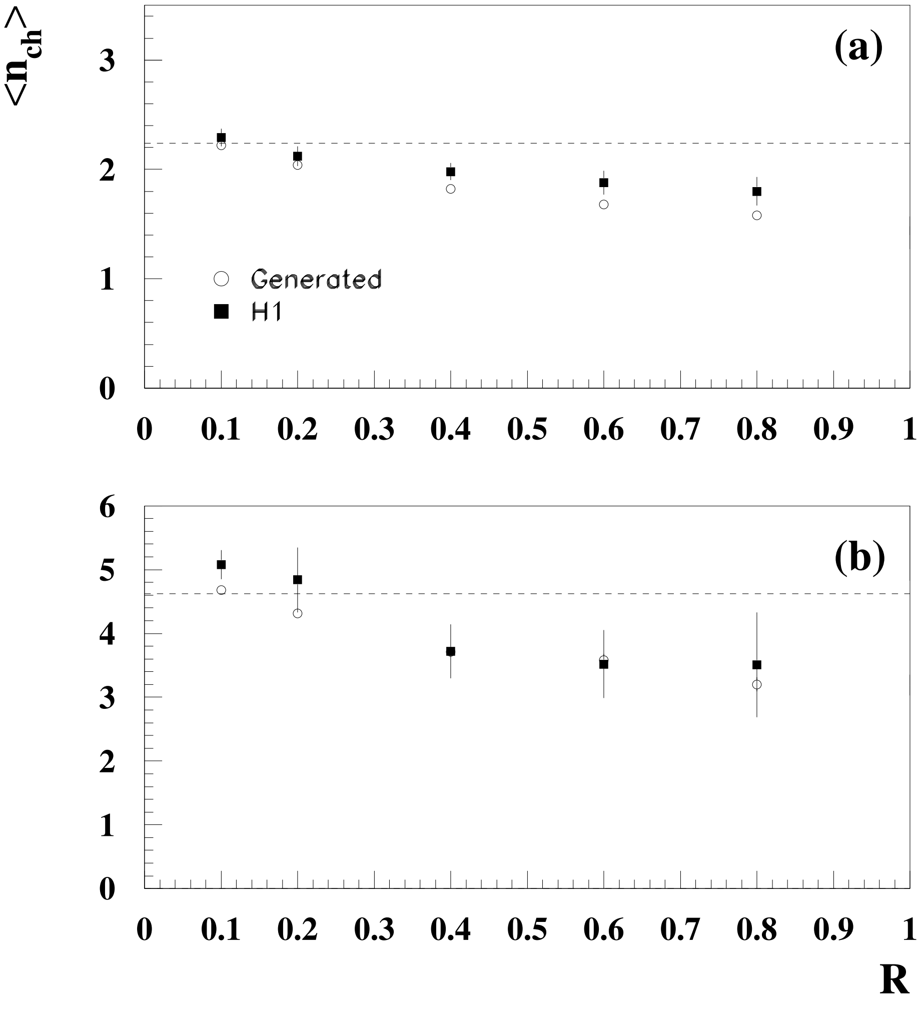

Figure 7.13: *The exclusive average charged multiplicity as a function of the ring radius, R, for the low Q^2 (a) and the high Q^2 (b) corrected data samples (closed squares). The generated multiplicity (open circles) is shown for comparison. The average charged multiplicity for one hemisphere of an e^+e^- event (dashed line) is shown also.*

7.5.4 Evolution of the Peak Position and Width of the Fragmentation Function

In order to measure the peak position and width of the ξ distributions, the OPAL collaboration fitted a distorted Gaussian distribution to OPAL [43] and TASSO [42] data over a limited interval around the peak. The form of the distorted Gaussian was suggested by Webber and Fong [82] and its five free parameters are calculated to next-to-leading order and hence by MLLA. It has also been reported by OPAL [43] that a fit using the MLLA formulae and its Gaussian approximation given in equation 3.13 provide a good description over the same region. However, while the MLLA fit provides a very good description from the lowest ξ values up to and slightly beyond the peak position, it nevertheless falls short of the data at large ξ. On the other hand, the distorted Gaussian is a better fit to the data at large values of ξ but is much poorer tending to overestimate the data at low values compared to the MLLA prediction. The Gaussian fit follows the MLLA prediction closely except in the regions well away from the peak position. At low values of ξ it tends to overestimate the data but only slightly compared to that of the distorted Gaussian and, at large values of ξ where there is only a slight overestimation of the data.

For consistency, it is desirable to perform an equivalent fit to the DIS data in order to compare to the published OPAL and TASSO results. In this thesis, all fits to the acceptance corrected scaled momentum distributions are performed with a Gaussian in a limited interval of ± 1 unit in ξ of the peak position as shown in figures 7.14 and 7.15 for each of the ten Q^2 intervals. The published e^+e^- results [42, 43] have been fitted using exactly the same procedure to remove any ambiguity to the fitting method and these results [83] are presented in table 7.3.

The results of these fits for both ξ_{peak} and ξ_{width} for each Q^2 interval are given in table 7.4 and presented in figure 7.16(a,b) as a function of the true (Monte Carlo corrected) average Q for events that satisfy the Breit frame energy flow selection. The statistical errors quoted are taken from the uncertainty due to fitting and the additional errors are all sources of systematic error discussed in section 7.8 added in quadrature. Again for comparison, the peak and width for distributions containing *all* events in the current hemisphere are presented in the last two columns with

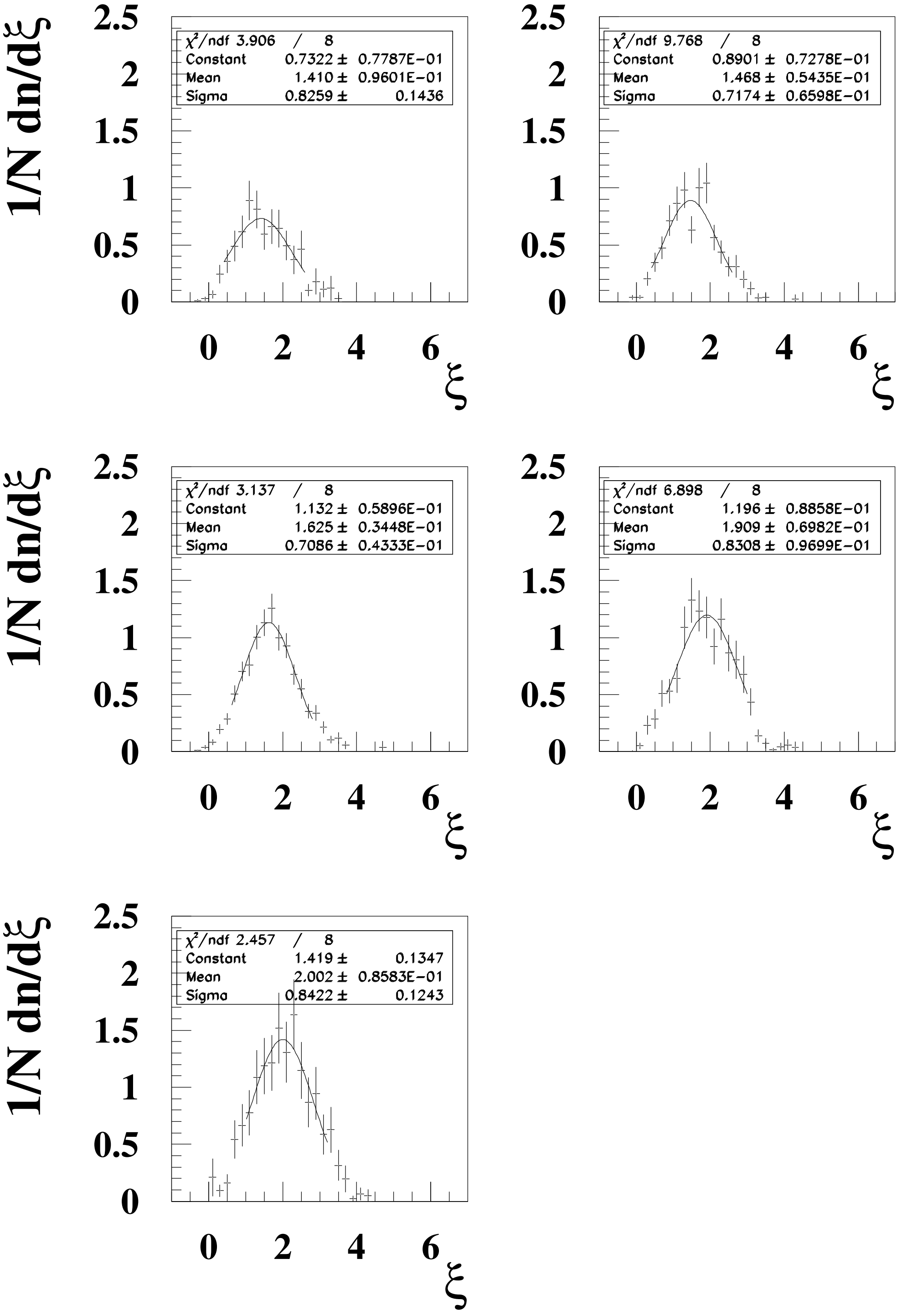

Figure 7.14: *Scaled momentum distributions for each Q^2 interval in the low Q^2 data sample. Each distribution has been acceptance corrected and a Gaussian fit performed over the limited interval of ± 1 unit in ξ of the statistical mean.*

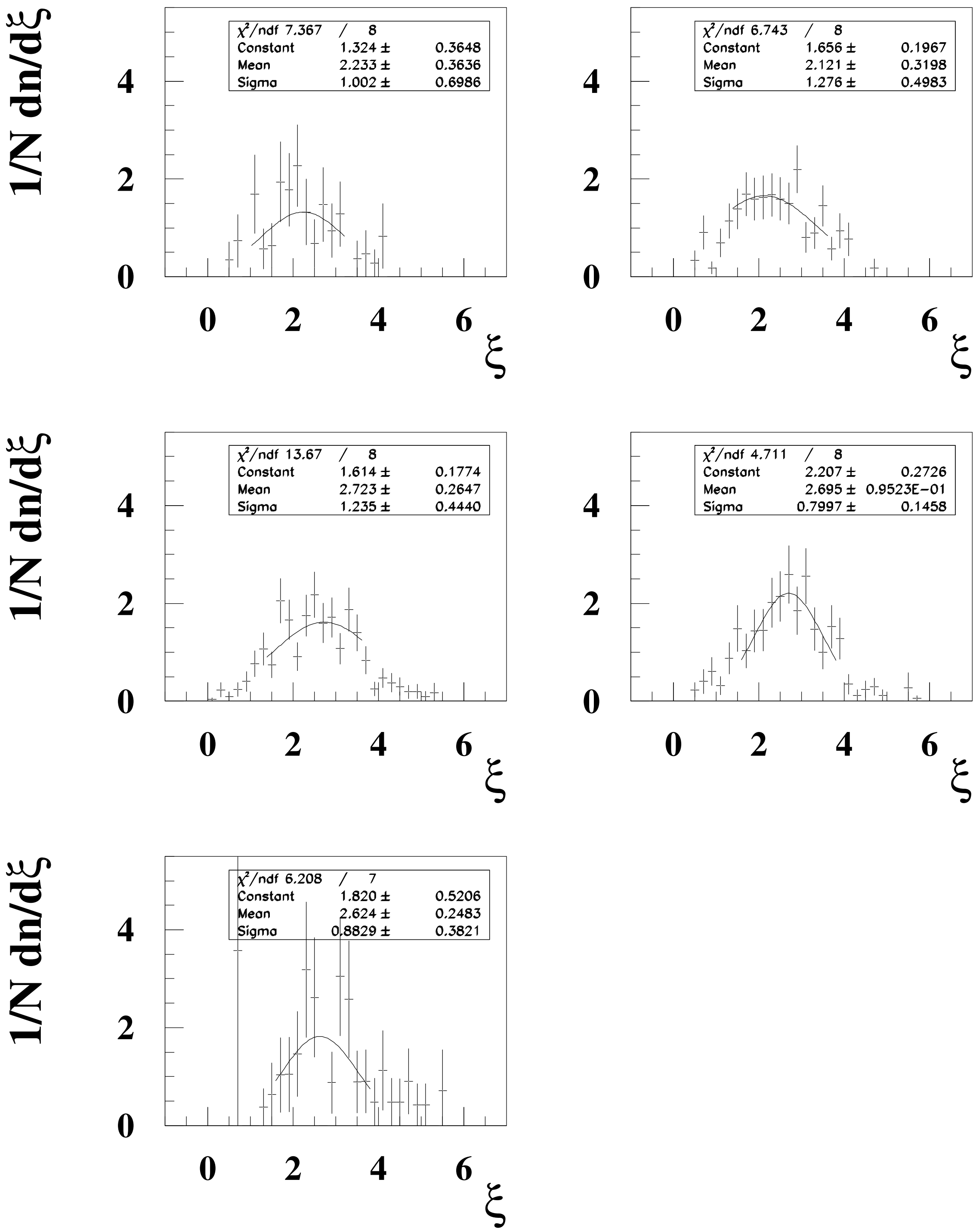

Figure 7.15: *Scaled momentum distributions for each Q^2 interval in the high Q^2 data sample. Each distribution has been acceptance corrected and a Gaussian fit performed over the limited interval of ± 1 unit in ξ of the statistical mean.*

Data Set	Mean	Width	χ^2/dof
TASSO 14 GeV	2.36 ± 0.02	0.90 ± 0.03	4.0/8
TASSO 22 GeV	2.66 ± 0.02	0.92 ± 0.03	5.6/8
TASSO 35 GeV	2.97 ± 0.01	1.04 ± 0.02	28.6/8
TASSO 44 GeV	3.08 ± 0.02	1.14 ± 0.03	12.6/8
OPAL 91 GeV	3.58 ± 0.01	1.35 ± 0.03	19.6/17

Table 7.3: *Results of fits done to the TASSO and OPAL data using a simple Gaussian.*

Q^2 Interval	**Energy flow selection**		**Total current hemisphere**	
(GeV^2)	Peak±stat±sys	Width±stat±sys	Peak±stat	Width±stat
12→15	1.41±0.10±0.05	0.83±0.14±0.03	1.45±0.08	0.72±0.08
15→20	1.47±0.06±0.05	0.72±0.07±0.02	1.49±0.08	0.82±0.09
20→40	1.63±0.04±0.06	0.71±0.05±0.02	1.66±0.06	0.74±0.04
40→60	1.91±0.07±0.07	0.83±0.10±0.03	1.94±0.09	0.91±0.11
60→80	2.00±0.09±0.07	0.84±0.12±0.03	2.01±0.10	0.87±0.13
100→175	2.23±0.36±0.08	1.00±0.70±0.02	2.27±0.17	0.75±0.27
175→250	2.12±0.32±0.08	1.28±0.50±0.03	2.18±0.30	1.26±0.48
250→450	2.72±0.26±0.10	1.24±0.44±0.03	2.68±0.23	1.09±0.32
450→1000	2.69±0.10±0.10	0.80±0.15±0.02	2.71±0.16	0.79±0.17
1000→8000	2.62±0.25±0.10	0.88±0.38±0.02	2.63±0.26	0.85±0.35

Table 7.4: *The peak and width of the fragmentation function for the Q^2 intervals given using the energy flow selection with peak fitting errors and all sources of systematic error added in quadrature. The peak and width for all events in the current hemisphere is shown for comparison with fitting errors only.*

fitting errors only.

7.5.5 Determination of Λ_{eff}

If Q is taken to be equivalent to $\sqrt{s_{ee}}$ and is normalised by an effective energy scale to give a dimensionless variable $Y = \ln(Q/2\Lambda_{eff})$ then, assuming gluon coherence, the predicted MLLA behaviour of the peak position and width as shown in chapter 3.5 is [38]

$$\xi_{peak} = 0.5Y + c_2\sqrt{Y} + \mathcal{O}(1) \tag{7.7}$$

$$\xi_{width} = \sqrt{Y^{3/2}/2c_1} \tag{7.8}$$

Result	**Number of flavours**		
	3	4	5
c_1	3.46	3.60	3.75
c_2	0.54	0.56	0.59
H1 fit			
Λ_{eff} (GeV)	0.24±0.03	0.22±0.03	0.21±0.03
$\mathcal{O}(1)$	-0.38±0.11	-0.47±0.09	-0.56±0.10
OPAL fit			
Λ_{eff} (GeV)	0.21±0.02		
$\mathcal{O}(1)$	-0.32±0.06		

Table 7.5: *The results of the MLLA fit to the data presented in the second and third columns of table 7.4 assuming three colours and three or more flavours.*

where c_1 and c_2 are constants dependent only on the number of colours and flavours in QCD, Λ_{eff} sets the scale of the mass of the final state fragmented hadrons, and $\mathcal{O}(1)$ contains higher order corrections. Following [43] in assuming three flavours, the value of these free parameters obtained from a simultaneous fit to the peak and width of the H1 data yields the result $\Lambda_{eff} = 0.24 \pm 0.04$ and $\mathcal{O}(1) = -0.38 \pm 0.11$. This fit is the solid line shown in figure 7.16 (a,b). For comparison, the results of this fit and of those obtained by assuming more than three flavours are presented in table 7.5. The results of these parameters are to be compared with the analysis [43] of e^+e^- ξ_{peak} evolution [42, 43, 44, 45] as a function of $Y = \ln(E^*/2\Lambda_eff)$ which gives $\Lambda_{eff} = 0.21 \pm 0.02$ GeV and $\mathcal{O}(1) = -0.32 \pm 0.06$. These results are also presented in table 7.5.

7.5.6 Comparison to Different Monte Carlo Models

The solid line fit to the data in figure 7.16 has a very small curvature and approximates strongly to a straight line. Thus the evolution of ξ_{peak} has been fitted to a straight line of the form:

$$\xi_{peak} = a\ln(Q) + b \tag{7.9}$$

A straight line fit to ξ_{peak} as a function of $\ln(Q)$ gives a gradient of 0.65 ± 0.07. The results of this fit are shown in the second and third column of table 7.6. The

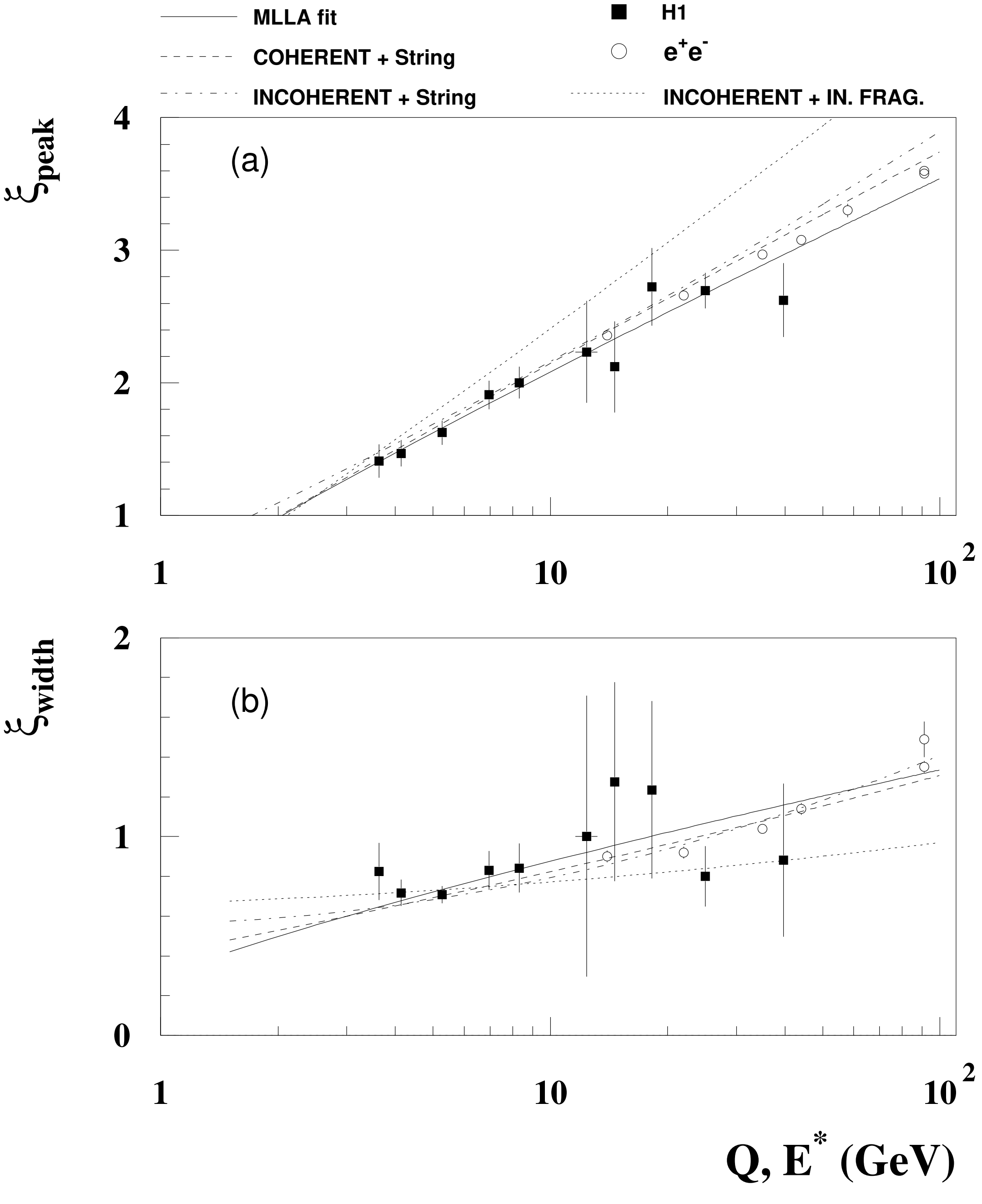

Figure 7.16: *Evolution of (a) the peak position and (b) the width (σ) of a fitted Gaussian fragmentation function compared with similar fits to e^+e^- data. The solid line is a two-parameter simultaneous MLLA-expectation fit to the H1 data. See text for a discussion of the various model predictions.*

low values of χ^2/dof confirm the viability of this approximation and are presented in the fourth column titled 'line fit' of table 7.6.

To attempt to determine which model of QCD implementation best describes the data and whether it is necessary to include gluon coherence, the results are compared to those at the generated hadron level produced from Monte Carlo programs in which the QCD cascade is modelled in different ways. Approximately 40K events of each of the following Monte Carlo samples were examined:

- LEPTO 6.1 (MEPS) with coherent parton showers and Lund string hadronisation,
- LEPTO 6.1 (MEPS) with incoherent parton showers and Lund string hadronisation,
- LEPTO 6.1 (MEPS) with incoherent parton showers and independent hadronisation,
- HERWIG which implements a cluster fragmentation scheme,
- ARIADNE + LEPTO 6.1 (MEAR) with a coherent parton shower ansatz and Lund string hadronisation,
- ARIADNE + LEPTO 6.1 (MEAR) with incoherent parton showers and independent hadronisation.

The results of the straight line fit for each of the models are also presented in table 7.6.

7.5.7 Evidence for Gluon Coherence

The dashed line of figure 7.16 shows the prediction at the generator level of the LEPTO 6.1 Monte Carlo with an assumption of gluon coherence in the parton showers modeled by implementing angular ordering and using a LUND string model [34] for final hadronisation. Reference [43] claims a significant need for gluon coherence, noting that a gradient of unity from a straight line fit would be the naïve expectation if the multiplicity in a parton shower increased solely due to constraints of longitudinal phase space. The results show that abandoning the angular-ordering

Monte Carlo	ξ_{peak}		**line fit**	**data fit**
Model	Gradient	Intercept	χ^2/dof	χ^2/dof
H1 data	0.65±0.07	0.57±0.14	0.50	
MEPS				
Coherent Cascade + String Frag.	0.70±0.01	0.52±0.02	1.51	1.10
Incoherent Cascade + String Frag.	0.71±0.01	0.54±0.02	0.78	1.43
Incoherent Cascade + Independent Frag.	0.94±0.01	0.26±0.02	0.52	6.44
HERWIG				
Cluster Frag.	0.73±0.03	0.33±0.05	1.78	1.75
MEAR				
String frag.	0.65±0.03	0.63±0.04	0.36	1.15
Independent. frag.	0.75±0.03	0.56±0.05	1.98	3.25

Table 7.6: *Parameters from a straight line fit to data and different Monte Carlo models*

model of gluon coherence in the parton shower, but maintaining string hadronisation (dashed-dotted line in figure 7.16) gives almost indistinguishable evolution predictions. The results from HERWIG [58] with cluster hadronisation (not shown) are similarly indistinguishable. A crude implementation [84] of an independent fragmentation model with or without (dotted line) gluon coherence gives effective gradients only slightly below unity.

A χ^2 test has been performed to determine the level of confidence [85] with which a given Monte Carlo model can be said to describe the data[2]. The χ^2/dof from this test is presented in the final column labelled 'data fit' of table 7.6. From these results it can be concluded that the data are in favour of those models that implement gluon coherence by explicitly modelling these effects in the parton shower. The data are also in support of those models that do not attempt to model coherence in the parton shower but implement the LUND hadronisation scheme. This strongly suggests that the LUND hadronisation scheme is more effective at reducing the gradient expected from the naïve interpretation rather than any effect caused by modelling gluon coherence in the parton shower and thus the need for an ansatz to describe coherence effects is not necessary.

7.6 Dependence on x

High Q^2 events are only accessible at high Bjorken x and this correlation is amplified by the W^2 and y cuts made in this analysis. Thus it is possible that the results presented so far are a reflected effect of a jet fragmentation evolution in terms of the parton momentum fraction x rather than Q^2. The expectations of MLLA are that, although distributions in the target region should show some x dependence [86], the peak of ξ in the current region should depend only on Q^2. The possibility of such x dependence has been investigated, suffering the consequent loss of statistics, by defining a number of rectangular (x, Q^2) cells well within acceptance limits and somewhat broader in Q^2 than previously used. The corrected values of ξ_{peak} are displayed in figure 7.17 as a function of x at constant Q^2, with statistical errors

---

[2] This test has been done to the peak positions only because of the large statistical errors associated with the width measurements.

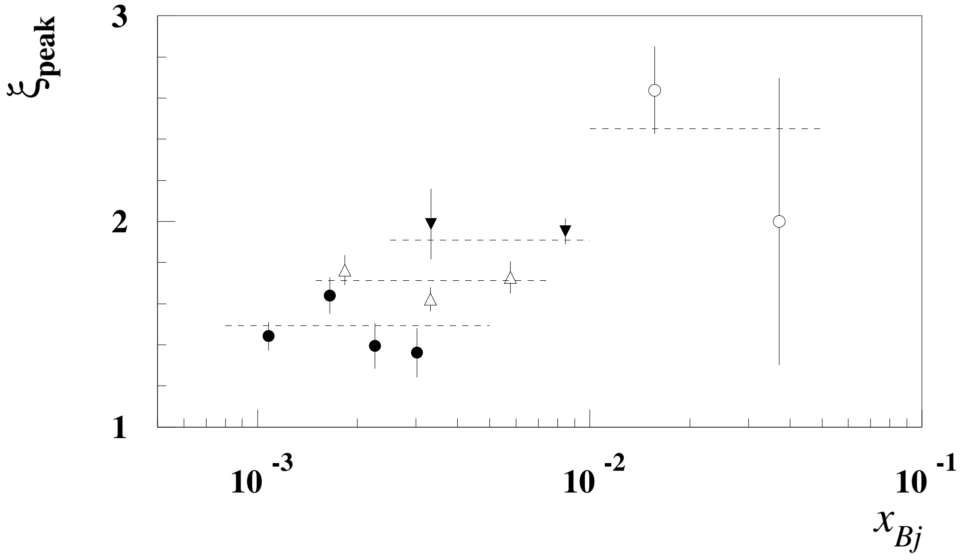

Figure 7.17: *Position of the fragmentation function peak as a function of Bjorken* x*, in the intervals (solid circles)* $12 < Q^2 < 25$ GeV^2*, (open triangles)* $25 < Q^2 < 45$ GeV^2*, (solid triangles)* $45 < Q^2 < 80$ GeV^2*, and (open circles)* $200 < Q^2 < 500$ GeV^2*. The dashed lines refer to the* ξ_{peak} *expected from the fit at the relevant mean* Q^2 *value.*

only. The dashed line refer to the expected values as interpolated from the fit to the function given in section 7.5.5. It is clear that these data indicate no observable x dependence.

7.7 Inclusion of Higher Order Processes

The analysis has been repeated with the inclusion of events which have zero energy in the current region of the Breit frame which were discussed in chapter 5.6. The peak positions of the fragmentation function are observed to move only slightly, but well within the fitting errors presented in the second column of table 7.4. The multiplicities[3] generally are lower especially at low Q^2. In the lowest Q^2 interval,

---

[3] A similar [87] analysis done by the ZEUS collaboration defined *their* total current hemisphere as that which also included higher order processes. As a result, a multiplicity comparison for the total current hemisphere between H1 and ZEUS is found to disagree at low Q^2. With the inclusion

they are 30% lower compared to those presented in the second column of table 7.2. As Q^2 increases this difference becomes much less significant.

7.8 Systematic Checks

A series of systematic checks were performed to investigate the sensitivity of the results to features of the central analysis. The sensitivity to these various systematic effects is discussed in the following subsections in terms of the peak, width and multiplicity of the fragmentation function.

- $\pm 1\sigma$ level of the resolution in $\cos\theta_B$ due to uncertainty in the selection of the Breit frame current hemisphere.
- The scattered electron energy was required to be greater than 20 GeV rather than 14 GeV.
- The cut on the square of the total hadronic energy flow through the detector was increased to 4400 GeV^2.
- The energy measurement for electrons was altered by varying the electromagnetic scale factors in the BEMC and LAr due to the uncertainty of calibration.
- Monte Carlo model used to make acceptance corrections for the data.
- Size of the Gaussian fitting interval about the mean of ξ.

7.8.1 Resolution in $\cos\theta_B$

The peak, width of the fragmentation function are affected through uncertainty in the selection of the Breit frame current hemisphere ($\cos\theta_B = 0$). As an estimator of the systematic error that might be introduced because of this selection, the analysis has been repeated using the selection at the $\pm 1\sigma$ level and extreme differences are taken to be an estimator of the systematic error. For both data sets, the change in the peak and width was small at 3% and 1% respectively.

---

of these events, both analyses are in agreement with one another.

7.8.2 Hadronic Energy Flow

For the events in this analysis, lines of constant W^2 in the (x, Q^2) plane are, to a good approximation, parallel to lines of constant y. In order to test the sensitivity of the results to QED radiative effects, a cut of $W^2 > 4400$ GeV^2 was demanded. This cut forces $y \geq 0.05$ and thus removes data which are more likely to suffer through QED radiation. This increase is expected to make only a small change because the event selection was designed to avoid large QED radiative effects by originally imposing the cut $W^2 > 3000$ GeV^2. The affect of imposing this cut was found to be negligible and is not included in the systematic error.

7.8.3 Photoproduction Background

Photoproduction events provide a large source of background to DIS events in which a high energy $\pi^0 \to \gamma\gamma$ fakes a scattered electron in the BEMC. In such cases, the true scattered electron is not detected in the calorimeter since the virtuality of the exchanged photon approaches zero. The kinematic variables and thus the boost to the Breit frame will be completely wrong. To ascertain the sensitivity to the possible residual photoproduction contamination in the data, the required scattered electron energy cluster in the BEMC was increased to 20 GeV. The affect of this cut was found to be negligible and is not included in the systematic error.

7.8.4 Electromagnetic Scale Factors

An additional source of systematic error is the measurement of the energy of the scattered electron in either the BEMC or the LAr. This directly affects the boost to the Breit frame since the kinematic variables are determined from the scattered electron energy. The electromagnetic energy scale for electrons is known to an accuracy of ±1.7% in the BEMC, and ±3% in the LAr calorimeter [2]. This change is implemented for the data only (i.e the scale factors in the Monte Carlo are not changed) in order to test the uncertainty in the energy measurement. For the low Q^2 sample, a 2% change to the energy scale causes a 1.2% change to the peak, a 2% change to the width and a 4.5% change to the multiplicity. For the high Q^2 data, a 3% change to the scale factor causes a 1% change to the peak, a 1% change to the width and 3% change to the multiplicity.

7.8.5 Correction to the Data

A different Monte Carlo model was used to determine the systematic uncertainty which arises due to unfolding the data using MEAR. The data were corrected with 100 K MEPS events. The MEPS Monte Carlo reproduces the characteristics of the hadronic final state reasonably well, but in the forward region of the detector it does not describe the data as well as MEAR. The percentage change to the peak, width and multiplicity was less than the 2% level and has also been included in the systematic error.

7.8.6 Transverse Momentum Cut

With the exception of the p_T cut, track cuts such as the number of hits, track length and so on are technical cuts that merely define what a good track is. These cuts are accounted for in the Monte Carlo simulation and are not expected to change the mean position of the fragmentation function. However, the systematic error associated to track simulation can be investigated by altering the p_T requirement. Figure 7.18 shows a scatter plot of p_T against ξ. It can be seen that there is a high degree of correlation between these variables and therefore one would expect that for a poor simulation of this correlation there would be a shift in ξ_{peak} as the p_T cut is varied.

The transverse momentum requirement for tracks in the central jet chamber was increased to 200 MeV. Since the majority of tracks are located in this region, no change was implemented for the forward or combined tracks which make use of a momentum cut. The percentage change to the peak and width as a result of increasing the transverse momentum cut was found to be $< 1\%$ and, although small, has been included in the systematic error.

7.8.7 Fitting Interval About the Mean of ξ

The Gaussian fits to the fragmentation function were repeated using two different intervals about the statistical mean of the ξ distribution. These intervals were chosen

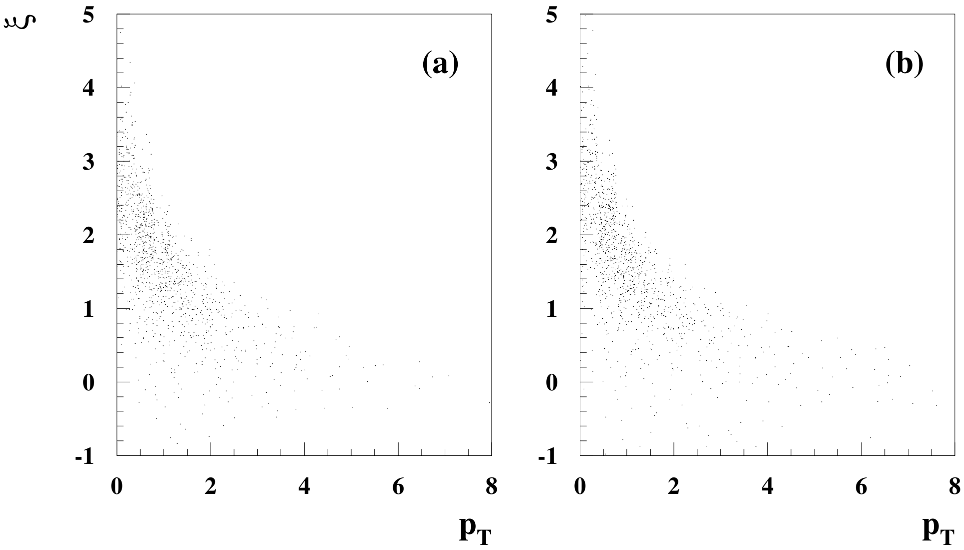

Figure 7.18: *Scatter plot showing the correlation between the fragmentation variable ξ and p_T of the track for (a) the low Q^2 data set and (b) low Q^2 reconstructed Monte Carlo.*

to be ± 1.2 and ± 1.4 units in ξ. The changes to the peak and width are well within 1σ of the fitting errors quoted and have not been included in the systematic error.

7.8.8 Sensitivity of ξ to (x, Q^2) Migrations

An investigation into the sensitivity of the peak position due to migrations in the (x, Q^2) bins has been performed. The peak position is found to be insensitive to Q^2 migrations on account of its excellent resolution ≤ 6 % over the (x, Q^2) plane.

7.9 Conclusions

A comparison of the multiplicities for events with and without the Breit frame energy flow selection as presented in table 7.2 show a difference. This difference is Q^2 dependent and becomes more significant at low Q^2 where higher order processes result in a loss of current related fragments to the target region.

The peak and widths (table 7.4) on the other hand are only slightly lower than those values obtained with the selection. These parameters are thus insensitive to the

$\mathbf{Q}^2$ Interval	$\Delta\xi_{peak}\%$			$\Delta\xi_{width}\%$			$\Delta < n_{ch} >\%$		
(GeV^2)	stat	sys	total	stat	sys	total	stat	sys	total
12→15	7.0	3.0	8.0	17.0	3.0	17.0	7.0	4.5	8.0
15→20	4.0	3.0	5.0	10.0	3.0	10.0	6.0	4.5	8.0
20→40	2.0	3.0	4.0	7.0	3.0	8.0	4.0	4.5	6.0
40→60	4.0	3.0	5.0	12.0	3.0	12.0	5.0	4.5	7.0
60→80	5.0	3.0	6.0	14.0	3.0	14.0	6.0	4.5	8.0
100→175	16.0	4.0	16.0	14.0	3.0	14.0	14.0	4.0	15.0
175→250	15.0	4.0	15.0	7.0	3.0	8.0	7.0	4.0	8.0
250→450	10.0	4.0	11.0	7.0	3.0	8.0	7.0	4.0	8.0
450→1000	4.0	4.0	6.0	7.0	3.0	8.0	7.0	4.0	8.0
1000→8000	10.0	4.0	11.0	19.0	3.0	19.0	19.0	4.0	19.0

Table 7.7: *The fitting error, systematic error and total error expressed as a fractional percentage (Δ) of the nominal peak, width and multiplicity of the fragmentation function for each of the Q^2 intervals. The fitting error and systematic errors are added in quadrature to obtain the total error.*

loss of hadronic fragments to the target region through QCD radiation. A study into the sensitivity of the peak, width and multiplicity of the fragmentation function due to systematic uncertainty has been investigated. It has been shown that in general, the size of the fitting error dominates over all other sources of systematic error. The average charged multiplicity is dominated by statistical errors particularly at high Q^2. A summary of the fitting results, systematic and total error expressed as a percentage (Δ) of the nominal values obtained for each of the Q^2 intervals is presented in table 7.7. The nominal values for the peak and width, and the multiplicity can be found in table 7.4 and 7.2 respectively for events which satisfy the Breit frame energy flow selection.

Chapter 8

Conclusions

This thesis has presented a measurement of the scaled momentum distributions of charged particles in the current region of the Breit frame at HERA and compared the results to those obtained in e^+e^- experiments. The basic features of the fragmentation function, when examined in this frame as a function of Q are close to those of quarks pair-created in e^+e^- interactions when examined in their CMS as a function of $\sqrt{s_{ee}}$.

The multiplicity evolution of the fragmentation function in the current region of the Breit frame has been compared with half the average charged multiplicity of an e^+e^- event. This has shown that Q in the Breit frame is a suitable scaling variable equivalent to $\sqrt{s_{ee}}$ in e^+e^- interactions. However, at low Q^2 values there is a disagreement between the multiplicities. It has been shown that this is due to the onset of higher order QCD effects which give rise to events (BGF and initial state QCDC) that have a significant loss of current related fragments to the target hemisphere. Events of this type are not mirrored in the e^+e^- system and a multiplicity analysis performed after removing such events from the sample is shown to agree with e^+e^-.

The predicted MLLA behaviour for the peak and width of the evolving fragmentation functions were used to fit to the data. The two free parameters from the theory, Λ_{eff} and $\mathcal{O}(1)$ are found to be 0.24 ± 0.04 GeV and -0.38 ± 0.11 respectively. The data presented in this thesis are consistent with the predictions of the MLLA and the assumptions of LPHD.

The evolution of the peak position with Q has been compared to a number of Monte Carlo models to examine the evidence, if any, for gluon coherence. According to theoretical expectation, gluon coherence manifests itself by reducing the slope of this evolution compared to that which would be obtained if the gluon emissions were not restricted by angular ordering. The data were found to favour those models that included the Lund string hadronisation scheme irrespective of whether those models explicitly included/excluded gluon coherence. Although the H1 data are in agreement with all other data that claim gluon coherence, the necessity for coherence, other than that already parameterised by the Lund string model, has not been demonstrated.

This analysis has presented clear evidence that the fragmentation properties of the struck quark from the proton in deep inelastic scattering are very similar to those that are pair created in e^+e^- interactions. The results therefore provide evidence for the universality of quark fragmentation.

Appendix A

Tables of Data

$1/N dn_{ch}/d(\cos\theta_B)$				
$\cos\theta_B$	**Low Q^2 sample**		**High Q^2 sample**	
bin interval	Flow sel.	Total cur.	Flow sel.	Total Cur.
-1.0 → -0.9	2.85 ± 0.17	2.27 ± 0.13	14.70 ± 1.10	12.13 ± 0.88
-0.9 → -0.8	2.44 ± 0.15	1.90 ± 0.11	6.40 ± 0.63	5.28 ± 0.52
-0.8 → -0.7	2.25 ± 0.15	1.90 ± 0.11	5.10 ± 0.56	4.29 ± 0.46
-0.7 → -0.6	2.05 ± 0.14	1.81 ± 0.11	3.16 ± 0.42	2.89 ± 0.36
-0.6 → -0.5	2.00 ± 0.14	1.75 ± 0.10	4.04 ± 0.49	3.43 ± 0.41
-0.5 → -0.4	2.05 ± 0.14	1.84 ± 0.11	2.98 ± 0.41	2.69 ± 0.35
-0.4 → -0.3	1.89 ± 0.14	1.73 ± 0.11	2.32 ± 0.37	2.16 ± 0.32
-0.3 → -0.2	1.81 ± 0.14	1.74 ± 0.11	1.98 ± 0.34	1.97 ± 0.30
-0.2 → -0.1	1.73 ± 0.14	1.65 ± 0.11	2.48 ± 0.39	2.27 ± 0.33
-0.1 → 0.0	1.47 ± 0.12	1.57 ± 0.11	2.53 ± 0.39	2.46 ± 0.34
0.0 → 0.1	1.58 ± 0.13	1.65 ± 0.11	1.66 ± 0.31	1.99 ± 0.30
0.1 → 0.2	1.77 ± 0.14	1.87 ± 0.11	1.43 ± 0.29	1.46 ± 0.26
0.2 → 0.3	1.91 ± 0.15	1.93 ± 0.12	1.89 ± 0.35	2.20 ± 0.32
0.3 → 0.4	1.78 ± 0.14	2.10 ± 0.12	1.60 ± 0.32	1.96 ± 0.30
0.4 → 0.5	1.86 ± 0.14	2.36 ± 0.13	2.60 ± 0.41	2.97 ± 0.38
0.5 → 0.6	2.11 ± 0.15	2.43 ± 0.13	2.50 ± 0.40	3.15 ± 0.39
0.6 → 0.7	2.57 ± 0.16	3.09 ± 0.14	3.11 ± 0.43	2.99 ± 0.37
0.7 → 0.8	3.27 ± 0.19	3.91 ± 0.16	3.90 ± 0.50	4.24 ± 0.46
0.8 → 0.9	4.65 ± 0.22	5.63 ± 0.20	5.93 ± 0.63	6.25 ± 0.57
0.9 → 1.0	10.32 ± 0.33	11.63 ± 0.28	11.20 ± 0.94	12.05 ± 0.86

Table A.1: Event normalised distribution of the cosine of the Breit frame polar angle for the low and high Q^2 samples, with statistical errors only.

$1/N dn^{\pm}/dx_p$				
x_p	**Low Q^2 sample**		**High Q^2 sample**	
bin interval	+ ve ± stat	− ve ± stat	+ ve ± stat	− ve ± stat
0.0 → 0.1	2.49 ± 0.17	2.44 ± 0.16	13.27 ± 0.93	13.68 ± 0.93
0.1 → 0.2	3.29 ± 0.19	3.27 ± 0.18	5.27 ± 0.58	5.62 ± 0.60
0.2 → 0.3	2.00 ± 0.14	2.05 ± 0.14	2.35 ± 0.39	1.91 ± 0.35
0.3 → 0.4	1.16 ± 0.11	1.10 ± 0.10	0.65 ± 0.20	0.86 ± 0.23
0.4 → 0.5	0.73 ± 0.08	0.56 ± 0.07	0.74 ± 0.23	0.61 ± 0.20
0.5 → 0.6	0.29 ± 0.05	0.42 ± 0.06	0.25 ± 0.13	0.17 ± 0.10
0.6 → 0.7	0.21 ± 0.04	0.19 ± 0.04	0.10 ± 0.07	0.17 ± 0.10
0.7 → 0.8	0.15 ± 0.03	0.11 ± 0.03	0.17 ± 0.11	0.00 ± 0.00
0.8 → 0.9	0.05 ± 0.02	0.07 ± 0.02	0.00 ± 0.00	0.12 ± 0.14
0.9 → 1.0	0.05 ± 0.02	0.008 ± 0.005	0.00 ± 0.00	0.00 ± 0.00

Table A.2: Event normalised x_p distribution for positive and negative tracks, for the low and high Q^2 data samples with statistical errors only.

$1/N dn/d\xi$		
ξ interval	**Low Q^2 sample**	**High Q^2 sample**
0.0 → 0.2	0.066 ± 0.013	0.015 ± 0.016
0.2 → 0.4	0.210 ± 0.028	0.078 ± 0.047
0.4 → 0.6	0.298 ± 0.034	0.227 ± 0.084
0.6 → 0.8	0.504 ± 0.048	0.557 ± 0.014
0.8 → 1.0	0.661 ± 0.054	0.318 ± 0.098
1.0 → 1.2	0.789 ± 0.061	0.669 ± 0.144
1.2 → 1.4	1.000 ± 0.070	0.946 ± 0.171
1.4 → 1.6	1.000 ± 0.069	1.060 ± 0.188
1.6 → 1.8	1.116 ± 0.075	1.625 ± 0.230
1.8 → 2.0	1.042 ± 0.074	1.555 ± 0.223
2.0 → 2.2	0.836 ± 0.064	1.402 ± 0.210
2.2 → 2.4	0.761 ± 0.062	1.844 ± 0.246
2.4 → 2.6	0.595 ± 0.056	1.915 ± 0.250
2.6 → 2.8	0.434 ± 0.047	1.718 ± 0.241
2.8 → 3.0	0.402 ± 0.049	1.758 ± 0.233
3.0 → 3.2	0.254 ± 0.037	1.529 ± 0.219
3.2 → 3.4	0.142 ± 0.026	1.391 ± 0.216
3.4 → 3.6	0.105 ± 0.025	1.177 ± 0.193
3.6 → 3.8	0.040 ± 0.015	0.906 ± 0.168
3.8 → 4.0	0.012 ± 0.007	0.675 ± 0.150
4.0 → 4.2	0.017 ± 0.009	0.562 ± 0.133
4.2 → 4.4	0.019 ± 0.013	0.180 ± 0.075
4.4 → 4.6	0.000 ± 0.000	0.185 ± 0.078
4.6 → 4.8	0.018 ± 0.023	0.241 ± 0.090
4.8 → 5.0	0.000 ± 0.000	0.125 ± 0.066

Table A.3: Event normalised $D(\xi)$ distribution for the low and high Q^2 data samples satisfying the energy flow selection with statistical errors only.

Bibliography

[1] HERA, A Proposal for a Large Electron-Proton Colliding Beam Facility at DESY, DESY HERA 81-10(1981).

[2] H1 Collaboration, Technical Proposal for the H1 Detector (1986); H1 Collaboration, The H1 Detector at HERA, DESY 93-103 (1993).

[3] ZEUS Collaboration, The ZEUS Detector, Technical Proposal (1986); ZEUS Collaboration, The ZEUS Detector, Status Report (1989).

[4] HERMES Collaboration, A proposal to measure the spin-dependent structure functions of the neutron and the proton at HERA (1990).

[5] Proceedings of the Workshop "Physics at HERA", edited W.Buchmuller and G. Ingleman, Hamburg, Germany, Vol. 1 (1991).

[6] *Physical Review* **D1251** (1994).

[7] T. Ahmed et al., H1 Collaboration, *Phys. Lett.* **B299** (1993) 385.

[8] M. Goldberg, *Energy Calibration and Reconstruction in BEMC*, H1 note H1-05/93-292 (1993).

[9] H. Bethe, and W. Heitler, *Proc. Roy. Soc.* **A146** (1934) 83.

[10] J. Heatherington, ToF - The Time of Flight Device for H1, Thesis submitted to the University of London.

[11] G. Bernardi et al., Guide to the Simulation Program H1SIM, H1 document.

[12] H. Albrecht et al., H1PHAN - H1 physics analysis programm, H1 document (1991).

[13] S. Egli et at., Guide to the Simulation Program H1SIM, H1 document (1991).

[14] R. Brum et al., GEANT long writeup, CERN Program Library, W5103 (1989).

[15] I. Abt et al., H1 Collaboration, *Phys. Lett.* **B328** (1994) 176.

[16] T. Ahmed et al., H1 Collaboration, *Nucl. Phys.* **B445** (1995) 195.

[17] L. W. Whitlow et al., *Phys. Lett.* **B250** (1990) 193.

[18] A. C. Benevenuti et al., BCDMS Collaboration, *Phys. Lett.* **B223** (1989) 485.

[19] For a review see, e.g., S. R. Mishra and F. Sciulli, *Ana. Rev. Nucl. Part. Sci.* **39** (1989) 259.

[20] Yu. L. Dokshitzer, *JETP* **46** (1977) 641;
V. N. Gribov and L. N. Lipatov, *Sov. J. Nucl. Phys.* **15** (1972) 438 and 675.

[21] G. Altarelli, G. Parisi, *Nucl. Phys.* 126 (1977) 297.

[22] E. A. Kuraev, L. N. Lipatov and V. S. Fadin, *Sov. Phys.* **JETP 44** (1972) 199;
Y. Y. Balitsky and L. N. Lipatov, *Sov. J. Nucl. Phys.* 28 (1978) 282.

[23] T. Ahmed et al., H1 Collaboration, Nucl. Phys **B439** (1995) 471;
I. Abt et al., H1 Collaboration, Nucl. Phys **B407** (1993) 515;
M. Derrick et al., ZEUS Collaboration, Z. Phys. **C65** (1995) 379;
M. Derrick et al., ZEUS Collaboration, Phys. Lett. **B316** (1993) 412.

[24] A. D. Martin, Proc. of the Workshop on HERA, *J. Phys.* **G19** (1993) 1603.

[25] I. Abt et al., H1 Collaboration, *Z. Phys* **C63** (1994) 377-389.

[26] A. H. Mueller, Columbia preprint CU-TP-658 (1994).

[27] J. Kwiencinski, A. D. Martin, P. J. Sutton and K. Golec-Biernat, *Phys. Rev.* **D50** (1994) 217.

[28] K. Golec-Biernat, J. Kwiencinski, A. D. Martin, and P. J. Sutton , Phys. Lett. **B335** (1994) 220.

[29] L. Lönnblad, Comput. Phys. Comm. 71 (1992) 15.

[30] L. Lönnblad, *Z. Phys.* **C65** (1995) 285;
L. Lönnblad, CERN-TH/95-95;
A. H. Mueller, *Nucl. Phys.* **B415** (1994) 373.

[31] T. Ahmed et at., H1 Collaboration, *Nucl. Phys.* **B429** (1994) 477.

[32] M. Derrick et at., ZEUS Collaboration, *Phys. Lett.* **B315** (1993) 481.

[33] G. Ingelman, *LEPTO version 6.1 - The Lund Monte Carlo for Deep Inelastic Lepton-Nucleon Scattering* Proceedings of the Workshop "Physics at HERA", edited W.Buchmuller and G. Ingleman, Hamburg, Germany, Vol. 3 (1991) 1366.

[34] B. Andersson, G. Gustafson, G. Ingelman and T. Sjöstrand, *Phys. Rep.* 97 (1983) 31;
T. Sjöstrand, *Nucl. Phys.* **B248** (1984) 469;
T. Sjöstrand, Computer Phys. Comm. 39 (1986) 347;
T. Sjöstrand and M. Bengtsson, Computer Phys. Comm. 43 (1987) 367.

[35] T. Sjöstrand, JETSET 7.3, CERN -TH -6488 -92 (1992).

[36] D. H. Perkins, Introduction to High Energy Physics, Addison-Wesley publishing Co. (1987).

[37] D. Graudenz, *Phys. Lett.* **B256** (1991) 518;
T. Brodkorb, J. G. Körner, *Z. Phys.* **C54** (1992) 519;
T. Brodkorb, J. G. Körner, E. Mirkes and G. A. Schuler, *Z. Phys* **C44** (1989) 415;
F. A. Berends, W. T. Giele and H. Kuijf, *Nucl. Phys* **B321** (1989) 39;
K. Hagiwara and D. Zeppenfeld, *Nucl. Phys.* **B313** (1989) 560.

[38] Yu. L. Dokshitzer, V. A. Khoze, A. H. Mueller and S. I. Troyan, *Basics of Perturbative QCD*, editions Frontieres, (1991).

[39] A. Chudakov, *Izv. Akad. Nauk SSSR*, Ser. Fiz., 19 (1955) 650.

[40] Yu. L. Dokshitzer, V. S. Fadin and V. A. Khoze, *Phys. Lett.* **B115** (1982) 242;
Zeit. Phys. **C15** (1982) 325;
A. H. Mueller, *Nucl. Phys.* **B213** (1983) 85;
Nucl. Phys. **B241** (1984) 141.

[41] Ya. I. Azimov, Yu. L. Dokshitzer, V. A. Khoze, and S. I. Troyan, *Zeit. Phys.* **C31** (1986) 213;
Zeit. Phys. **C27** (1985) 65;
L. V. Gribov, Yu. L. Dokshitzer, V. A. Khoze, and S. I. Troyan, *Phys. Lett.* **B202** (1988) 276.

[42] TASSO Collaboration, W. Braunschweig et al., *Zeit. Phys.* **C47** (1990) 187.

[43] OPAL Collaboration, M. Z. Akrawy et al., *Phys. Lett.* **B247** (1990) 617.

[44] L3 Collaboration, B. Adeva et al., *Phys. Lett.* **B259** (1991) 199.

[45] TOPAZ Collaboration, R. Itoh et al., *Phys. Lett* **B345** (1995) 335.

[46] E. R. Boudinov, P. V. Chliapnikov and V. A. Uvarov, *Phys. Lett* **B309** (1993) 210.

[47] G. Thompson et. al., *Jet Finding in the Breit Frame*, *J. Phys.* **G19** (1993) 1575.

[48] G. Gustafson and U. Petterson, *Nucl. Phys.* **B306** (1988) 746;
G. Gustafson, *Phys. Lett.* **B175** (1986) 453.

[49] Ya. I. Azimov, Yu. L. Dokshitzer, V. A. Khoze and S. I. Troyan, *Phys. Lett.* **B165** (1985) 147.

[50] CERN 89-08, Vol. 3 (1989) 159.

[51] B. Andersson, G. Gustafson, L. Lönnblad and U. Pettersson, *Z. Phys.* **C43** (1989) 625;
B. Andersson and L. Lönnblad, *Phys. Lett.* **B277** (1992) 359.

[52] Yu. L. Dokshitzer et al., *Z. Phys.* **C55** (1992) 107.

[53] G. Alexander et al., OPAL Collaboration, *Phys. Lett.* **264B** (1991) 467.

[54] R. P. Feynman and R. D Field, *Nucl. Phys.* **B136** (1978) 1.

[55] T. Meyer, *Zeit. Phys.* **C12** (1982) 77.

[56] P. Hoyer, P. Osland, H. G. Sander, T. F. Walsh, P. M. Zerwas, *Nucl. Phys.* **B161** (1979) 349.

[57] P. Biddulph and G. Thompson, Comput. Phys. Commun. 67 (1989) 13.

[58] G. Marchesini et al., Comput. Phys. Commun. 67 (1992) 465.

[59] B. R. Webber, *Nucl. Phys.* **B238** (1984) 492.

[60] H. Hufnagel, H1REC - L5 Event Classification, H1 Document (1992 onwards).

[61] T. Ahmed, *First Measurements of the Neutral Current Deep Inelastic Cross-Sections and the Proton Structure Function $F_2(x, Q^2)$ at HERA*, Ph. D thesis, University of Birmingham (1994).

[62] T. Ahmed et al., H1 Collaboration, *Nucl. Phys.* **B429** (1994) 477.

[63] S. Burke, private communication.

[64] H1 Collaboration, HEP Conference, Brussels, 1995, paper EPS-0473.

[65] U. Bassler et al., *Progress on Kinematical Variable Reconstruction*, H1 note H1-03/93-274 (1993).

[66] K. C. Hoeger, *Measurement of x, y, Q^2 in Neutral Current Events* Proceedings of the Workshop "Physics at HERA", edited W.Buchmuller and G. Ingleman, Hamburg, Germany, (1991) Vol. 1 43.

[67] U. Bassler and G. Bernardi, *On the Kinematic Reconstruction of Deep Inelastic Scattering at HERA: the Σ Method* DESY pre-print 94-231 (1994).

[68] Proceedings of the Workshop "Physics at HERA", edited W.Buchmuller and G. Ingleman, Hamburg, Germany, (1987) Vol. 1 p33.

[69] Proceedings of the Workshop "Physics at HERA", edited W.Buchmuller and G. Ingleman, Hamburg, Germany, (1991) Vol. 1 p71.

[70] G. Ingelman, *Deep Inelastic Physics at HERA*, DESY 87-144 (1987).

[71] J. Blümlein, M .Klein, Proceedings of the Snowmass Workshop 'The Physics of the Next Decade', ed. R .Craven, (1990) 549.

[72] W. Von. Schlippe, private communication.

[73] Page 1292 of: Particle Data Group, K Gieselmann et al., *Phys. Rev.* **D50** (1994) 1175.

[74] S. Aid et. al., *Nucl. Phys.* **B445** (1995) 3.

[75] H1 Collaboration, EPS Conference, Brussels, EP-0483 (1995).

[76] G. Thompson and D. Kant, H1 internal note, H1-08/95-452.

[77] M. Z. Akrawy et. al., OPAL Collaboration, *Z. Phys.* **C47** (1990) 505.

[78] N. Sakai, *Phys. Lett.* **B45** (1979) 67;
J. Sheiman, *Nucl. Phys.* **B171** (1980) 445;
P. Allen et al., Nucl. Phys **B176** (1980) 333.

[79] Proceedings of the Workshop "Physics at HERA", edited W.Buchmuller and G. Ingleman, Hamburg, Germany, (1991) Vol. 3 p 1419; A. Kwiatkowski, H. Spiesberger and H. J. Möhring, Computer Phys. Comm. 69 (1992) 155.

[80] OPAL Collaboration, P. D. Acton et. al., *Z. Phys.* **C53** (1992) 539.

[81] P. Abreu et al., DELPHI Collaboration, *Phys. Lett.* **B347** (1995) 447.

[82] C. P. Fong and B. R. Webber, *Phys. Lett.* **B229** (1989) 289.

[83] J. V. Morris, Private communication.

[84] T. J. Sjöstrand, CERN preprint CERN-TH.7112/93 and Comput. Phys. Commun. 43 (1987) 367.

[85] R. J. Barlow, 'Statistics - A Guide to the Use of Statistical Methods in the Physical Sciences', ISBN 0471 92295 1.

[86] G. Ingelman and J. Rathsman, *J. Phys.* **G19** (1993) 1594.

[87] M. Derrick et al., ZEUS Collaboration, *Z. Phys.* **C67** (1995) 93.